Synthesis, Coordination and Photophysical Properties of Polynuclear Lanthanide(III) Self-assemblies Based on β-Diketonates Ligands

Dissertation

Tan Yan Bing

2020

Photonic Molecular Science Laboratory

Graduate School of Materials Science

Nara Institute of Science and Technology

TABLE OF CONTENTS

ABBREVIATIONS

CD	circular dichroism
CPL	circularly polarized luminescence
H_2(BTP)	1,3-bis(4,4,4-trifluoro-1,3-dioxobutyl)phenyl
H_2(BPP)	1,3-bis(3-pentafluoroethyl-3-oxopropanoyl)benzene
H_2(BHP)	1,3-bis(3-heptafluoropropyl-3-oxopropanoyl)benzene
H_2(BPB)	3,3-bis(3-pentafluoroethyl-3-oxopropanoyl)biphenyl
H_3(TTP)	1,3,5-tris(3-trifluoromethyl-3-oxopropanoyl)benzene
H_3(THP)	1,3,5-tris(3-heptafluoropropyl-3-3-oxopropanoyl)benzene
bipy	2,2'-bipyridine
Ph-Pybox	chiral 2,6-bis(4-phenyl-2-oxazolinyl)pyridine
(*R*)-Ph-Pybox	2,6-bis[(4R)-4-phenyl-2-oxazolinyl]pyridine
(*S*)-Ph-Pybox	2,6-bis[(4S)-4-phenyl-2-oxazolinyl]pyridine
(*R*)-^{i}Ph-Pybox	2,6-Bis[(4*R*)-(+)-isopropyl-2-oxazolinyl-2-yl]pyridine
(*S*)-^{i}Ph-Pybox	2,6-Bis[(4*S*)-(-)-isopropyl-2-oxazolinyl-2-yl]pyridine

1.0 INTRODUCTION

1.1 Symmetry and Chirality

1.1.1 Symmetry

The objects surrounding us have its own geometry. If the object is being made up of parts that are exactly match in shape, it is regarded as symmetric entity. In general, the term "symmetry" means the quality of being similar or equal and originates from the Greek word '*συμμετρία*' which refers to the agreement in dimensions, due proportion and arrangement[1]. In contrast, the objects that are lack of symmetry are asymmetric.

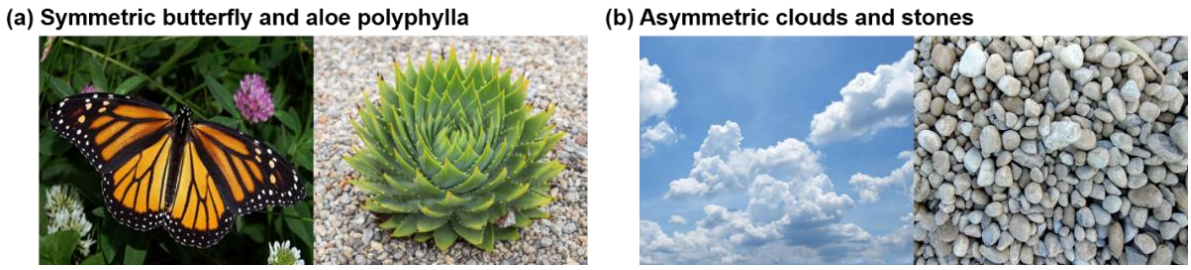

Figure 1.1. (a) Symmetric and (b) asymmetric objects[2].

The quality of similarity in the nature can be described scientifically under different mathematical operation or transformation. For example, the butterfly wings are invariant to the reflection on the imaginary line of symmetry which lies on the main body part. Besides, the leaves of aloe polyphylla exhibit spiral symmetry, where the leaves are growing and dilating in Fibonacci sequence from main rotational axis (on the centre of the aloe).

Under microscopic level, the symmetry concept can be applied to molecules, specially categorized as molecular symmetry in the field of chemistry. Based on the group theory, the symmetry present in molecules can be described by five types of symmetry element: identity (E), proper rotation (C_n), reflection (σ), improper rotation (S_n), and inversion centre (i)[3]. To be

a symmetric molecule, the molecule should be identical with its original configuration after performing symmetry operations. All the molecules have the *E* symmetry since all molecules are unchanged under identity operation. The molecules could possess n-fold axes of symmetry (C_n) if there are proper rotations by 360°/n, with the highest order of n be the principle axis. The mirror plane could be aligned parallelly (σ_v) or perpendicularly (σ_h) to the principal axis, reflecting the molecules into an indistinguishable configuration. If a σ_v plane bisects the angle between two C_2 axes, it is defined as dihedral plane (σ_d). An improper rotation (S_n) is a proper rotation followed by a horizontal mirror plane reflection (σ_h). A molecule has an inversion centre if there is reflection of all parts through the centre of molecule that results in a non-distinguishable configuration.

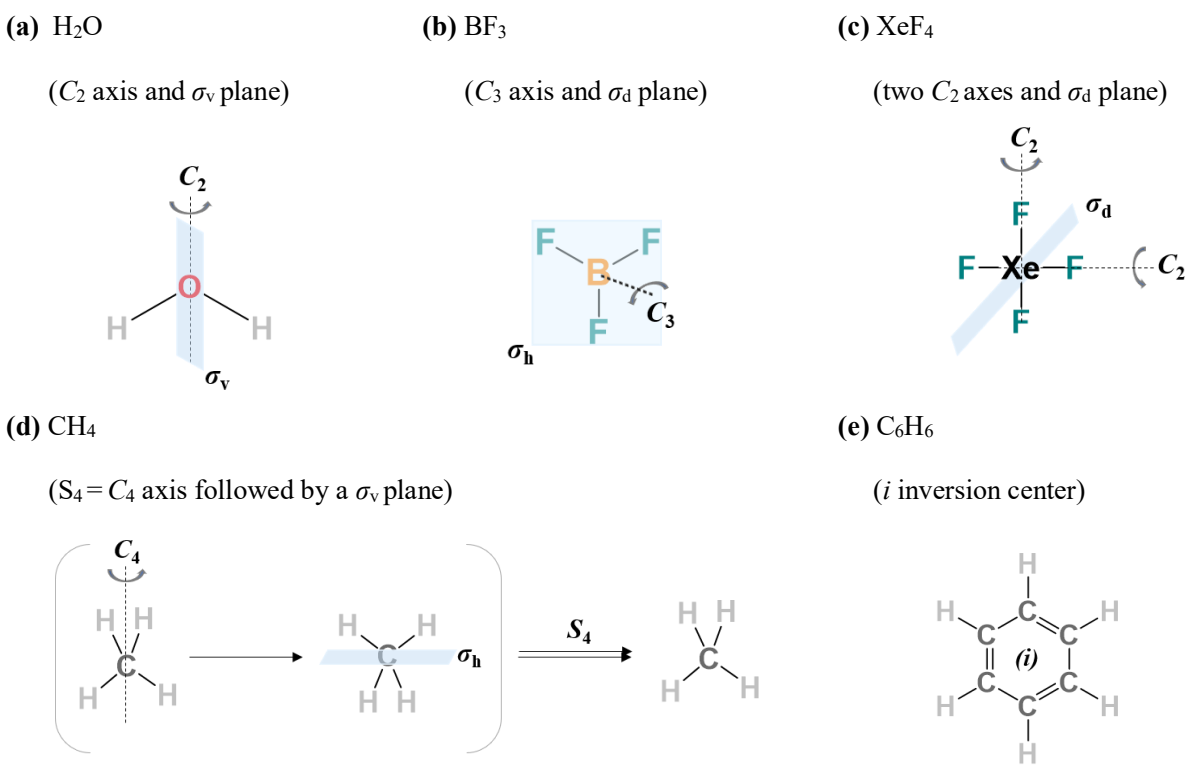

Figure 1.2. Symmetry elements on (a) water, (b) boron trifluoride, (c) xenon tetrafluoride, (d) methane and (e) benzene molecules.

1.1.2 Chirality

Chiral is a property of a rigid object of being non-superimposable to its mirror image[4]. It is closely related with symmetry since it makes use of the reflection through mirror as symmetry element to determine chirality in objects. An example that exhibits chiral property is hand, the right hand and left hand are non-distinguishable from each other (Figure 1.3b). In fact, the term of 'chirality' is originated from the Ancient Greek word χειρ (*kheir*), which means "hand"[5].

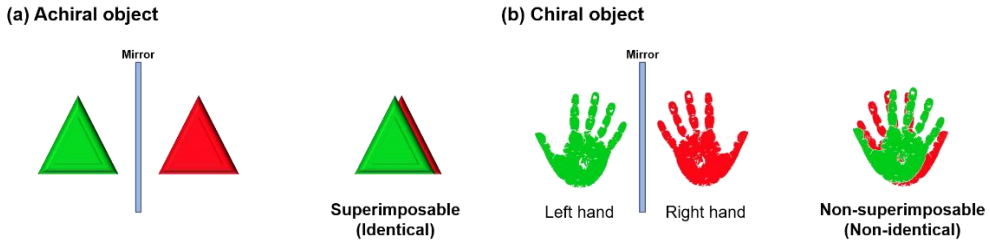

Figure 1.3. Achiral and chiral objects

In chemistry, chiral molecules[6] are stereoisomers. Different spatial arrangements of atoms in stereoisomers usually give rise to the chirality. For two stereoisomers are related by reflection, they are known as a pair of *R*/*S* enantiomers which consist of stereocenter/s indicating the point/s that result in opposite configuration (for instance, two steregenenic centers in 2,6-Bis[(4*R*/4*S*)-4-phenyl-2-oxazolinyl]pyridine molecule; Figure 1.4a). For stereoisomers emerging from free or restricted rotation of bonds, they are diastereomers.

Enantiomers have the same physical properties (solubilities, melting point) but different optical activity. When interacting with linearly polarised light, they will either rotate linearly polarised light clockwise (dextrorotary) or anticlockwise (levorotary). As the degree of optical rotation is dependent on the concentration of the enantiomers, there will be no optical rotation if an equal amount of *d*- and *l*-form enantiomers are present in a racemic mixture.

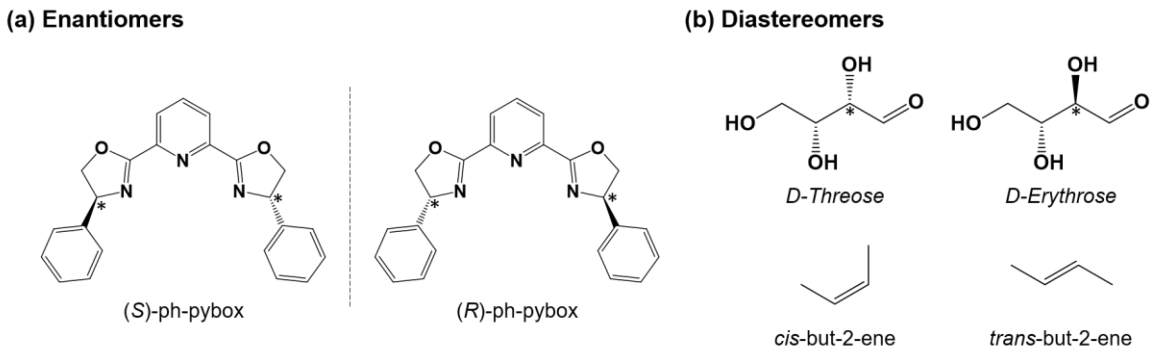

Figure 1.4. (a) Enantiomers of 2,6-Bis[(4*R*/4*S*)-4-phenyl-2-oxazolinyl]pyridine. (b) Diastereomers of D-Threose/Erythrose and cis-/trans-but-2-ene.

Chirality in organic molecules is usually realised by the asymmetric spatial arrangement of atoms in the molecules. For coordination complexes, asymmetric ligands arrangement around the metal centre could result in chirality in metal ion (Figure 1.5a). Besides, chirality in coordination compound could also be achieved by introducing chiral ligands to the metal centre ion (Figure 1.5b). In general, asymmetry is a main key lead to chiral property[7,8]. Thus, chiral molecules or compounds normally do not have inversion centre, improper rotation and reflection symmetries.

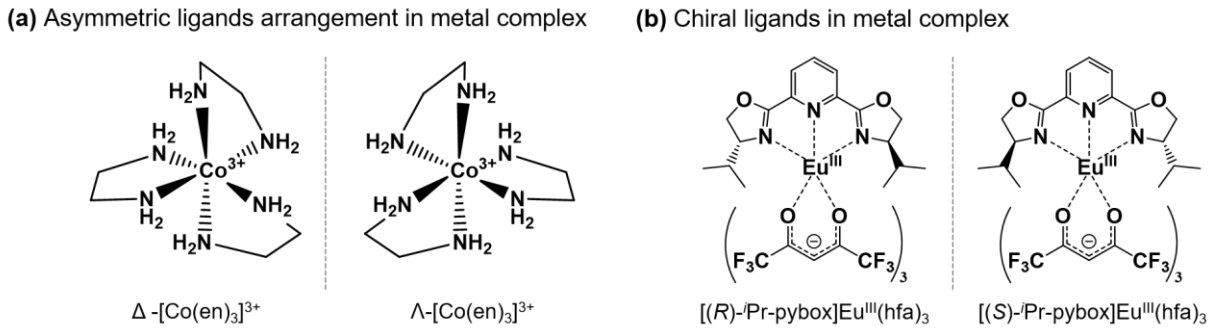

Figure 1.5. (a) Asymmetric en ligands arrangement in $[Co(en)_3]^{3+}$ complexes. (b) Chiral ^{i}Pr-pybox in [(*R*)-/(*S*)-^{i}Pr-pybox]$Eu^{III}(hfa)_3$ complexes[6].

1.2 Circularly Polarised Light and Luminescence

Polarised light is two-dimensional transverse wave, possessing 'handedness' once the electric and magnetic field with same amplitude are oscillating out of phase by 90˚ to each other[9]. The electric and magnetic vector can either rotate clockwise or anticlockwise to the propagation direction. It is known as right circularly polarised light if the light is rotating clockwise, and vice versa (Figure 1.6a).

Molecules can absorb photons and emit light at certain energies, producing their characteristic emission spectra. Upon photoexcitation, spontaneous emission of radiation generated from an electronically or vibrationally excited species not in thermal equilibrium with its environment is termed as photoluminescence[10]. Various internal energy transitions may occur before the excited molecular species emit light (Figure 1.6b). Once the light emit are circularly polarized, the process of emission is named as circularly polarised luminescence (CPL).

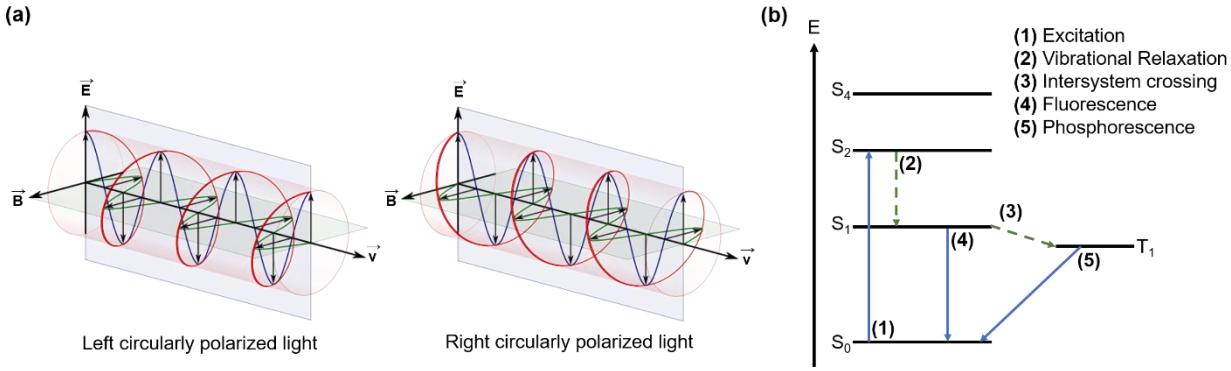

Figure 1.6. (a) Left and right circularly polarised light[9]. (b) Jablonski diagram.

In CPL spectroscopy[11], differential spontaneous emission of right and left circularly polarised radiation, ΔI by a luminophore is measured (*Eq.* 1, where I_L and I_R are the intensity of left and right circularly polarized radiation respectively). The degree of CPL activity can be assessed by the luminescence dissymmetry factor, g_{lum}. With a value range from -2 to 2, g_{lum} is defined as the ratio of the differential emission intensity to the average total emission intensity

(*Eq*. 2). The extra one-half factor included in *Eq*. 2 is to make the definition consistent with the g_{abs} factor in the circular dichroism (CD) spectroscopy (*Eq*. 3, where ε_L and ε_R are the molar absorption coefficients of left and right circularly polarized light respectively).

$$\Delta I \equiv I_L - I_R \qquad (Eq.1)$$

$$g_{lum} = \frac{\Delta I}{\frac{1}{2}I} = \frac{(I_L - I_R)}{\frac{1}{2}(I_L + I_R)} \qquad (Eq.2)$$

$$g_{abs} = \frac{\Delta\varepsilon}{\varepsilon} = \frac{(\varepsilon_L - \varepsilon_R)}{\frac{1}{2}(\varepsilon_L + \varepsilon_R)} \qquad (Eq.3)$$

Involving transition from *i* to *j*, the g_{lum} correlates with the magnetic and electric transition dipole vectors (*Eq*. 4, where μ_m and μ_e are magnetic and electric transition dipole vectors and $\theta_{u,m}$ is the angle between μ_m and μ_e). Since μ_m is generally much smaller than μ_e, $|\mu_m|^2$ in the denominator *Eq*.4 becomes negligible. Thus, g_{lum} becomes directly proportional to μ_m (*Eq*.5). Magnetic-dipole-allowed and electric-dipole-forbidden transitions usually give larger g_{lum} value.

$$g_{lum} = 4cos\theta_{u.m}\frac{|\mu_{e(ij)}||\mu_{m(ij)}|}{|\mu_{e(ij)}|^2 + |\mu_{m(ij)}|^2} \qquad (Eq.4)$$

$$g_{lum} = 4cos\theta_{u.m}\frac{|\mu_{m(ij)}|}{|\mu_{e(ij)}|} \qquad (Eq.5)$$

There are a large number of reported CPL-active chiral organic and inorganic molecular systems in recent years. Among them, chiral lanthanide (III) (Ln^{III}) complexes has been extensively studied for CPL experiment due to its unique emission from intraconfigurational *f-f* transitions. Up to date, the highest CPL performance for Ln^{III} system was achieved by cesium tetrakis(3-heptafluto-butyryl-(+)-camphorato) europium(III), $Cs[Eu^{III}((+)\text{-hfbc})_4]$ complexes, with a reported $|g_{lum}|$ of 1.38 in chloroform[12]. Enhancement of CPL activity of $Cs[Eu((+)\text{-hfbc})_4]$ can be induced through helical aggregation (g_{lum} = 1.45 in a mixture of chloroform and

hexane(1:24))[13] . Chiral organic molecules usually having smaller g_{lum} than Ln^{III} coordination compounds (within the 10^{-3} to 10^{-1} range)[14]. However, exceptional high g_{lum} (~1.6) has been realised by a light-emitting organic diode consisting 3-layered of chiral super-organized polymeric cholesteric crystals (PCCs) reflector[15].

1.2.1 CPL Measurement Technique

Optical design of CPL instruments is generally based on the oscillating quarter-wave plate system. Being a birefringence material, quarter-wave plate converts the circularly polarised light to linearly polarised light by advancing or retarding the incoming circularly polarised light by 90˚ in phase.

Mostly CPL experiments are carried out by hand-made CPL measurement systems. Figure 1.7a shows the schematic diagram of CPL instruments used in Photonic Molecular Science, NAIST[16]. The CPL-active sample is irradiated by a 375nm excitation continuous wave laser. The emitted circularly polarized light is then converted to linear polarised light by the photoelastic modulator (PEM). The PEM driven at frequency of 50 kHz control the retardation of the emitted light. The linear polarised signals at specific wavelength is then detected by photomultiplier tube (PMT) after passing the linear polarised cubic prism and monochromator. Differential emission, ΔI, and luminescence dissymmetry factor, g_{lum} are analysed and recorded on a hand-made system software.

By incorporating a set of optics (rotatable quarter-wave plate and linearly polarized plate) to a conventional spectrofluorometer, right and left circularly polarised components of a sample at specific wavelength can be resolved (Figure 1.7b)[17]. The emission intensity is periodically modulated with the rotating quarter wave-plate. The maximum and minimum intensity obtained at the angle of θ of 45˚, 225˚ and 135˚, 135˚ correspond to I_R and I_L,

respectively (Figure 1.8). The g_{lum} value can be evaluated using *Eq*. 2. Periodicity at every 90˚ indicate no linearly polarised component from the sample.

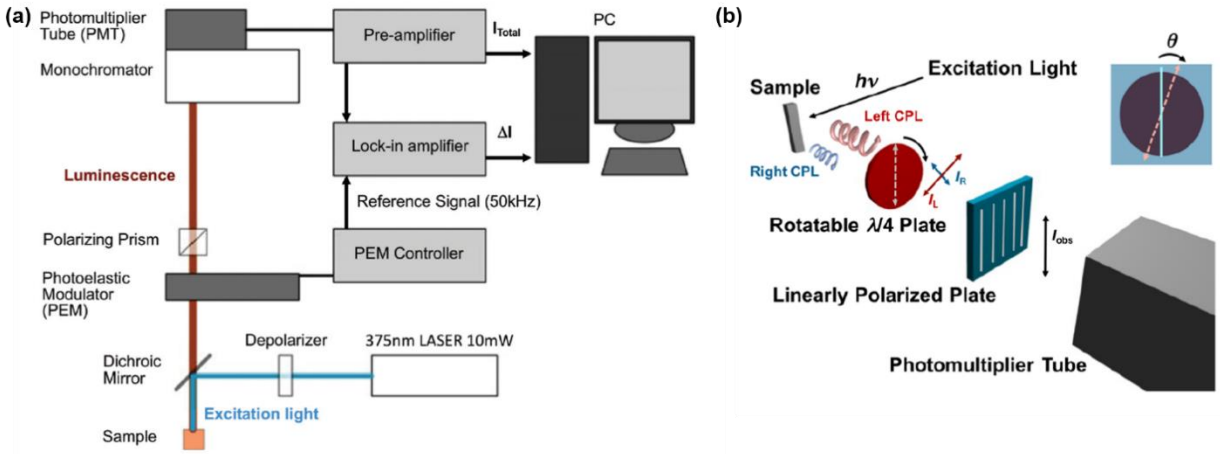

Figure 1.7. (a) Schematic diagram of CPL measurement system in Photonic Molecular Science Laboratory, NAIST[16]. (b) Schematic diagram of g_{lum} measurement system based on the conventional fluorescence spectrofluorometer[17].

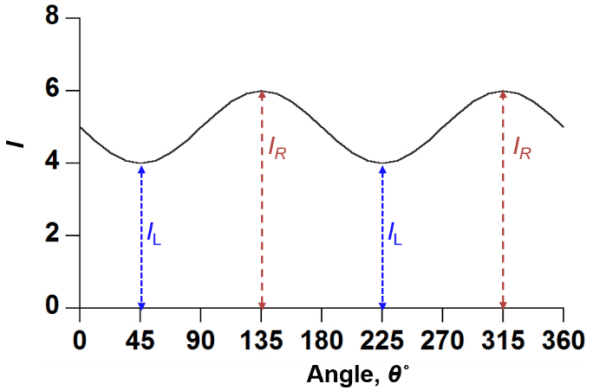

Figure 1.8. Emission intensity as a function of angle, *(θ)* between rotatable quarter-wave plate and linearly polarized plate obtained from the g_{lum} measurement system based on the fluorescence spectrofluorometer. *θ at* 45˚, 225˚ and 135˚, 135˚ corresponds to I_R and I_L, respectively (Figure 1.7b).

Practically, Figure 1.7a and Figure 1.7b instruments may be applicable for samples displaying $|g_{lum}| > 0.1$ since data processing capability are typically in the range of 100 to 10000 counts.

1.3 CPL Spectroscopy of Lanthanide Coordination Complexes

The lanthanide series comprises 15 elements with atomic number of 57 through 71, from lanthanum (La) through lutetium (Lu). They typically exist in +3 oxidation state in solution, since additional stabilization interactions associated with +3 charged ions can offset the energy used in removing *f* electrons. Involving *4f-4f* intraconfigurational transition, all the Ln^{III} (except for La^{III} and Lu^{III}) are luminescent upon excitation. Sharp and narrow Ln^{III} emission bands are always resulted from Ln^{III} luminescence, mostly in the region of visible or near-infrared. Due to the shielding effect of the *4f* orbitals $5p^6 6s^2$ subshells, direct Ln^{III} emission are weak as its low molar absorption extinction coefficient. Enhanced Ln^{III} emission is usually be achieved by sensitization mechanism, whereby appropriate ligands are used as antenna[57]. In such case, ligands absorb and transfer the excitation energy to the Ln^{III} core (Figure 1.9).

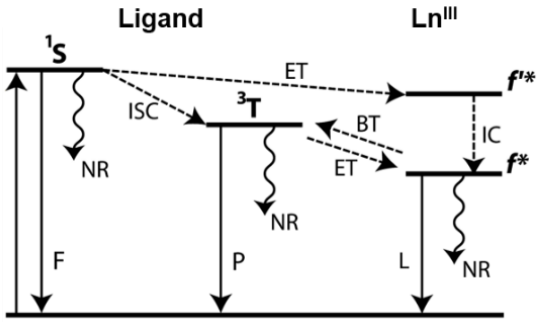

Figure 1.9. The mechanism of luminescence from Ln^{III} through ligand sensitization mechanism[11b].

Large circular polarization in the Ln^{III} is due to their *f-f* transitions which can be either magnetic or electric dipole character transition. Since the g_{lum} is directly proportional to magnetic dipole strength (Eq.5), the magnetic dipole transition is always the transition of interest in the CPL spectroscopy. Due to different *f-f* transitions having different electric and magnetic dipole strength, different Ln^{III} exhibit different g_{lum} in the same coordination system. The Eu^{III} ion is found to be the most accessible to CPL activity. Upon excitation, Eu^{III} complexes give characteristics red ($^5D_0 \rightarrow {}^7F_J$, J = 0-4) luminescence (Figure 1.10). The

$^5D_0 \rightarrow {}^7F_1$ transition satisfies the magnetic-dipole selection rule, $\Delta J = 0, \pm 1$(except $0 \leftrightarrow 0$), which is the transition interest for CPL activity.

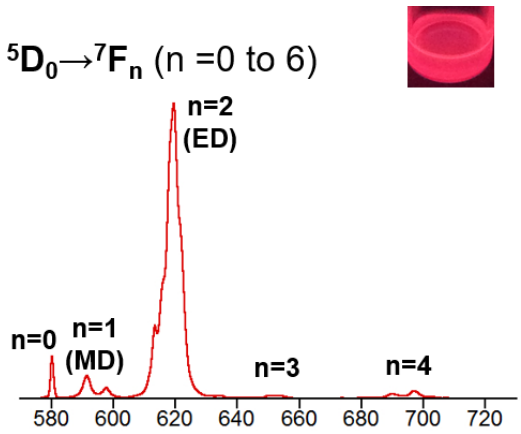

Figure 1.10. Typical Eu^{III} emission profile.

The *f-f* transitions are perturbed by the crystal field splitting. Thus, Ln^{III} site symmetry is believed to be the main clue for understanding the structure and spectra relationship. Typical coordination numbers of Ln^{III} are eight and nine, which can exhibit square antiprism (8), tricapped trigonal prism (9) and capped square antiprism (9) geometries (Figure 1.11). The Eu^{III} site symmetry can be assessed by the relative total intensities of hypersensitive $^5D_0 \rightarrow {}^7F_2$ transition to $^5D_0 \rightarrow {}^7F_1$ transition, A_{rel}(TI). The larger the A_{rel}(TI) value corresponds to the lower the symmetry of the Eu^{III} coordination geometries. Although a more distorted coordination geometry promises a better understanding of g_{lum}, there has been no common knowledge on the relationship between the Eu^{III} site symmetry and the g_{lum} value.

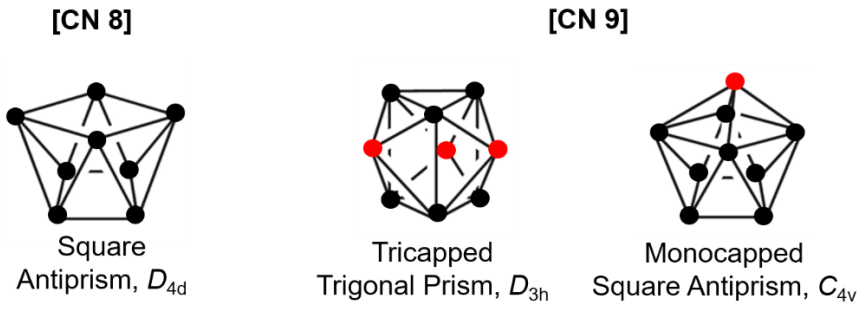

Figure 1.11. Eight- and nona-coordination geometry of Ln^{III} [11b].

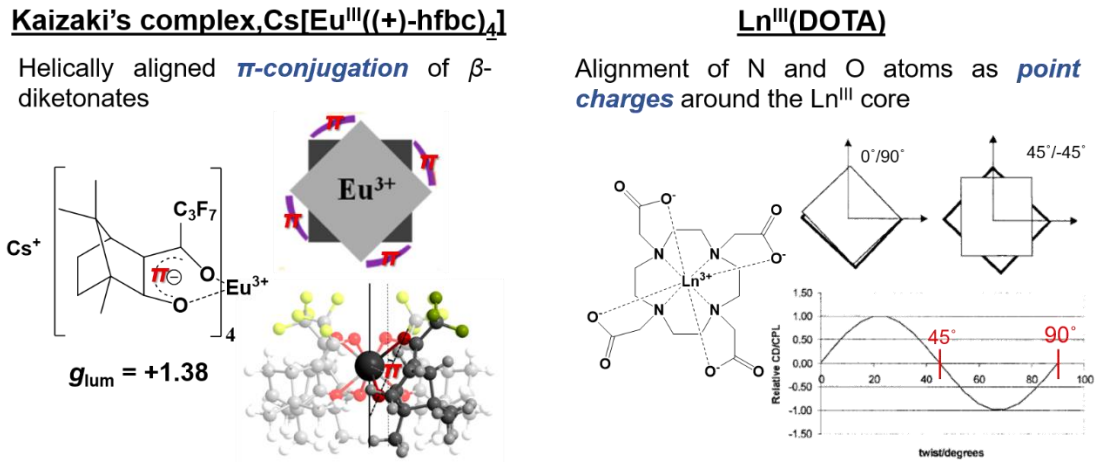

Figure 1.12. (Left) The dynamic coupling mechanism of $Cs[Eu^{III}((+)\text{-hfbc})_4]$ and (Right) static coupling mechanism of $Ln^{III}(DOTA)$[19, 20].

The *f-f* transitions may gain intensity by static and dynamic coupling mechanism[18]. Static coupling mechanism explains the ligand as point charges interacting to Ln^{III} transitions, whereas dynamic coupling mechanism propose ligand polarisation to the Ln^{III} transitions. In $Cs[Eu^{III}((+)\text{-hfbc})_4]$ (g_{lum} ~1.38, the) and Ln^{III}-DOTA (g_{lum} ~0.1), the contribution of the static coupling mechanism to the luminescence dissymmetry was discussed through the twist angle in the axially symmetric square antiprism or capped square antiprism geometry. They proposed that the CPL activity must be vanished at twist angle of 0˚, 45˚, and 90˚. Both systems are eight-coordinated and exhibit twist angle of about 40°. A study reported by Di Bari et al. suggested that through the dynamic coupling mechanism, skewness of the four diketonates plane from the main symmetry axis relatively close to ideal angle could largely result in such high g_{lum} (~1.38, the highest among Ln inorganic system) to be observed in the $Cs[Eu^{III}((+)\text{-hfbc})_4]$ system[19]. The induced polarisation on the four helically aligned *β*-diketonates (hfbc) ligands promotes dominant electromagnetic interactions with the Europium (III) (Eu^{III}) metal centre *f-f* transitions, breaking a nearly symmetric Eu^{III} coordination environment (Figure 1.12). In this consideration, the π electron system of ligands perturb the Eu^{III} emission, promoting coupling between electronic transition and transverse light wave.

Besides the degree of helical twist of the complex, Bruce et al.[20] reported other factors determining the g_{lum} based on the well-defined DOTA-based macrocycle Eu^{III} complexes, such as the axial donor group solvation, the nature of ligand field and the degree of conformational rigidity of the complex.

Any changes found in the primary Eu^{III} coordination sphere in each chiral system are apparent in the CPL spectra. Kawai et al.[16] have reported that different asymmetric arrangement in Eu^{III} nona-coordination sphere of [(*R*)- or (*S*)-Ph-pybox]$Eu^{III}(hfa)_3$, and [(*R*)- or (*S*)-^{i}Pr-pybox]$Eu^{III}(hfa)_3$ induce opposite sense of CPL activity (Figure 1.13). In the CPL spectra of [(*R*)-Ph-pybox]$Eu^{III}(hfa)_3$, the sign of CPL follows the sequence of +, - at the $^5D_0 \rightarrow {}^7F_1$ and $^5D_0 \rightarrow {}^7F_2$ transitions, respectively (Figure 1.13a). In contrasts, the sign of CPL follow the sequence of -, + at the $^5D_0 \rightarrow {}^7F_1$ and $^5D_0 \rightarrow {}^7F_2$ transitions, respectively in the CPL spectra of [(*R*)- or (*S*)-^{i}Pr-pybox]$Eu^{III}(hfa)_3$ (Figure 1.13b). Different non-covalent π-π stacking and CH/F ligand-ligand interactions between pybox and β-diketonates ligands are found to induce different asymmetric arrangement in primary coordination sphere, and thus alter the sense of optical chirality.

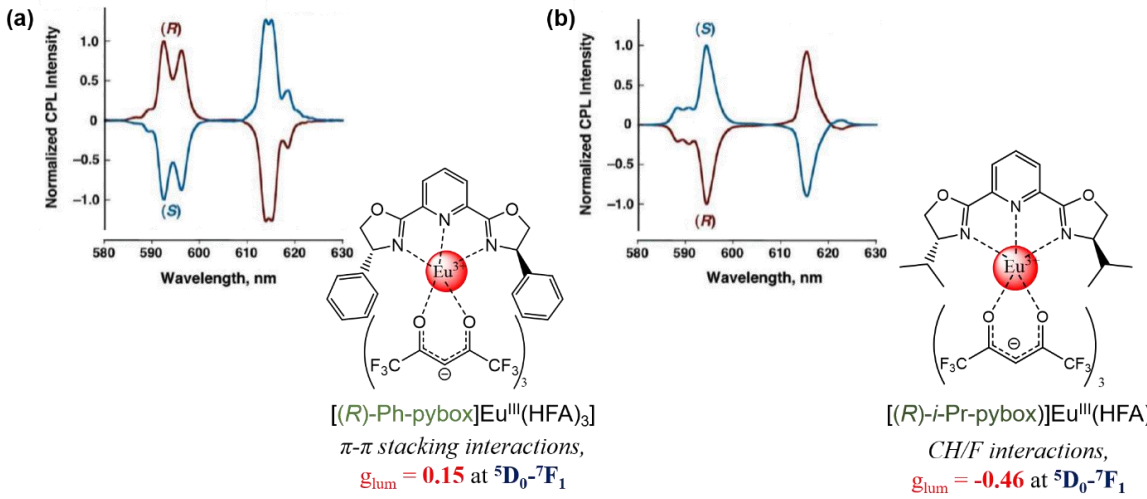

Figure 1.13. Normalised CPL spectra of (a) [(*R*)- or (*S*)-Ph-pybox]$Eu^{III}(hfa)_3$ and (b) [(*R*)- or (*S*)-^{i}Pr-pybox]$Eu^{III}(hfa)_3$[16].

1.4 Research Objectives

CPL has attracted a lot of attention due to its potential applications in optoelectronic devices[21] and optical sensors[22-26]. Thus, developing useful chiral structure-CPL spectra correlation is crucial for designing functional CPL materials (with large g_{lum} and emission quantum yield). However, it is still a challenge as most of CPL measurements are carried out in solution. Structure diversity in solution should be first considered before evaluating structural origin of CPL activity. It has been reported that quasi-racemization structures suppresses CPL activity of some chiral mononuclear Ln^{III} complexes[54-55]. To suppress the structural fluctuation in solution phase, multivalent coordination chemistry has been introduced. Besides, closed, polynuclear complexes have also been considered to be kinetically inert and promising less solution structure dynamic[27-34]. The aim of this research work is to prepare a series of new CPL-active, closed polynuclear Ln^{III} helicates (in particular, circular helicate and cage) and study their possible structure-spectra relationship for higher CPL activity. It should be noticed that limited reports on octa-coordinated Ln^{III} circular helicate were studied at the starting of this research project.

Herein, three new different types of polynuclear, nona-coordinated Ln^{III} self-assemblies based on the achiral tetravalent bis-β-diketonates or hexavalent tris-β-diketonates and chiral pybox ligands were synthesized and characterized (Figure 1.14). Design, preparation, and structural and photophysical characterization of each type of self-assemblies will be discussed in Chapter 2, 3, and 4.

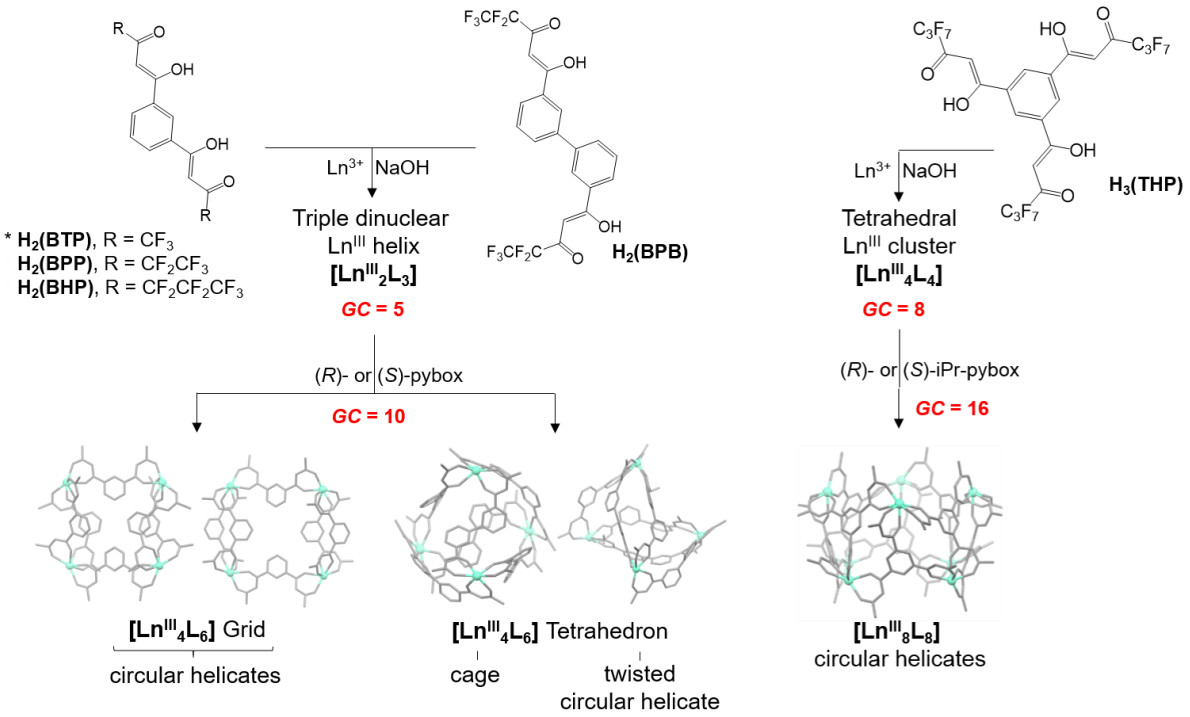

Figure 1.14. Reaction scheme of $[Ln^{III}_4L_6]$ grid or tetrahedron and $[Ln^{III}_8L_8]$ square antiprism.

2.0 CHIRAL SELF-ASSEMBLED OF QUADRILATERAL $Ln^{III}_4L_6(Pybox)_4$ GRID

2.1 Introduction

Despite versatile and high Ln^{III} coordination numbers impose a difficultly in controlling the formation of polynuclear complexes or self-assemblies, there are still a number of reported studies on the formation of dinuclear $Ln^{III}_2L_3$ and trinuclear $Ln^{III}_3L_3$ helicates[35-38], trinuclear $Ln^{III}_3L_6$ self-assembly[39], trinuclear $Ln^{III}_3L_2$ complexes[40], tetranuclear tetrahedral lanthanide $Ln^{III}_4L_6$ cluster[41-44], and cation assisted hexameric europium $[Eu^{III}_6L_{12}]$ wheel[45]. In particular, Senegas et al.[46] have successfully isolated first example of D_3-symmetrical circular Ln^{III} helicates[47-49] by using the effect of global complexity (GC = sum of the number coordinating metal ions, *m* and bridging ligands, *n* (GC = *m* + *n*) ; GC of $Ln^{III}_3L_3$ = 3+3 = 6). They pointed out the crucial role of GC over the influence of the stoichiometry ratio in self-assembly process. Different factors (for instance, counter-ion templating effect) affect the preferential formation of the complexes with GC of x over other complexes with GC of y.

In this chapter, by using the GC strategy, a series of nanometer-sized tetranuclear alternating circular Ln^{III} helicate based on achiral anionic bis-*β*-diketonates, L ligands and chiral Pybox ligands, with a general formula of $[Pybox]_4Eu_4L_6$ (GC = 4 +6 =10) were successfully fabricated through ligand-to-ligand interactions. π-π or CH-π interactions observed in the X-ray crystal structure thermodynamically stabilize the circular helicates in polar or non-polar solvent medium. All the circular helicates exhibit large circular polarization in solution with different chiroptical performance ($|g_{lum}|$ = 0.08 to 0.31).

2.2 Preparation

Bridging ligands of fluorinated bis-*β*-diketonate, H_2L [H_2(BTP), H_2(BPP), H_2(BHP)] can be synthesized from the Claisen Condensation between 1,3-bis-acetophenone and two non-enolizable trifluoroethyl acetate, ethyl pentafluoropropionate or ethyl heptafluorobutyrate (Figure 2.1).

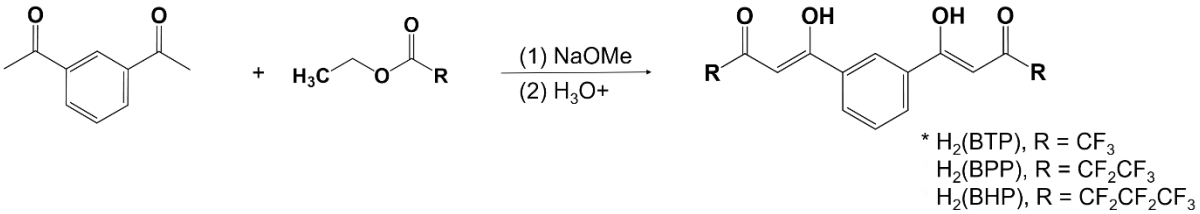

Figure 2.1. Reaction scheme of H_2(BTP), H_2(BPP), H_2(BHP) ligands

Bis-*β*-diketonate chelated Eu^{III} precursor complexes can be prepared by reacting the ligand, H_2L with Eu^{III} chloride hexahydrate ($Eu^{III}Cl_3.6H_2O$) in an appropriate ratio under basic condition. Deprotonation of bis-*β*-diketonate, H_2L by sodium hydroxide (NaOH) resulted in the formation of anionic ligand with doubly negative charges, L. The chelating anionic ligand can react with the trivalent Eu^{III} ions, Eu^{III} in a 3:2 ratio, producing neutral, dinuclear triple helix, [$Eu^{III}_2L_3$] (Figure 2.2)[51]. The [$Eu^{III}_2L_3$] helicate contains solvent molecules weakly bound to each Eu^{III} ions. Single crystal suitable for analysis can be obtained from the slow evaporation of hexane into the dimethoxyethane (DME) solution containing sample. DME solvent molecules coordinated to Eu^{III} ions in recrystallisation process, generating crystal structure of $Eu^{III}_2L_3(DME)_2$ (Figure *A1-2*, refer to Table *A2* for crystallographic data). [Tb^{III}_2(BTP)$_3$] and [Sm^{III}_2(BTP)$_3$] can be prepared in a similar manner as [Eu^{III}_2(BTP)$_3$]

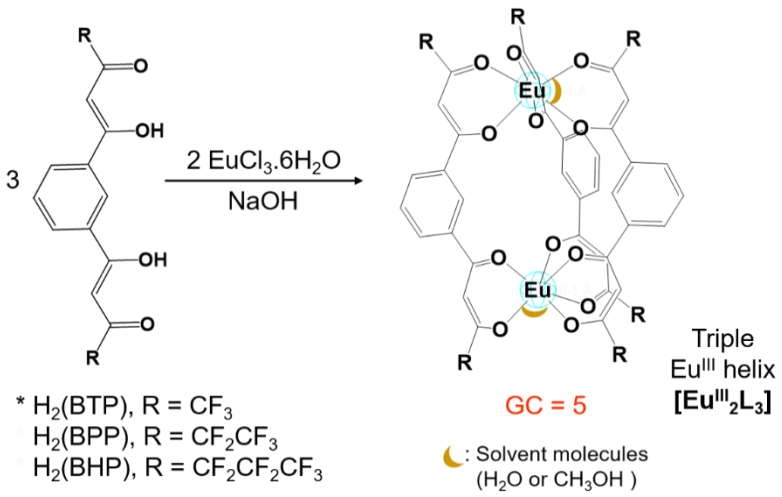

Figure 2.2. Reaction scheme of $[Eu^{III}_2L_3]$, L= BTP, BPP, and BHP.

Further reaction of the dinuclear triple helix with the (*R)* or (*S)*-pybox ligand results tetranuclear Ln^{III} self-assemblies with the general formula of [(*R)* or (*S)*-Pybox)$_4$]$Ln^{III}_4L_6$ (Figure 2.3). Chiral D_2-symmetrical quadrilateral grid-like self-assemblies are produced from the reaction of $[Ln^{III}_2L_3]$ (L = BTP, BPP, BHP) with chiral Ph-pybox ligand {Self-assemblies with D_2 symmetry: [(*R*)- or (*S*)-Ph-Pybox]$_4Eu^{III}_4$(BTP)$_6$ (**1-Eu^{Ph}*RRRR*/1-Eu^{Ph}*SSSS***), [(*R*)- or (*S*)-Ph-Pybox]$_4Sm^{III}_4$(BTP)$_6$ (**1-Sm^{Ph}*RRRR*/1-Sm^{Ph}*SSSS***), [(*R*)- or (*S*)-Ph-Pybox]$_4Tb^{III}_4$(BTP)$_6$ (**1-Tb^{Ph}*RRRR*/1-Tb^{Ph}*SSSS***), [(*R*)- or (*S*)-Ph-Pybox]$_4Eu^{III}_4$(BPP)$_6$ (**2-Eu^{Ph}*RRRR*/2-Eu^{Ph}*SSSS***), and [(*R*)- or (*S*)-Ph-Pybox]$_4Eu^{III}_4$(BHP)$_6$ (**3-Eu^{Ph}*RRRR*/3-Eu^{Ph}*SSSS***)}. The reaction of $[Eu^{III}_2(BPP)_3]$ with chiral ^{i}Pr-pybox ligand afford pseudo C_{2h}-symmetrical quadrilateral grid-like self-assemblies, [(*R*)- or (*S*)-^{i}Pr-Pybox]$_4Eu^{III}_4$(BPP)$_6$ (**2-Eu^{iPr}*RRRR*/2-Eu^{iPr}*SSSS***)}. Suitable single crystal for analysis can be obtained in toluene/diethyl ether, ethyl acetate/hexane, methyl ethyl ketone (MEK)/ethanol or acetone/pentane solvent pairs.

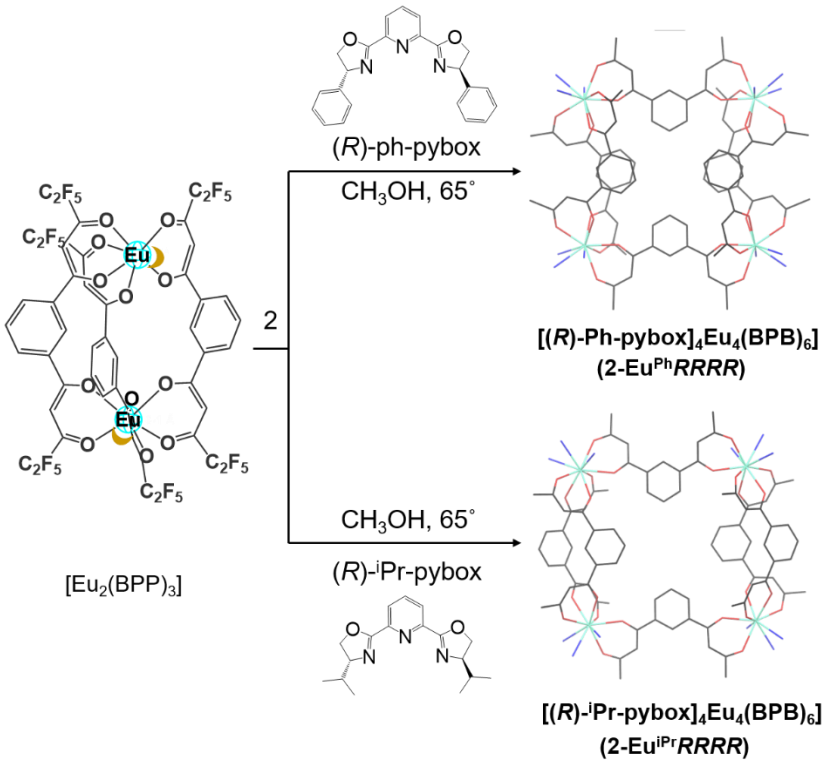

Figure 2.3. Reaction Scheme of **2-Eu^{Ph}*RRRR*** and **2-Eu^{iPr}*RRRR***.

2.3 Crystal structure

Figure 2.4 shows the crystal structures of **1-Eu^{Ph}*RRRR*/1-Eu^{Ph}*SSSS*, 2-Eu^{Ph}*RRRR*/2-Eu^{Ph}*SSSS*** and **2-Eu^{iPr}*RRRR*/2-Eu^{iPr}*SSSS***, where the *R*- and *S*-isomers are non-superimposable complete mirror images of each other (refer to Table *A4*, *A6*, and *A7* for crystallographic data). **1-Eu^{Ph}*RRRR*/1-Eu^{Ph}*SSSS*** are crystallized in monoclinic with space group of *C*2 whereas **2-Eu^{Ph}*RRRR*/2-Eu^{Ph}*SSSS*** are crystallized in tetragonal crystal system with space group of *P*422. Crystals of **2-Eu^{iPr}*RRRR*/2-Eu^{iPr}*SSSS*** pack in monoclinic crystal system with space group of $P2_1$. Due to high disordering of the heptafluoropropyl units of BHP ligands and the phenyl arm-units of Ph-Pybox ligands, good resolved structures of **3-Eu^{Ph}*RRRR*/3-Eu^{Ph}*SSSS*** could not be obtained. Their tetranuclear structures are revealed to be alike with **2-Eu^{Ph}*RRRR*/2-Eu^{Ph}*SSSS*** (Figure *A6*).

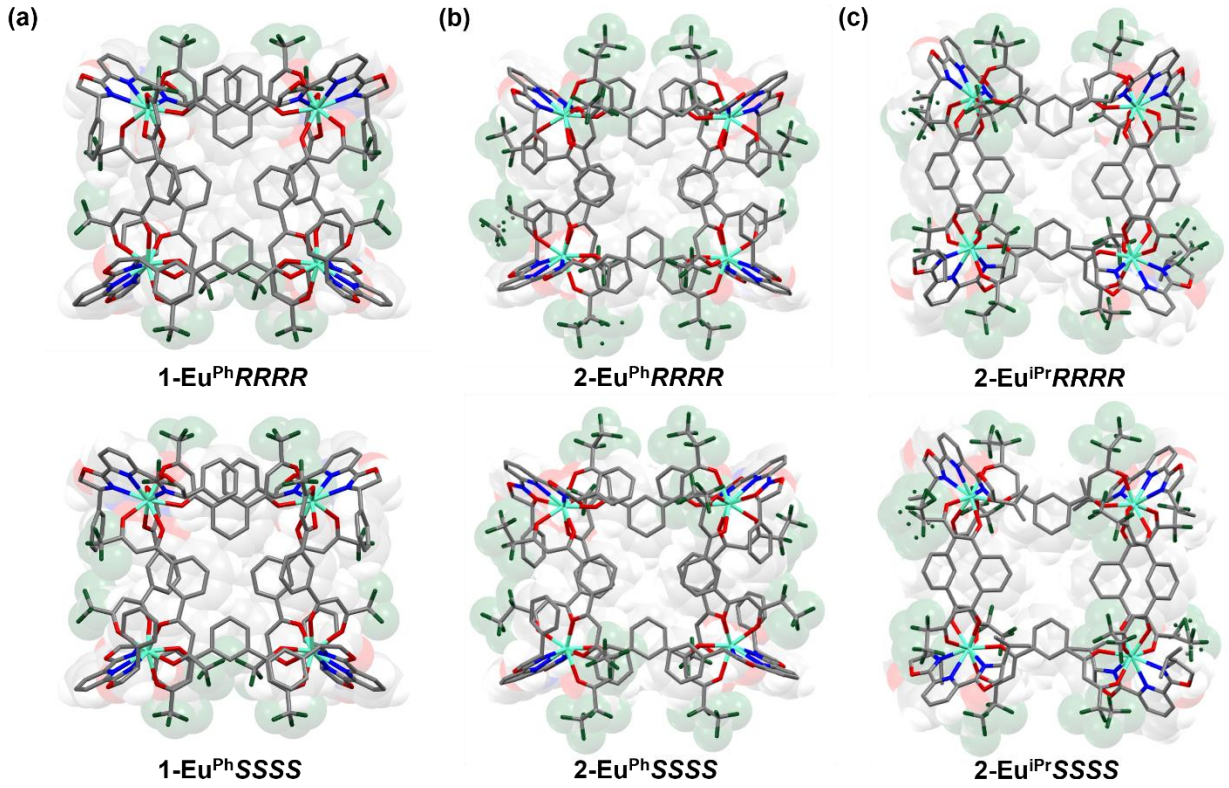

Figure 2.4. X-ray crystal structure of (a) **1-Eu^{Ph}*RRRR*** and **1-Eu^{Ph}*SSSS*, (b) 2-Eu^{Ph}*RRRR*** and **2-Eu^{Ph}*SSSS*** and (c) **2-Eu^{iPr}*RRRR*** and **2-Eu^{iPr}*SSSS***.

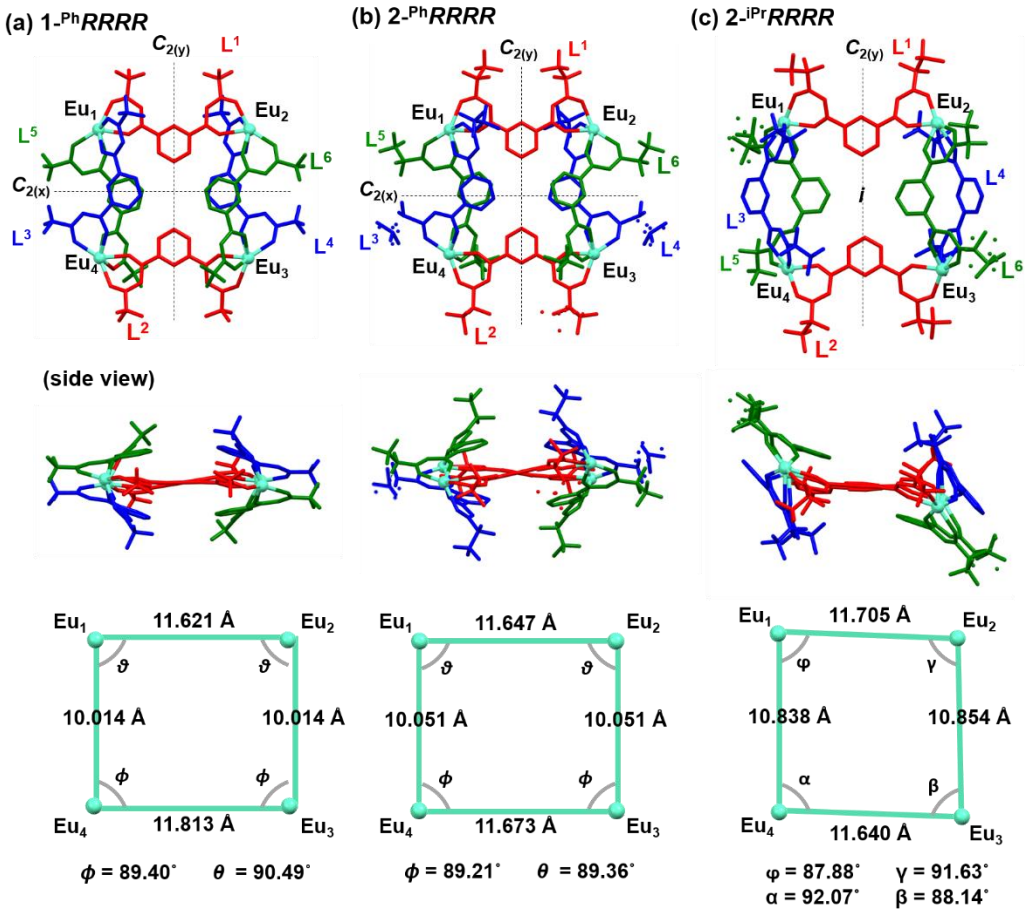

Figure 2.5. $Eu^{III}_4L_6$ core structure, Eu-Eu distances and Eu-Eu-Eu angles of (a) **1-Eu^{Ph}*RRRR***, **(b) 2-Eu^{Ph}*RRRR*** and (c) **2-Eu^{iPr}*RRRR*** *(The σ_h symmetry is strictly applied to Eu_4L_6 core structure)*.

Structures of **1-Eu^{Ph}*RRRR*/1-Eu^{Ph}*SSSS*, 2-Eu^{Ph}*RRRR*/2-Eu^{Ph}*SSSS*** and **3-Eu^{Ph}*RRRR*/2-Eu^{Ph}*SSSS*** can be considered as D_2-symmetrical quadrilateral grid, composing two [(*R*)- or (*S*)-Ph-Pybox]$_2Eu^{III}_2L_3$ which arrange in alternating, closed cyclic manner to form an alternating circular helicate. Similarly, two [(*R*)- or (*S*)-^{i}Pr-Pybox]$_2Eu^{III}_2$(BPP)$_3$ arrange in alternating, closed cyclic form to give pseudo C_{2h}-symmetrical grid-like **2-Eu^{iPr}*RRRR*/2-Eu^{iPr}*SSSS*** circular helicate. Four nona-coordinated Eu^{III} with same chirality define the vertices of the grid, whereas six L ligands occupy four edges of the grid in 2:1:2:1 fashion, connecting four Eu^{III} ions together. To be noted that, perfect D_2- or C_{2h}-symmetry is not observed in their crystal structures. Thus, minor variations in the Eu-Eu distances, Eu-Eu-Eu angles and dihedral angle of L are found in each crystal structures (Figure 2.5).

In **1-Eu^{Ph}*RRRR*/1-^{P}Eu^{h}*SSSS*** and **2-Eu^{Ph}*RRRR*/2-^{Ph}Eu*SSSS***, a $C_{2(y)}$ rotational symmetry in the crystal structures involves a pair of two equivalent Eu^{III} ions ($Eu_1 = Eu_2$ and $Eu_3 = Eu_4$) (Figure 2.5a and b). Besides, a pair of interior angles (~89˚) close to the right angle are observed for Eu_1-Eu_2-Eu_3 and Eu_1-Eu_4-Eu_3. In contrasts, crystal structures of **2-Eu^{iPr}*RRRR*/2-Eu^{iPr}*SSSS*** revealed four different interior angles (~89˚) (Figure 2.5c). The sum of the four interior angles are 359.78˚, 357.1˚ and 359.7˚ in **1-Eu^{Ph}*RRRR***, **2-Eu^{Ph}*RRRR*** and **2-Eu^{iPr}*RRRR*** respectively, suggesting different Eu-Eu-Eu-Eu co-planarity.

Table 2.1. Dihedral angle of BTP or BPP ligands in the X-ray crystal structure of **1-Eu^{Ph}*RRRR*/1-Eu^{Ph}*SSSS***, **2-Eu^{Ph}*RRRR*/2-Eu^{Ph}*SSSS*,** and **2-Eu^{iPr}*RRRR*/2-Eu^{iPr}*SSSS***.

Eu^{III} self-assemblies	Degree of ligand twisting (˚)					
	L_A		L_B		L_C	
	L^1	L^2	L^3	L^4	L^5	L^6
1-Eu^{Ph}*RRRR*	-23.42	35.38	78.77	78.77	81.09	81.09
1-Eu^{Ph}*SSSS*	24.61	-34.96	-78.33	-78.33	-81.30	-81.30
2-Eu^{Ph}*RRRR*	-35.22	-12.32	83.48	83.48	77.87	77.87
2-Eu^{Ph}*SSSS*	36.07	8.83	-86.72	-86.72	-77.05	-77.05
2-Eu^{iPr}*RRRR*	-55.70	56.60	-2.63	-0.06	4.02	-3.77
2-Eu^{iPr}*SSSS*	56.46	-56.24	2.20	0.01	-4.26	4.20

Each L coordinates to two Eu^{III} ions as a helicate ligand. Taking into symmetry consideration, six L can be categorized into three type, L_A (L^1, L^2; red), L_B (L^3, L^4; blue) and L_C (L^5, L^6; green). L_B and L_C are similar in **1-Eu^{Ph}*RRRR*/1-Eu^{Ph}*SSSS*** and **2-Eu^{Ph}*RRRR*/2-^{Ph}Eu*SSSS***, but dissimilar in **2-Eu^{iPr}*RRRR*/2-Eu^{iPr}*SSSS***. The ligand twisting angles of L_B and L_C in **1-Eu^{Ph}*RRRR*/1-Eu^{Ph}*SSSS*** and **2-Eu^{Ph}*RRRR*/2-^{Ph}Eu*SSSS*** are differ by 5°, whereas two L_A differ ~10° and ~25° in magnitude in **1-Eu^{Ph}*RRRR*/1-Eu^{Ph}*SSSS*** and **2-Eu^{Ph}*RRRR*/2-^{Ph}Eu*SSSS*** respectively. Conversely, two L_A in **2-Eu^{iPr}*RRRR*/2-Eu^{iPr}*SSSS*** shows similar twisting angles (±56^{o}) with opposite sign to each other whereas the L_B and L_C are almost coplanar with dihedral angle less than 5^{o} (Table 2.1). The chiral ligand twisting angle is

determined from the dihedral angle between two β-diketonate planes on each BPP ligand from the corresponding Eu^{III} ions (refer to Figure *A26* for definition).

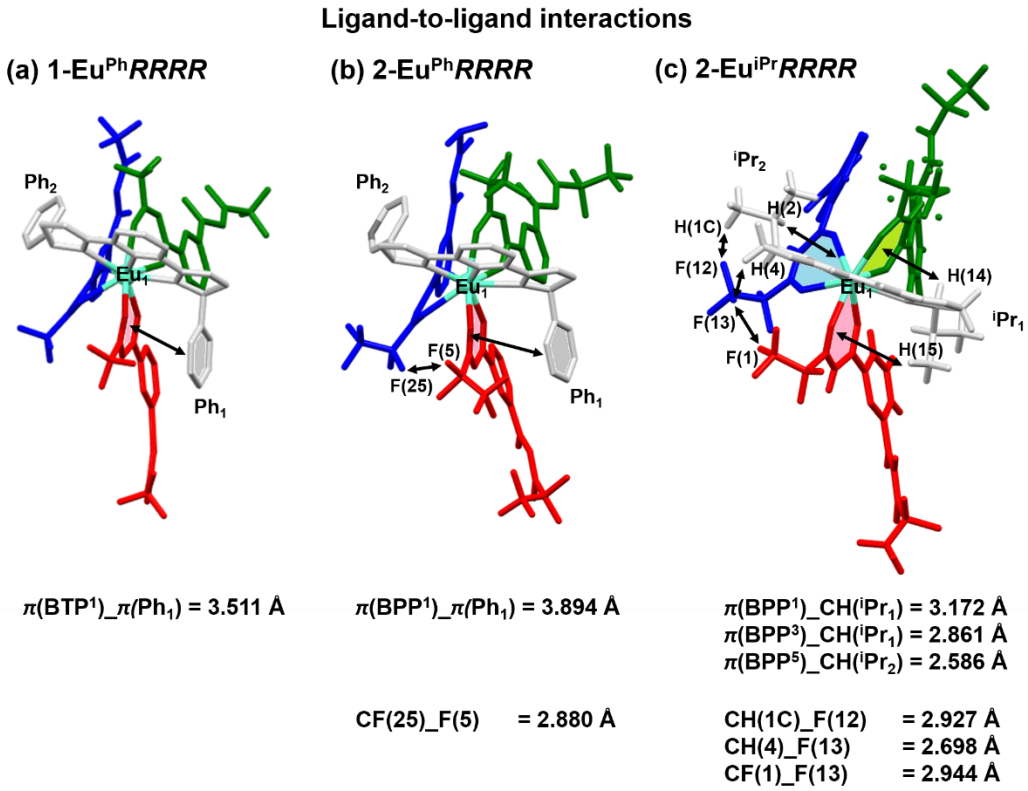

Figure 2.6. Ligand-to-ligand interactions of (a) **1-Eu^{Ph}*RRRR*** (b) **2-Eu^{Ph}*RRRR*** and (c) **2-Eu^{iPr}*RRRR***.

X-ray crystallography analysis revealed that ligand-to-ligand interactions between Pybox and β-diketonate moiety in the crystal structures facilitate the formation of circular helicates structures with different L arrangements around Eu^{III} ions. In **2-Eu^{iPr}*RRRR*/2-Eu^{iPr}*SSSS***, there are typical CH_π interactions between the isopropyl arm ($^{i}Pr^{1}$ and $^{i}Pr^{2}$) of ^{i}Pr-pybox ligand and β-diketonates moieties of the adjacent BPP (L_A, L_B, and L_C) ligands around Eu_1 (Figure 2.6c). In contrast, π-π stacking interaction between the phenyl arm (Ph^{1}) of Ph-Pybox and the β-diketonates moiety of the adjacent BTP or BPP ligand (L_A) around Eu^{III} ions are observed in **1-Eu^{Ph}*RRRR*/1-Eu^{Ph}*SSSS*** and **2-Eu^{Ph}*RRRR*/2-^{Ph}Eu*SSSS***. The other phenyl arm (Ph^{2}) of Ph-pybox has no appreciable contact with the adjacent BTP or BPP ligands (L_B,

and L_C) (Figure 2.6a and b). Lacking of such interactions allows helix twisting of L_B, and L_C ligands around the Eu^{III} ions, forming two $[Eu^{III}_2(L)_2]$ helical chains in **1-Eu^{Ph}*RRRR*/1-Eu^{Ph}*SSSS*** and **2-Eu^{Ph}*RRRR*/2-^{Ph}Eu*SSSS*** structures (*M*- or *P*-helix *R* and *S* isomer, respectively). In addition to the mentioned interactions, intramolecular CF_F interactions between BPP ligands and CF_H interactions between BPP ligand and ^{i}Pr-pybox ligand can also be found in the crystal structures of **2-Eu^{Ph}*RRRR*/2-^{Ph}Eu*SSSS*** and **2-Eu^{iPr}*RRRR*/2-Eu^{iPr}*SSSS***. Detailed contacting interactions are summarized in Table *A16*.

All the Eu^{III} cores are nona-coordinated with three nitrogen atoms of the Pybox ligand and six oxygen atoms of three *β*-diketonates moieties of L (Figure 2.7). Two typical geometries generally known for describing the nona-coordination systems are the D_{3h} tricapped-trigonal prism (TTP) and C_{4v} capped square antiprism (SAP). The primary Eu^{III} coordination spheres of **1-Eu^{Ph}*RRRR*/1-Eu^{Ph}*SSSS***, **2-Eu^{Ph}*RRRR*/2-^{Ph}Eu*SSSS*** and **2-Eu^{iPr}*RRRR*/2-Eu^{iPr}*SSSS*** have distorted capped SAP geometry. A basal quadrate plane in each Eu^{III} capped SAP geometry is existing perpendicularly to the pseudo-C_4 main symmetry axis. The main axis of capped SAP is determined from minimal deviation of all observed dihedral angle along each edge ($\delta^{1\text{-}21}$) from the ideal estimated angles (θ of $E_{a\text{-}e}$, Figure 2.7, Figure *A9-A10* and Table *A11-A13*). The dihedral angle along the diagonal edge of the square base (δ^{21}) of the Eu^{III} circular helicates are in a range of 151° to 172°, as shown in Figure 2.7b and c.

Distinct arrangements of the L ligands in these self-assemblies induce difference the outer-sphere coordination orientations of a Pybox (N-N-N; blue circles) and three BPP ligands (O-O; red circles) arounds the Eu ions. The Ph-Pybox ligand is skewed with an angle from the main axis in the Eu^{III} coordination geometries of **1-Eu^{Ph}*RRRR*/1-Eu^{Ph}*SSSS*** and **2-Eu^{Ph}*RRRR*/2-^{Ph}Eu*SSSS***, whereas ^{i}Pr-Pybox ligand caps on the top in the Eu^{III} coordination geometries of **2-Eu^{iPr}*RRRR*/2-Eu^{iPr}*SSSS***. Besides, there is no difference found in the *β*-diketonates orientations in each of the four Eu^{III} cores of **1-Eu^{Ph}*RRRR*/1-Eu^{Ph}*SSSS*** and **2-**

Eu^{Ph}*RRRR*/2-^{Ph}Eu*SSSS*, under differentiating two oxygen atoms that directly bonded to the Eu^{III} ions as oxygen atoms next to the fluoroalkyl chains O(A) and phenyl rings O(B) (Figure 2.7b, linkage of fluoroalkyl groups was marked with the green triangle). In contrast, there is a pair of distinguishable Eu^{III} coordination geometries (Eu$_1$ ≈ Eu$_2$ and Eu$_3$ ≈ Eu$_4$) in **2-Eu^{iPr}*RRRR*/2-Eu^{iPr}*SSSS***. The *β*-diketonate moeities in Eu$_1$/Eu$_2$ coordination sphere orientates oppositely to the Eu$_3$/Eu$_4$, as shown in Figure 2.7c. The quasi-mirror image Eu^{III} coordination geometries observed in **2-Eu^{iPr}*RRRR*/2-Eu^{iPr}*SSSS*** is consistent with the pseudo C_{2h} symmetrical structure.

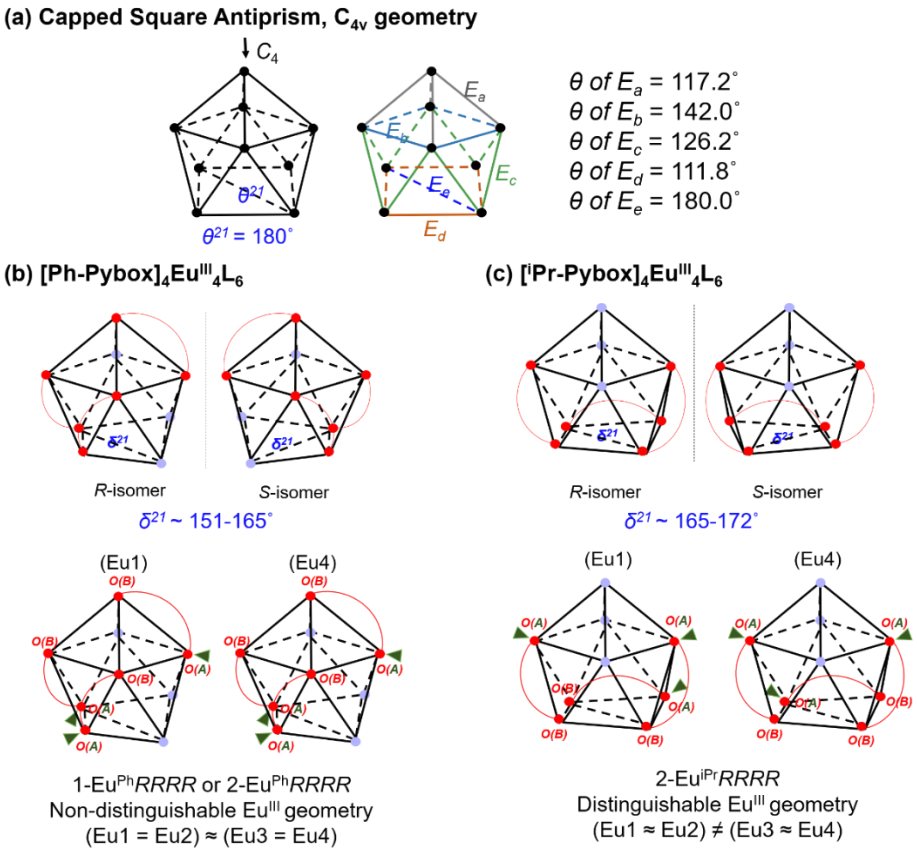

Figure 2.7. (a) Perfect capped SAP geometry. Eu^{III} coordination geometries of (a) [(*R*) or (*S*)-Py-Pybox)$_4$]Eu$^{III}{}_4$L$_6$ and (b) [(*R*) or (*S*)-^{i}Pr-Pybox)$_4$]Eu$^{III}{}_4$L$_6$. O(A) and O(B) are oxygen atoms in the carbonyl units of bis-*β*-diketonate ligands which are next to the fluoroalkyl chains and phenyl rings, respectively. Green triangles in the Eu geometries designate linkage of the fluoroalkyl chain.

Chiral self-assemblies of **1-Tb^{Ph}*RRRR*/1-Tb^{Ph}*SSSS*** and **1-Sm^{Ph}*RRRR*/1-Sm^{Ph}*SSSS*** are isomorphous of the **1-Eu^{Ph}*RRRR*/1-Eu^{Ph}*SSSS***. Their X-ray crystal structures are given in the Figure *A5* (refer to Table *A5*-*6* for crystallographic data).

2.4 NMR Analysis

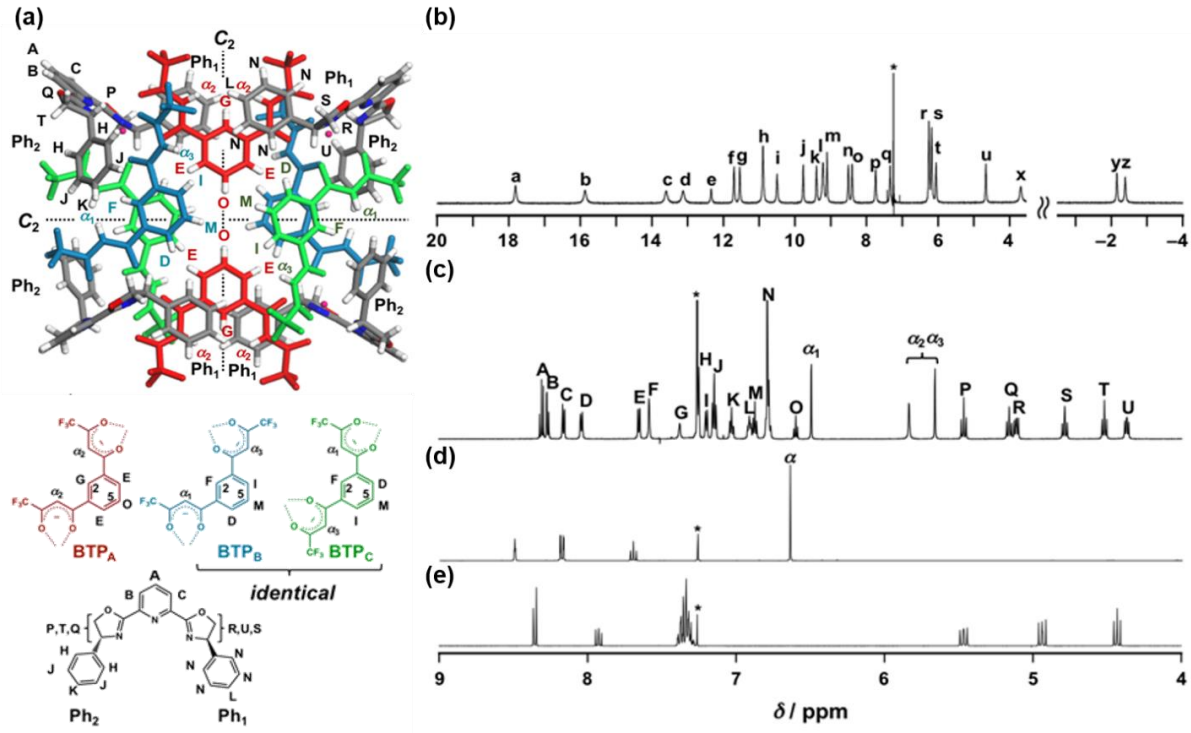

Figure 2.8. (a) Solution structure and NMR signal assignment of **1-Y^{Ph}*RRRR***. ^{1}H NMR (600 MHz) spectra of (b) **1-Eu^{Ph}*RRRR*** and (c) **1-Y^{Ph}*RRRR*** in $CDCl_3$. ^{1}H NMR (400 MHz) spectra of (d) BTP and (e) (*R*)-Ph-Pybox in $CDCl_3$. Asterisk denotes the solvent NMR peak.

Figure 2.8b shows the ^{1}H NMR spectrum of **1-Eu^{Ph}*RRRR*** in chloroform-d ($CDCl_3$). Due to the paramagnetic properties of Eu^{III} core, the 24 proton resonances of **1-Eu^{Ph}*RRRR*** are broad and spread over a wide chemical shift range of –3 to 18 ppm. To facilitate the rationalization, a chiral self-assembly of diamagnetic yttrium(III) ions (Y^{III}), which exhibit similar coordination modes to Eu^{III} ions was synthesized. The Y^{III} circular helicate of [(*R*)-Ph-Pybox]$_4$(Y^{III})$_4$(BTP)$_6$, **1-Y^{Ph}*RRRR*** was successfully crystallized and confirmed by the X-ray diffraction analysis (Figure *A5*). X-ray crystallographic of **1-Y^{Ph}*RRRR*** revealed the chiral self-assembly of Y^{III} is isomorphous of the **1-Eu^{Ph}*RRRR***. The ^{1}H NMR spectrum of **1-Y^{Ph}*RRRR*** also exhibits a total of 24 resonances (Figure2.8c). Full assignment of 24 proton NMR signals of **1-Y^{Ph}*RRRR*** and **1-Eu^{Ph}*RRRR*** were done sequentially with the aid of the COSY and

ROESY correlations (Figure *A15-A17*, for a detailed discussion, see the Appendices), and ^{1}H NMR signals of free BTP, (*R*)-Ph-Pybox ligands and (Figure 2.8d and e, respectively). The ^{1}H NMR spectrum of **1-Y^{Ph}*RRRR*** suggests D_2 symmetry in the self-assemblies in solution, showing consistency with the D_2-symmetrical crystal structure. Three proton singlets are found with an integration ratio of 1:1:1 in the region for the α-proton (5-7 ppm), (α_{1-3} in Figure 2.8c). One of three singlets correspond to the α-protons of BTP_A with C_2 symmetry, and the other two singlets are assignable to the α-protons of BTP_B and BTP_C without C_2-symmetry (Figure 2.8a).

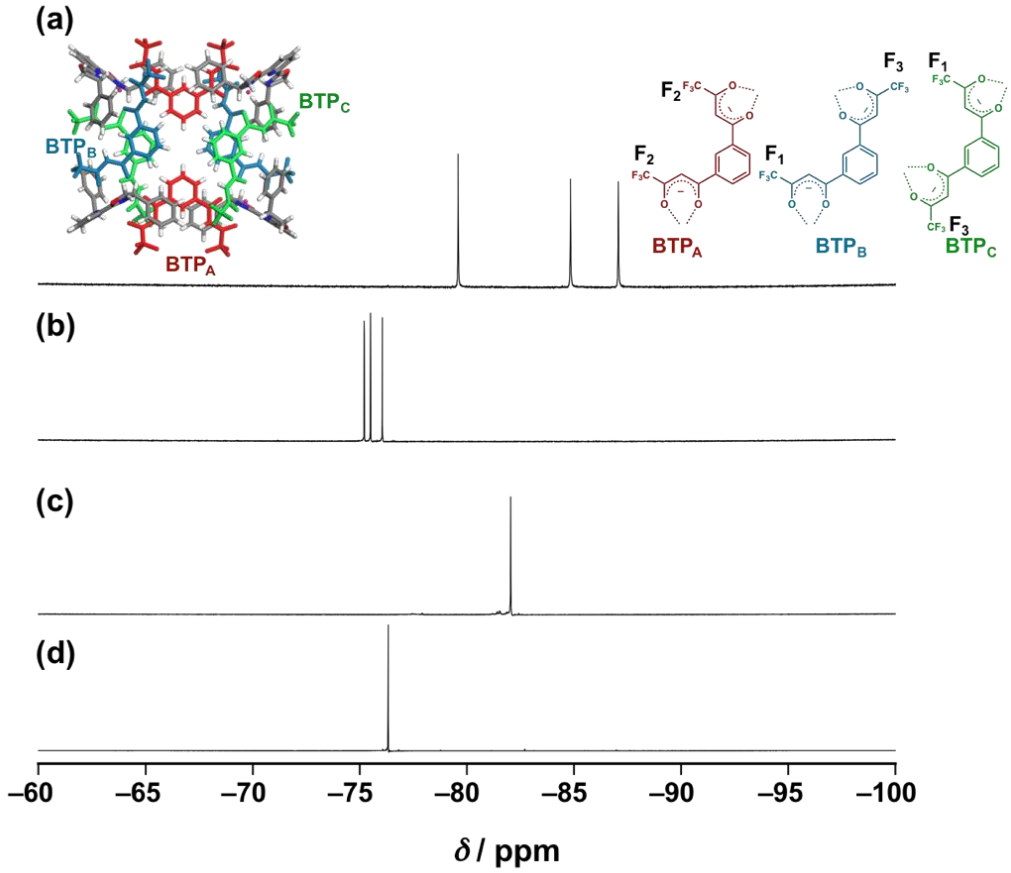

Figure 2.9. ^{19}F NMR spectra of (a) **1-Eu^{Ph}*RRRR*** (b) **1-Y^{Ph}*RRRR*** (c) H_2(BTP) ligand in $CDCl_3$. (d) ^{19}FNMR spectrum of precursor complex [Eu^{III}_2(BTP)$_3$] in acetone-d_6.

Three ^{19}F NMR signals due to BTP ligands can be observed for the self-assembly, also indicating the **1-Y^{Ph}*RRRR*** and **1-Eu^{Ph}*RRRR*** exhibit D_2 symmetry in solution. Figure 2.9a and b show the ^{19}F NMR spectrum of **1-Eu^{Ph}*RRRR*** and **1-Y^{Ph}*RRRR***, respectively. In addition, no (*R*)-Ph-second diastereomer was detected in both ^{1}H NMR spectra, indicating a single homochiral conformation in solution.

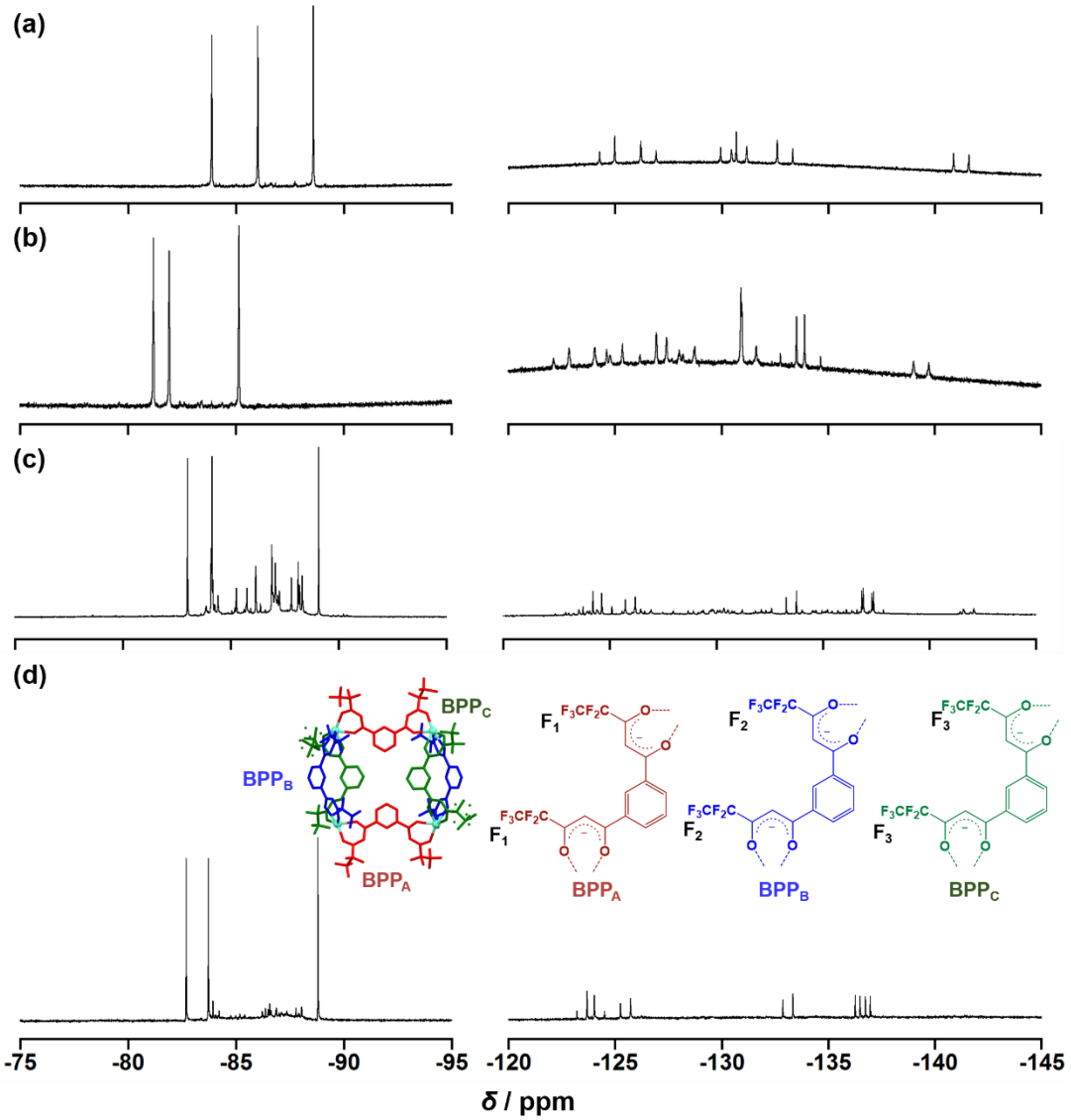

Figure 2.10. ^{19}F NMR spectra of (a) **2-Eu^{Ph}*RRRR*** (b) **3-Eu^{Ph}*RRRR*** (c) **2-Eu^{iPr}*RRRR*** in $CDCl_3$. ^{19}F NMR spectrum of **2-Eu^{iPr}*RRRR*** in toluene-d_8.

Analogous to **1-Eu^{Ph}*RRRR***, **2-Eu^{Ph}*RRRR*** and **3-Eu^{Ph}*RRRR*** are likely to exhibit D_2 symmetry in solution. The ^{19}F NMR spectrum of **2-Eu^{Ph}*RRRR*** and **3-Eu^{Ph}*RRRR*** show three characteristic CF_3 fluorine peaks in $CDCl_3$ (Figure 2.10a and b) and toluene-d_8 (C_7D_8). Three fluorine resonances from CF_3 units are displayed in the ^{19}F NMR spectrum of **2-Eu^{iPr}*RRRR*** in C_7D_8, suggesting the pseudo-C_{2h} symmetrical self-assemblies in toluene (Figure 2.10d). Each type of BPP ligands (BPP_A/BPP_B/BPP_C) of **2-Eu^{iPr}*RRRR*** contribute one fluorine signals, where two fluoroalkyl ends in each BPP ligands become identical under C_2 and σ_h symmetry. Additional minor CF_3 fluorine peaks are detected in the ^{19}F NMR analysis of **2-Eu^{iPr}*RRRR*** in $CDCl_3$ (Figure 2.10c), indicating probable coexisting conformers in the polar solvent medium. Due to the chiral environment, individual geminal CF_2 fluorines are diastereotopic and chemical shifts are non-equivalent (in the spectrum region from -120 ppm to -145ppm). F_F couplings between the geminal CF_2 fluorine in each self-assembly were observed through the 2D ^{19}F,^{19}F COSY NMR analysis (Figure *A19-22*). Based on ^{19}F,^{19}F cross relation, each geminal CF_2 fluorine resonance seem to split into doublets due to its neighbouring fluorine atom.

2.5 Mass Analysis

Investigation of the supramolecular geometry of the self-assemblies in solution by Electrospray Ionization (ESI) was carried out. Mass signals of $\{[Pybox]_4(Ln^{III})_4L_6 + H\}^+$ or $\{[Pybox]_2(Ln^{III})_2L_3 + H\}^+$ peaks were detected in the ESI(+) method. In ESI(+)-MS of **1-Eu^{Ph}*RRRR*/1-Eu^{Ph}*SSSS***, mass peaks of 4201.4 and 4223.4 can be unambiguously assigned to $\{[Ph\text{-}Pybox]_4(Eu^{III})_4(BTP)_6 + H\}^+$ and $\{[Ph\text{-}Pybox]_4(Eu^{III})_4(BTP)_6 + Na\}^+$, respectively, by using their calculated isotopic distribution (Figure 2.11b inset). In addition, mass peak assignable to the $Ln^{III}_2L_3$ type complex at *m*/*z* = 2101.20, which corresponds to $\{[Ph\text{-}Pybox]_2(Eu^{III})_2(BTP)_3 + H\}^+$ was also detected. Mass signals of $Ln^{III}_2L_3$ and $Ln^{III}_4L_6$ type complex of **2-Eu^{Ph}*RRRR*/2-Eu^{Ph}*SSSS***, **2-Eu^{iPr}*RRRR*/2-Eu^{iPr}*SSSS*** and **3-Eu^{Ph}*RRRR*/3-Eu^{Ph}*SSSS*** are shown in Figure 2.12, with their theoretical isotopic distribution.

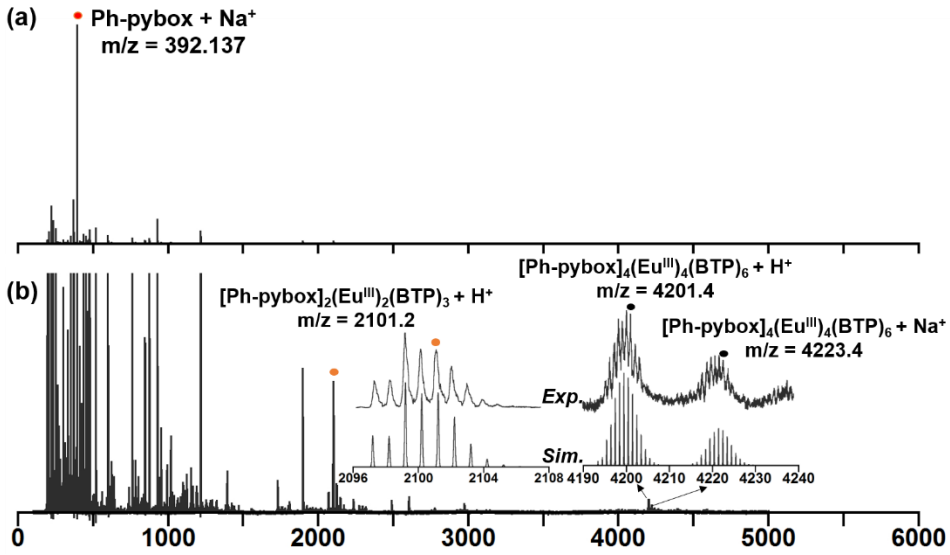

Figure 2.11. (a) ESI(+)-MS of **1-Eu^{Ph}*SSSS*** in chloroform with the flow of methanol. (b) ESI(+)-MS of **1-Eu^{Ph}*SSSS*** with the intensity scaled down. Inset: Isotopically resolved signals at *m*/*z* = 2102.2, *m*/*z* = 4201.4 and *m*/*z* = 4223.4 with the calculated isotopic distributions for$\{[(S)\text{-Ph-pybox})]_2Eu_2(BTP)_3 + H\}^+$, $\{[(S)\text{-Ph-pybox})]_4Eu_4(BTP)_6 + H\}^+$ and $\{[(S)\text{-Ph-pybox})]_4Eu_4(BTP)_6 + Na\}^+$ respectively.

$Eu^{III}_2L_3$ type complex can be interpreted as possible thermodynamic equilibria existing in solution at low concentration and possible gas-phase dissociation processes. Thus, the simple

$[Eu^{III}_2L_3]$ dinuclear helicate should be considered as the most probable species in solution, as a C_2 point group of $[Pybox]_2Eu^{III}_2L_3$ is in agreements with 3 fluorine signals identified by ^{19}F-NMR. Hence, the photophysical characterization of self-assemblies were investigated in solution phase and solid-state to evaluate consistency of solution and solid-state structure.

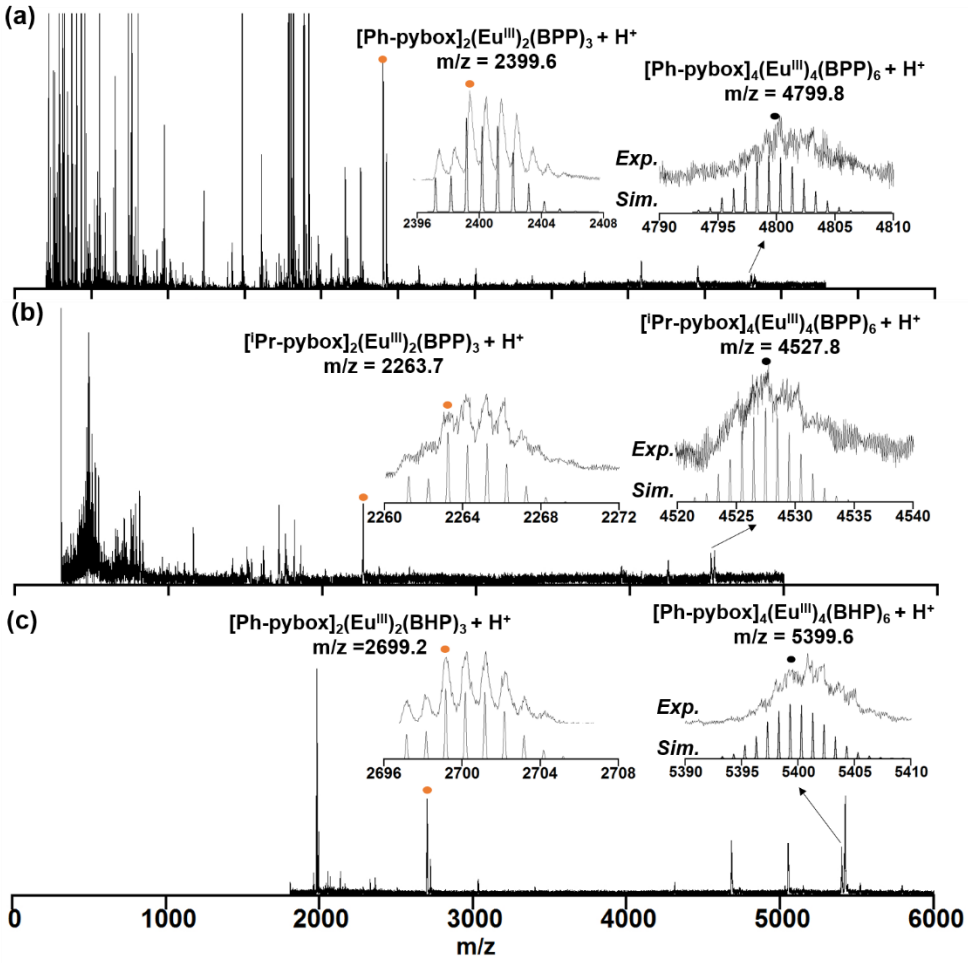

Figure 2.12. (a) ESI(+)-MS of **2-Eu^{Ph}*RRRR*** with the intensity scaled down. Inset: Isotopically resolved signals at *m*/*z* = 2399.6 and *m*/*z* = 4799.8 with the calculated isotopic distributions for$\{[(R)$-Ph-pybox$)]_2Eu_2(BPP)_3 + H\}^+$ and $\{[(R)$-Ph-pybox$)]_4Eu_4(BTP)_6 + H\}^+$ respectively. (b) ESI(+)-MS of **2-Eu^{iPr}*RRRR*** with the intensity scaled down. Inset: Isotopically resolved signals at *m*/*z* = 2263.7 and *m*/*z* = 4527.8 with the calculated isotopic distributions for$\{[(R)$-^{i}Pr-pybox$)]_2Eu_2(BPP)_3 + H\}^+$ and $\{[(R)$-^{i}Pr-pybox$)]_4Eu_4(BTP)_6 + H\}^+$ respectively. (c) ESI(+)-MS of **3-Eu^{Ph}*SSSS*** with the intensity scaled down. Inset: Isotopically resolved signals at *m*/*z* = 2699.2 and *m*/*z* = 5399.6 with the calculated isotopic distributions for$\{[(S)$-Ph-pybox$)]_2Eu_2(BHP)_3 + H\}^+$ and $\{[(S)$-Ph-pybox$)]_4Eu_4(BHP)_6 + H\}^+$ respectively.

2.6 Emission and CPL Profile

Upon excitation at 360nm, the Sm^{III}, Tb^{III}, and Eu^{III} self-assemblies gives characteristics red-orange ($^4D_{5/2}\rightarrow{}^6F_J$, J = 5/2-11/2), green ($^5D_4\rightarrow{}^7F_J$, J = 6-3) and red ($^5D_0\rightarrow{}^7F_J$, J = 0-4) luminescence, respectively in solution (chloroform or toluene) and solid-state (KBr pellet). Nearly quantitative fit between the crystal-field splitting of emission in solution and solid state are observed for all the Eu^{III} self-assemblies. The CPL profiles of (*R*)- and (*S*)-isomers display almost complete mirror signals with each other (Figure 2.13 and 2.14) and the CPL spectra in solution are nearly identical to the solid-state spectra.

For the Eu^{III} self-assemblies, $^5D_0 \rightarrow {}^7F_0$ emission band displays one narrow line, whereas $^5D_0 \rightarrow {}^7F_1$ and $^5D_0 \rightarrow {}^7F_2$ emission bands split into several crystal-field level. Intense peak is always observed at hypersensitive $^5D_0 \rightarrow {}^7F_2$ transition with respect to the $^5D_0 \rightarrow {}^7F_1$ transition, indicating non-centrosymmetric nature of the nona-coordinated Eu^{III} geometries. The degree of Eu^{III} site symmetry can be assessed through the relative total intensity ratio of the $^5D_0 \rightarrow {}^7F_2$ transition to $^5D_0 \rightarrow {}^7F_1$ transition, A_{rel}(TI)[61-62]. Taking into 5% measurement error, all the $(Pybox)_4(Eu^{III})_4L_6$ self-assemblies have a similar A_{rel}(TI) value of about 14 (Table 2.2). Besides, the A_{rel}(TI) values in solution and solid state are comparable, suggesting a similar distorted capped SAP Eu^{III} geometries in solution.

Table 2.2. Relative Total Intensity Ratio of Eu^{III} self-assemblies in chloroform, toluene and KBr pellet.

Eu^{III} self-assemblies	**Relative Total Intensity Ratio, A_{rel}(TI)**		
	$CHCl_3$	**C_7H_8**	**KBr**
1-Eu^{Ph}*RRRR* (1-Eu^{Ph}*SSSS*)	14.62 (14.82)	14.72 (14.69)	13.02 (13.05)
2-Eu^{Ph}*RRRR* (2-Eu^{Ph}*SSSS*)	14.60 (14.94)	14.72 (14.66)	14.05 (14.23)
2-Eu^{iPr}*RRRR* (2-Eu^{iPr}*SSSS*)	14.49 (14.54)	14.60 (14.41)	13.82 (14.00)
3-Eu^{Ph}*RRRR* (3-Eu^{Ph}*SSSS*)	14.37 (14.93)	14.85 (14.81)	14.42 (14.24)

* Estimated measurement error for A_{rel}(TI) = 5%.

The transition of interest for CPL activity of Sm^{III}, Tb^{III}, Eu^{III} are $^4G_{5/2}\rightarrow{}^6H_{7/2}$ (ca. 596nm), $^5D_4\rightarrow{}^7F_5$ (ca. 542nm) and $^5D_0\rightarrow{}^7F_1$ (ca. 591 nm) respectively, as these transitions often show large circular polarization as they are magnetic dipole transitions satisfying the magnetic-dipole selection rule, $\Delta J = 0, \pm 1$ (refer to Figure 2.13 for emission and CPL spectra). The g_{lum} of the **1-Eu^{Ph}*RRRR*** and **1-Eu^{Ph}*SSSS*** were determined to be +0.22 and –0.24 respectively, at the magnetic transition ($^5D_0\rightarrow{}^7F_1$) band at λ = 591 nm in chloroform. **1-Eu^{Ph}*RRRR*/1-Eu^{Ph}*SSSS*** exhibit higher g_{lum} compared to the other Sm^{III} and Tb^{III} counterpart. **1-Sm^{Ph}*RRRR*/1-Sm^{Ph}*SSSS*** exhibit g_{lum} of -0.11/+0.12 at $^4G_{5/2}\rightarrow{}^6H_{7/2}$ transition in chloroform. Accurate determination of the g_{lum} of **1-Tb^{Ph}*RRRR*/1-Tb^{Ph}*SSSS*** could not be done due to its weak emission in chloroform.

Circular helicates of **2-Eu^{Ph}*RRRR*/2-Eu^{Ph}*SSSS*** and **3-Eu^{Ph}*RRRR*/3-Eu^{Ph}*SSSS*** display similar emission and CPL spectra signature, in which sign of the CPL of the (*R*)-isomer follows the sequence of (+) and (–) at $^5D_0 \rightarrow {}^7F_1$ and $^5D_0 \rightarrow {}^7F_2$ transitions, respectively (Figure 2.14a, b, d, e, g and h). Such spectral similarity indicates that the solution structure and primary coordination spheres of **3-Eu^{Ph}*RRRR*/3-Eu^{Ph}*SSSS*** must be very alike to **2-Eu^{Ph}*RRRR*/2-Eu^{Ph}*SSSS***. On the other hand, **2-Eu^{iPr}*RRRR*/2-Eu^{iPr}*SSSS*** exhibit different CPL spectral pattern (Figure 2.14b, e, and h). The CPL sign of the **2-Eu^{iPr}*RRRR*** follows the sequence of (–, +) at $^5D_0 \rightarrow {}^7F_1$ transition and (–, +, –) at $^5D_0 \rightarrow {}^7F_2$ transition. The specific bipolar CPL peaks observed at both $^5D_0 \rightarrow {}^7F_1$ and $^5D_0 \rightarrow {}^7F_2$ transitions are ascribed to the possible pseudo-racemization in the four Eu^{III} on each tetra-nuclear grid of **2-Eu^{iPr}*RRRR*/2-Eu^{iPr}*SSSS***. **2-Eu^{Ph}*RRRR*/2-Eu^{Ph}*SSSS*** and **3-Eu^{Ph}*RRRR*/3-Eu^{Ph}*SSSS*** exhibit the similar g_{lum} value (~|0.30| in $CHCl_3$), whereas **2-Eu^{iPr}*RRRR*/2-Eu^{iPr}*SSSS*** displays the lower g_{lum} (~|0.10| in $CHCl_3$). Different ligands orientations around the Eu^{III} and number of non-distinguishable Eu^{III} coordination geometry affects the sign and magnitude of the luminescence dissymmetry factors. This suggests significant contribution of dynamic coupling mechanism to the observed g_{lum}

value, in which the chiral arrangement of π-conjugation systems of the *β*-diketonate ligands seem to play dominant role.

By using a calibrated integrating sphere system upon excitation of the ligand absorption band, the emission quantum yield (ϕ_{em}) was determined (summarized in Table 2.3). The emission decay of the Eu^{III} self-assemblies was found to be mono-exponential in the solution, suggesting only one Eu^{III} species in the solution (Figure *A31* for emission decay profile of **1-Eu^{Ph}*RRRR*/1-Eu^{Ph}*SSSS***, **2-Eu^{Ph}*RRRR*/2-Eu^{Ph}*SSSS*, 2-Eu^{iPr}*RRRR*/2-Eu^{iPr}*SSSS*, 3-Eu^{Ph}*RRRR*/3-Eu^{Ph}*SSSS***)

Table 2.3. Luminescence dissymmetry factor (g_{lum}), quantum yield (ϕ_{em}) and emission lifetime (τ) of Eu^{III} self-assemblies

Eu^{III} self-assemblies	**g_{lum} ($^5D_0 \rightarrow {}^7F_1$)**		**ϕ_{em} ($CHCl_3$)**	**τ/ms ($CHCl_3$)**
	$CHCl_3$	**C_7H_8**		
	(~592.5 nm)			
1-Eu^{Ph}*RRRR*	0.22	0.20	0.15	0.602
(1-Eu^{Ph}*SSSS*)	(-0.22)	(0.20)	(0.15)	(0.600)
2-Eu^{Ph}*RRRR*	0.31	0.29	0.21	0.607
(2-Eu^{Ph}*SSSS*)	(-0.30)	(-0.29)	(0.20)	(0.602)
2-Eu^{iPr}*RRRR*	0.07	0.12	0.16	0.624
(2-Eu^{iPr}*SSSS*)	(-0.08)	(-0.11)	(0.16)	(0.625)
3-Eu^{Ph}*RRRR*	0.31	0.28	0.19	0.601
(3-Eu^{Ph}*SSSS*)	(-0.30)	(-0.28)	(0.19)	(0.615)

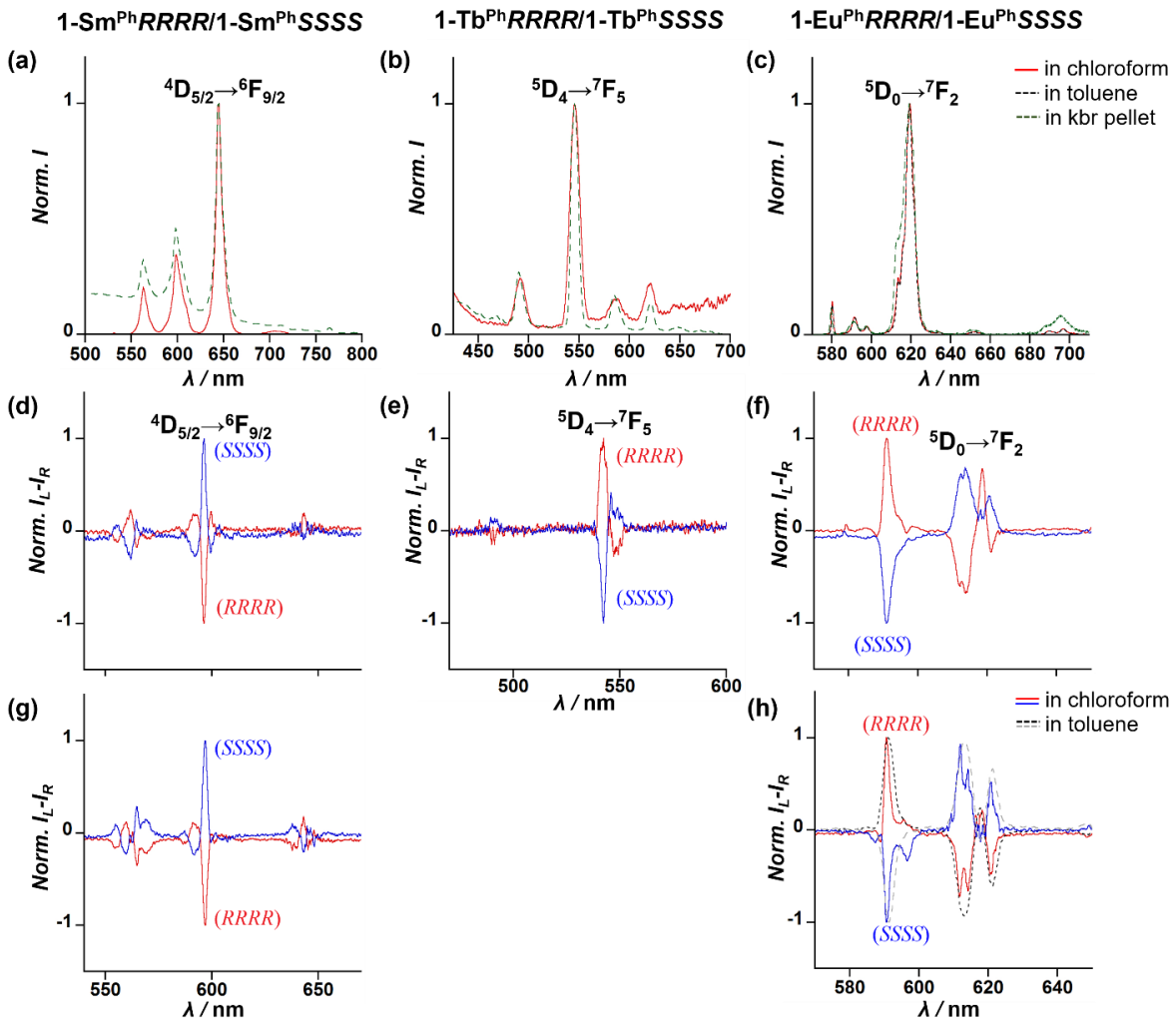

Figure 2.13. Emission spectra of (a) **1-Sm^{Ph}*RRRR***, (b) **1-Tb^{Ph}*RRRR***, (c) **1-Eu^{Ph}*RRRR*** in chloroform (red solid, conc. = 3.4 × 10^{-6} M), toluene (black dashed, conc. = 3.4 × 10^{-6} M) and kbr pellet (green dashed) at 298K. Normalized CPL spectra of (d) **1-Sm^{Ph}*RRRR*/1-Sm^{Ph}*SSSS***, (e) **1-Tb^{Ph}*RRRR*/1-Tb^{Ph}*SSSS***, and (f) **1-Eu^{Ph}*RRRR*/1-Eu^{Ph}*SSSS*** in KBr pellet (red and blue solid line for the (*R*)- and (*S*)-enantiomers in chloroform, respectively). Normalized CPL spectra of (g) **1-Sm^{Ph}*RRRR*/1-Sm^{Ph}*SSSS***, and (h) **1-Eu^{Ph}*RRRR*/1-Eu^{Ph}*SSSS*** in chloroform and toluene at 298K (conc. = 3.4 × 10^{-6} M; red solid and black dashed for the (*R*)-enantiomers in chloroform and toluene, respectively; blue and grey dashed line for the (*S*)- enantiomers in chloroform and toluene, respectively).

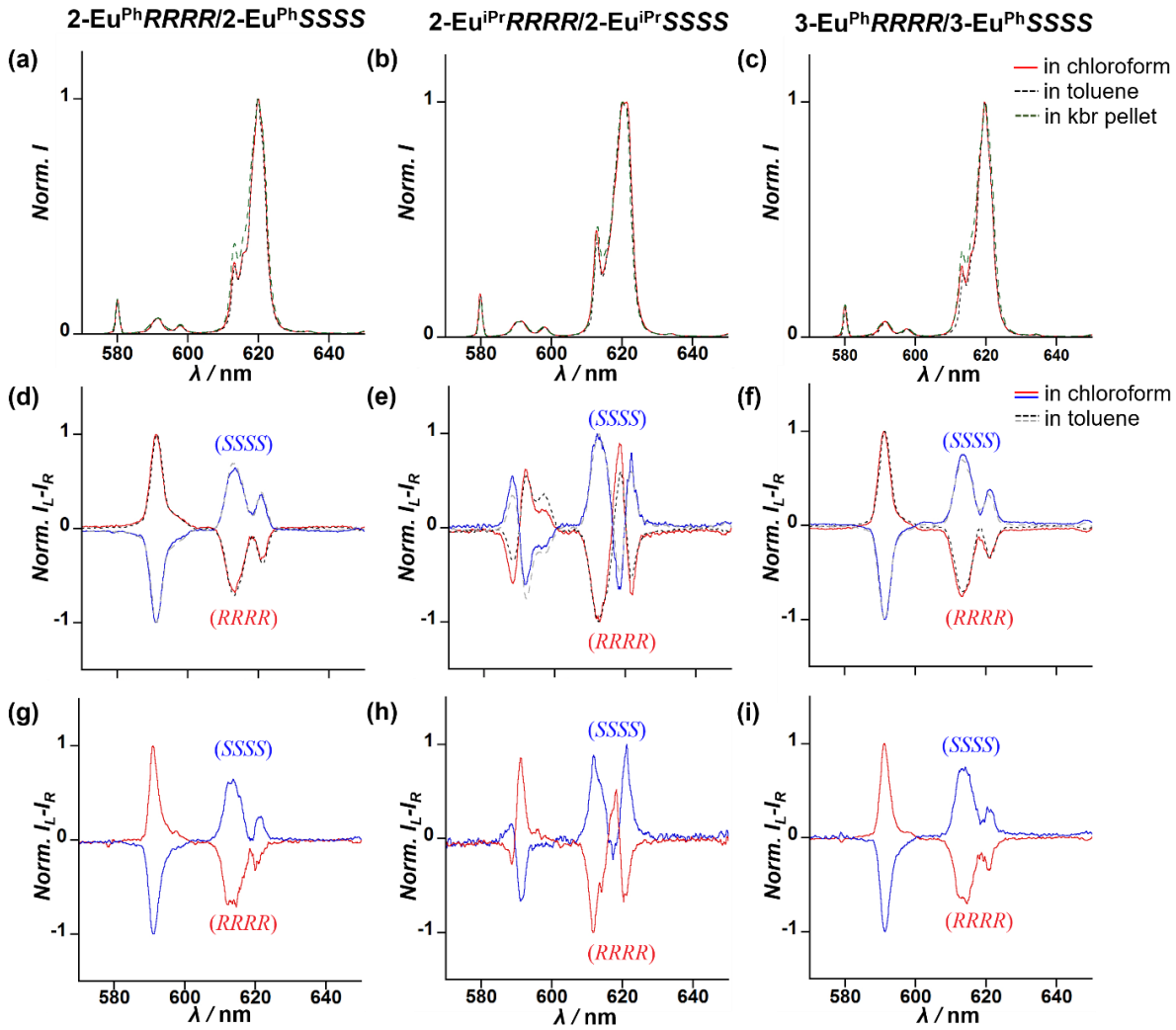

Figure 2.14. Emission spectra of (a) **2-Eu^{Ph}*RRRR***, (b) **2-Eu^{iPr}*RRRR***, and (c) **3-Eu^{Ph}*RRRR*** in chloroform (red solid, conc. = 3.4 × 10^{-6} M), toluene (black dashed, conc. = 3.4 × 10^{-6} M) and kbr pellet (green dashed) at 298K. Normalized CPL spectra of (d) **2-Eu^{Ph}*RRRR*/2-Eu^{Ph}*SSSS***, (e) **2-Eu^{iPr}*RRRR*/2-Eu^{iPr}*SSSS***, and (f) **3-Eu^{Ph}*RRRR*/3-Eu^{Ph}*SSSS*** in chloroform and toluene at 298K (conc. = 3.4 × 10^{-6} M; red solid and black dashed for the (*R*)-enantiomers in chloroform and toluene, respectively; blue and grey dashed line for the (*S*)- enantiomers in chloroform and toluene, respectively). Normalized CPL spectra of (g) **2-Eu^{Ph}*RRRR*/2-Eu^{Ph}*SSSS***, (h) **2-Eu^{iPr}*RRRR*/2-Eu^{iPr}*SSSS***, and (i) **3-Eu^{Ph}*RRRR*/3-Eu^{Ph}*SSSS*** in KBr pellet (red and blue solid line for the (*R*)- and (*S*)- enantiomers in chloroform, respectively).

3.0 CHIRAL SELF-ASSEMBLED OF $Ln^{III}_4L_6(Pybox)_4$ TETRAHEDRON

3.1 Introduction

In the previous chapter, a series of novel expanded tetranuclear Eu^{III} grid self-assemblies based on achiral anionic bis-*β*-diketonates, L ligands with larger GC ($[Eu^{III}_4L_6]$ = 10) were fabricated through sequential reaction of $[Eu^{III}_2L_3]$ with GC of 5 with chiral co-ligands (*R*)- or (*S*)-Pybox.

In this chapter, rational design of new chiral tetranuclear Ln^{III} self-assemblies with GC of 10 was demonstrated by controlling the length of the spacer in the bis-*β*-diketonates ligand (Figure 3.1). When employing bis-*β*-diketonates ligand with bipheyl spacer as bridging ligands, tetrahedron type of $[Eu^{III}_4L_6]$ self-assemblies with GC of 10 were isolated. However, increasing the linkage of Eu-Eu distances in these $[Eu^{III}_4L_6]$ tetrahedrons have increased their structural conformational flexibility in polar or non-polar solvent medium. All the $[Eu^{III}_4L_6]$ tetrahedron exhibit large circular polarization in solution with different chiroptical performance ($|g_{lum}|$ = 0.08 to 0.23).

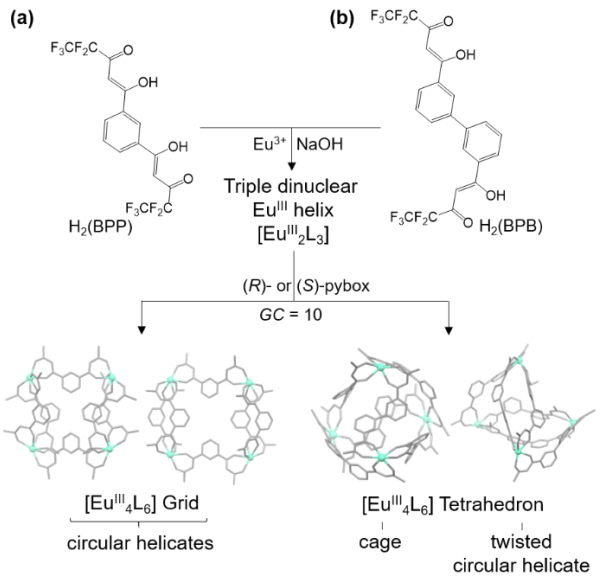

Figure 3.1. Reaction scheme of (a) $[Eu^{III}_4L_6]$ circular helicates and (b) $[Eu^{III}_4L_6]$ tetrahedral cage or circular helicate.

3.2 Preparation

Biphenyl spacer - bridging ligands of fluorinated bis-β-diketonate, H_2BPB can be synthesized from the Claisen Condensation between 3,3'-diacetylbiphenyl and two non-enolizable ethyl pentafluoropropionate (Figure 3.2).

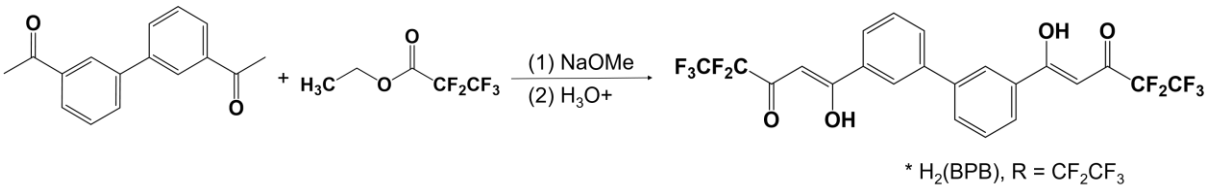

Figure 3.2. Reaction scheme of H_2(BPP), ligand

In basic condition, the deprotonated anionic BPB ligands can react with Eu^{III} chloride hexahydrate in 3:2 ratio to afford dinuclear $[Eu^{III}_2(BPB)_3]$ complexes (Figure 3.3). The $[Eu^{III}_2(BPB)_3]$ helicate contains solvent molecules weakly bound to each Eu^{III} ions. Although attempt to grow crystal of $Eu^{III}_2(BPB)_3$ from solvent pairs of DME/hexane or ethanol/chloroform/hexane was unsuccessful, similar $[Eu^{III}_2(BTB)_3]$ helix structure was confirmed and reported in the literature[52].

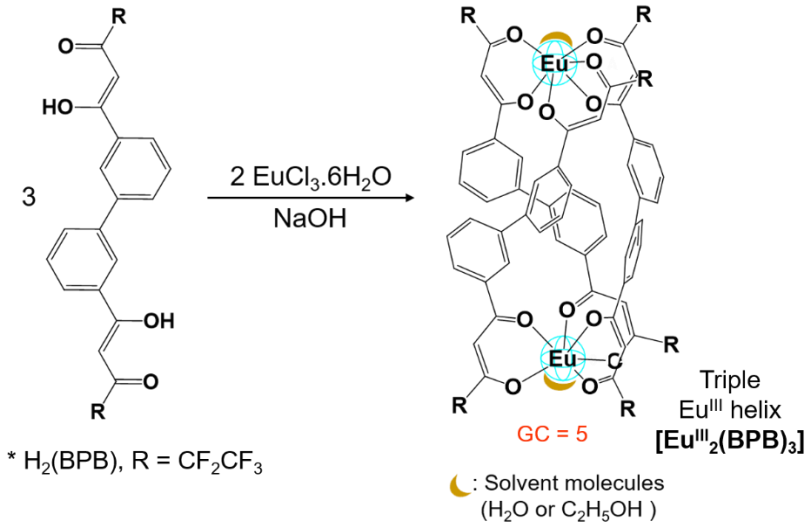

Figure 3.3. Reaction scheme of $[Eu^{III}_2L_3]$, L= BPB.

Further reaction of the $[Eu^{III}_2(BPB)_3]$ with the (*R)* or (*S)*-pybox ligand produce chiral D_2-symmetrical tetrahedral Eu^{III} structures, [(*R*)- or (*S*)-Ph-Pybox]$_4Eu^{III}_4(BPB)_6$ (**4-Eu^{Ph}*RRRR*/4-Eu^{Ph}*SSSS***) and [(*R*)- or (*S*)-^{i}Pr-Pybox]$_4Eu^{III}_4(BPB)_6$ (**4-Eu^{iPr}*RRRR*** or **4-Eu^{iPr}*SSSS***) (Figure 3.4). Crystals of **4-Eu^{Ph}*RRRR*/4-Eu^{Ph}*SSSS*** and **4-Eu^{iPr}*RRRR*** or **4-Eu^{iPr}*SSSS*** can be grown from toluene/hexane solvent pairs.

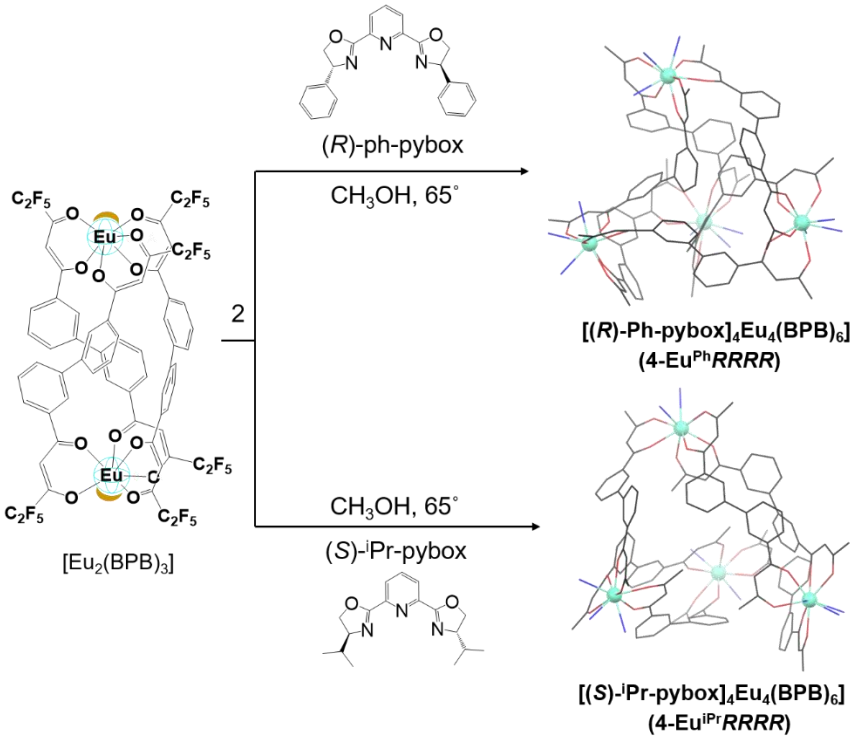

Figure 3.4. Reaction Scheme of **4-Eu^{Ph}*RRRR*, 4-Eu^{iPr}*SSSS***

3.3 Crystal structure

Figure 3.5a shows the crystal structures of **4-Eu^{Ph}*RRRR*/4-Eu^{Ph}*SSSS***, where the *R*- and *S*-isomers are non-superimposable complete mirror images of each other (refer to Table *A8* for crystallographic data). **4-Eu^{Ph}*RRRR*** is crystallized in monoclinic with space group of *C*2 whereas **4-Eu^{Ph}*SSSS*** is crystallized in orthorhombic crystal system with space group of $P2_12_12$. Although attempts to grow good single crystals of **4-Eu^{iPr}*RRRR*/4-Eu^{iPr}*SSSS*** failed, poor resolved structure of **4-Eu^{iPr}*SSSS*** revealed tetrahedral tetranuclear Eu^{III} tetrahedron as shown in Figure 3.5b.

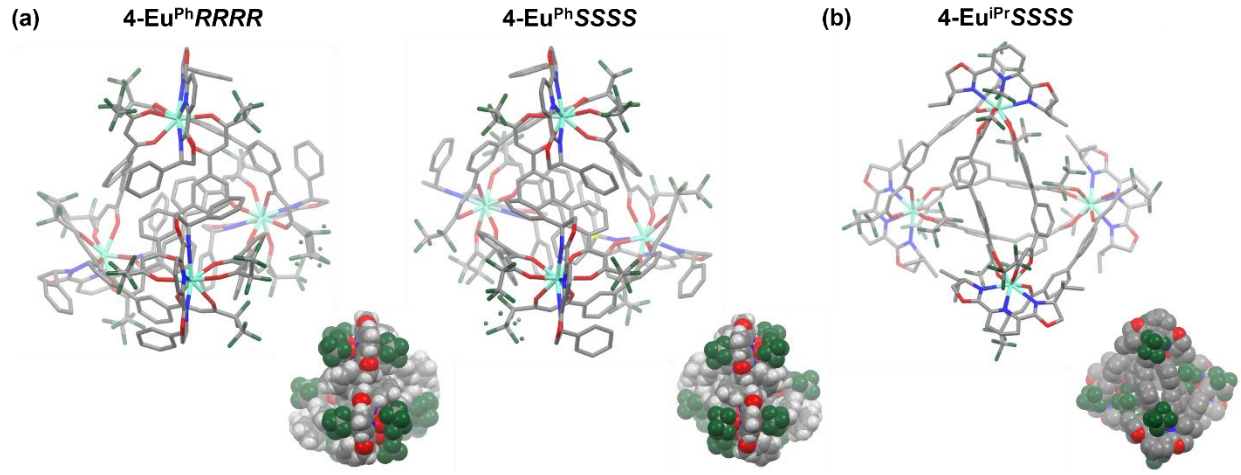

Figure 3.5. X-ray crystal structure of (a) **4-Eu^{Ph}*RRRR*** and **4-Eu^{Ph}*SSSS*** and poor resolved crystal structure (b) **4-Eu^{iPr}*SSSS***.

Structure of **4-Eu^{Ph}*RRRR*/4-Eu^{Ph}*SSSS*** and **4-Eu^{iPr}*RRRR*/4-Eu^{iPr}*SSSS*** can be considered as D_2-symmetrical tetrahedral tetranuclear cage and twisted circular helicate, respectively, composing two asymmetric units of [(*R*)- or (*S*)-Pybox]$_2$Eu$^{III}_2$(BPB)$_3$. Four nona-coordinated Eu^{III} ions with same chirality define the vertices of the tetrahedral cluster, connecting to each other by six BPB bridging ligands. It should be noted that perfect D_2-symmetry is not observed in their crystal structures, probably due to crystal packing effects.

Therefore, slight variations in the Eu-Eu distances, Eu-Eu-Eu angles and dihedral angle of BPB ligand are observed in each crystal structures.

Presence of a $C_{2(y)}$ rotational symmetry in each crystal structures leads to a pair of two equivalent Eu^{III} ions (Eu_1 and Eu_2). The Eu_1-Eu_1 and Eu_2-Eu_2 distances in **4-Eu^{Ph}*RRRR*** are 11.364 Å and 11.760 Å, respectively. There are two similar pairs of three Eu-Eu-Eu interior angles in **4-Eu^{Ph}*RRRR*** (~ 59.0°, 66.5°, and 54.0°), making up four acute scalene triangular Eu-Eu-Eu planes (Figure 3.6a).

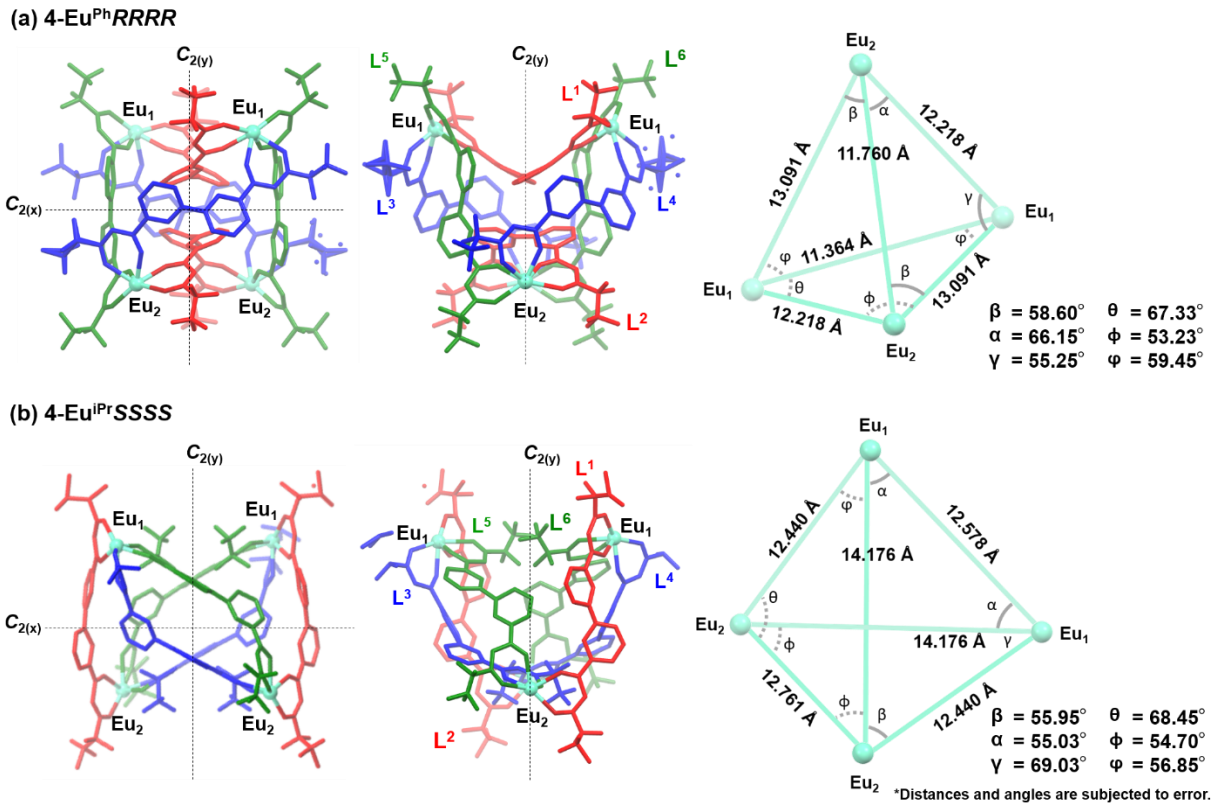

Figure 3.6. $Eu^{III}_4(BPB)_6$ core structure, Eu-Eu distances and Eu-Eu-Eu angles of (a) **4-Eu^{Ph}*RRRR***, (b) **4-Eu^{iPr}*SSSS***.

Each BPB coordinates to two Eu^{III} ions as a helicate ligand. Three BPB ligands connect each Eu^{III} ions to the other three Eu^{III} ions in **4-Eu^{Ph}*RRRR*/4-Eu^{Ph}*SSSS***, but to the other two Eu^{III} ions in **4-Eu^{iPr}*RRRR*/4-Eu^{iPr}*SSSS***. Taking into symmetry consideration, six BPB can be categorized into three type, BPB_A (L^1, L^2; red), BPB_B (L^3, L^4; blue) and BPB_C (L^5, L^6; green).

BPB_B and BPB_C are similar in **4-Eu^{Ph}*RRRR*/4-Eu^{Ph}*SSSS*** but dissimilar in **4-Eu^{iPr}*RRRR*/4-Eu^{iPr}*SSSS***. The uniformity of the BPB_B and BPB_C in each structure is clearly shown in their ligand twisting angle. The dihedral angle of BPB_B and BPB_C in **4-Eu^{Ph}*SSSS*** differ by ~53˚, but varies only by ~5˚ in **4-Eu^{iPr}*SSSS***. All the BPB ligands (BPB_A, BPB_B, and BPB_C) are *M*- and *P*-helix in **4-Eu^{Ph}*RRRR*** and **4-Eu^{Ph}*SSSS*** respectively. In **4-Eu^{iPr}*SSSS***, BPB_A (*P*-helix) is found to possess difference helicity with BPB_B and BPB_C (*M*-helix). The chiral BPB ligands twisting angle are summarized in Table 3.1.

Table 3.1. Dihedral angle of BPB ligands in the X-ray crystal structures of **4-Eu^{Ph}*RRRR*/4-Eu^{Ph}*SSSS*** and **4-Eu^{iPr}*SSSS***.

Eu(III) self-assemblies	Degree of BPB ligand twisting (˚)					
	BPB_A		BPB_B		BPB_C	
	L^1	L^2	L^3	L^4	L^5	L^6
4-Eu^{Ph}*RRRR*	-155.11	-155.16	154.12	154.12	100.65	100.65
4-Eu^{Ph}*SSSS*	153.75	153.75	-158.18	-149.14	-102.32	-102.32
4-Eu^{iPr}*SSSS	-118.25	-118.25	109.72	109.72	104.93	104.93

***** dihedral angles are subjected to error.

Difference type of ligand-to-ligand interactions between Pybox and *β*-diketonate moieties revealed in the crystal structures are found to be responsible for distinct BPB ligands coordination modes between **4-Eu^{Ph}*RRRR*/4-Eu^{Ph}*SSSS*** and **4-Eu^{iPr}*RRRR*/4-Eu^{iPr}*SSSS***. There is π-π stacking interaction between the phenyl arm (Ph^1) of Ph-Pybox and the *β*-diketonates moiety of the adjacent BPB ligand around Eu^{III} ions in **4-Eu^{Ph}*RRRR*/4-Eu^{Ph}*SSSS*** (Figure 3.7a; $d_{\pi\text{-}\pi}(Eu_1)$ = 3.883 Å and $d_{\pi\text{-}\pi}(Eu_2)$ = 3.940 Å). Possible CH_π interactions between the isopropyl arm ($^iPr^1$ and $^iPr^2$) of ^{i}Pr-pybox ligand and *β*-diketonates moieties of the adjacent BPB ligands around Eu_1 could be found in **4-Eu^{iPr}*RRRR*/4-Eu^{iPr}*SSSS*** (Figure 3.7b). In addition, intramolecular CF_F interactions between BPB ligands and CH_H

interactions between Ph-pybox ligands are found in the crystal structures of **4-Eu^{Ph}*RRRR*/4-Eu^{Ph}*SSSS***. Detailed contacting interactions are summarized in Table *A16*.

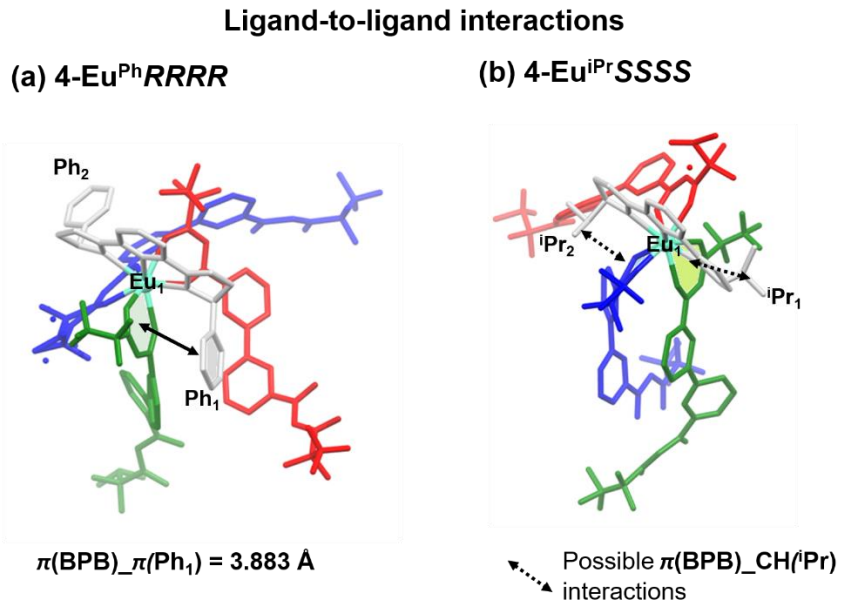

Figure 3.7. Ligand-to-ligand interactions of (a) **4-Eu^{Ph}*RRRR*** and (b) **4-Eu^{iPr}*RRRR***.

All the Eu^{III} cores are nona-coordinated with three nitrogen atoms of the Pybox ligand and six oxygen atoms of three *β*-diketonates moieties of L, exhibiting distorted capped SAP geometry (Figure 3.8, Figure *A10*, and Table *A14*). Primary coordination spheres are distorted from an ideal axial C_4 symmetry capped square antiprism geometry to a different extent (for instance, slight deviation in the dihedral angle along the diagonal edge of the square base from an ideal angle of 180˚ is observed in both *R*- and *S*-isomers). Eu^{III} coordination geometries in both **4-Eu^{Ph}*RRRR*/4-Eu^{Ph}*SSSS*** and **4-Eu^{iPr}*RRRR*/4-Eu^{iPr}*SSSS*** having Pybox ligand lies parallelly with the main C_4-axis. Besides, there is no difference found in the *β*-diketonates orientations in each of the four Eu^{III} cores of **4-Eu^{Ph}*RRRR*/4-Eu^{Ph}*SSSS*** and **4-Eu^{iPr}*RRRR*/4-Eu^{iPr}*SSSS***. Thus, four Eu^{III} coordination geometries are non-distinguishable in term of the outer-sphere ligand orientations. Interestingly, the outer-sphere ligand orientations in Eu^{III} cores of **4-Eu^{Ph}*RRRR*** are similar to **4-Eu^{iPr}*SSSS***, and vice versa.

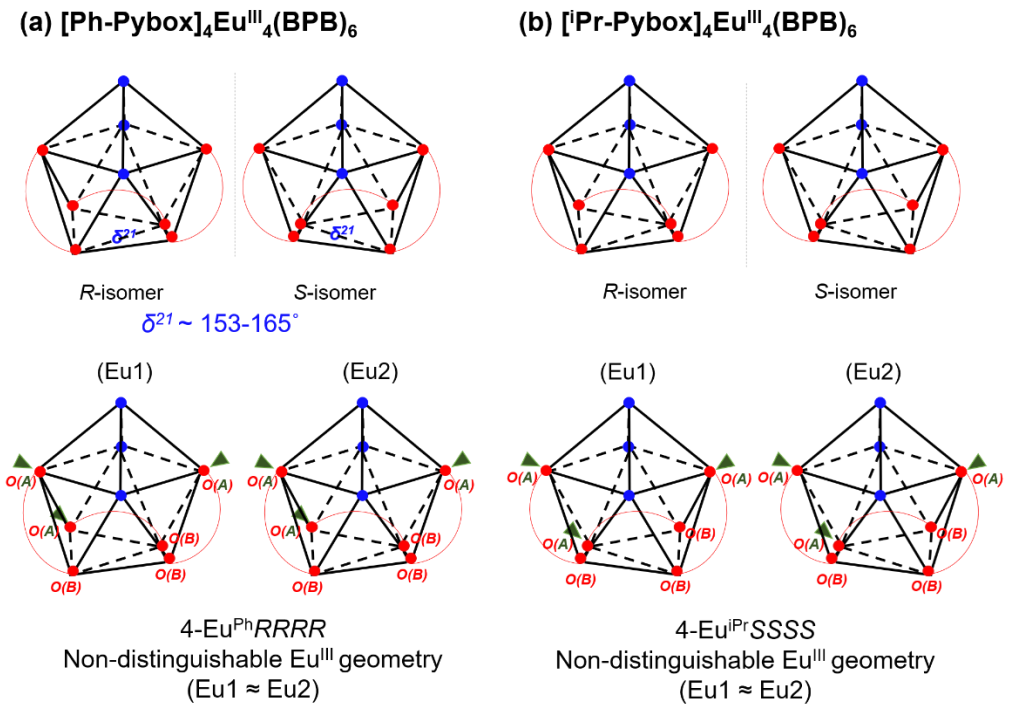

Figure 3.8. Coordination geometry of (a) **4-Eu^{Ph}*RRRR*/4-Eu^{Ph}*SSSS*** and (b) **4-Eu^{iPr}*RRRR*/4-Eu^{iPr}*SSSS***. O(A) and O(B) are oxygen atoms in the carbonyl units of bis-*β*-diketonate ligands which are next to the fluoroalkyl chains and phenyl rings, respectively. Green triangles in the Eu geometries designate linkage of the fluoroalkyl chain.

3.4 NMR Analysis

The ^{19}F NMR spectra of **4-Eu^{Ph}*RRRR*** and **4-Eu^{iPr}*RRRR*** in $CDCl_3$ and C_7D_8 are shown in Figure 3.9. The ^{19}F NMR spectra of **4-Eu^{Ph}*RRRR*** in both $CDCl_3$ and C_7D_8 show multiple CF_3 fluorine resonances, indicating deviation from a simple D_2 symmetrical **4-Eu^{Ph}*RRRR*** structure in solution (Figure 3.9a and b). **4-Eu^{Ph}*RRRR*** seem to be unstable in solution and most likely undergo structural change in polar and non-polar solvent medium. The ^{19}F NMR spectrum of **4-Eu^{iPr}*RRRR*** show multiple fluorine resonances of CF_3 units in $CDCl_3$ (Figure 3.9c), but displaying three CF_3 group fluorine resonances of in C_7D_8 (Figure 3.9d). **4-Eu^{iPr}*RRRR*** are highly symmetry in non-polar solvent, which are likely to exhibit D_2 symmetry in solution.

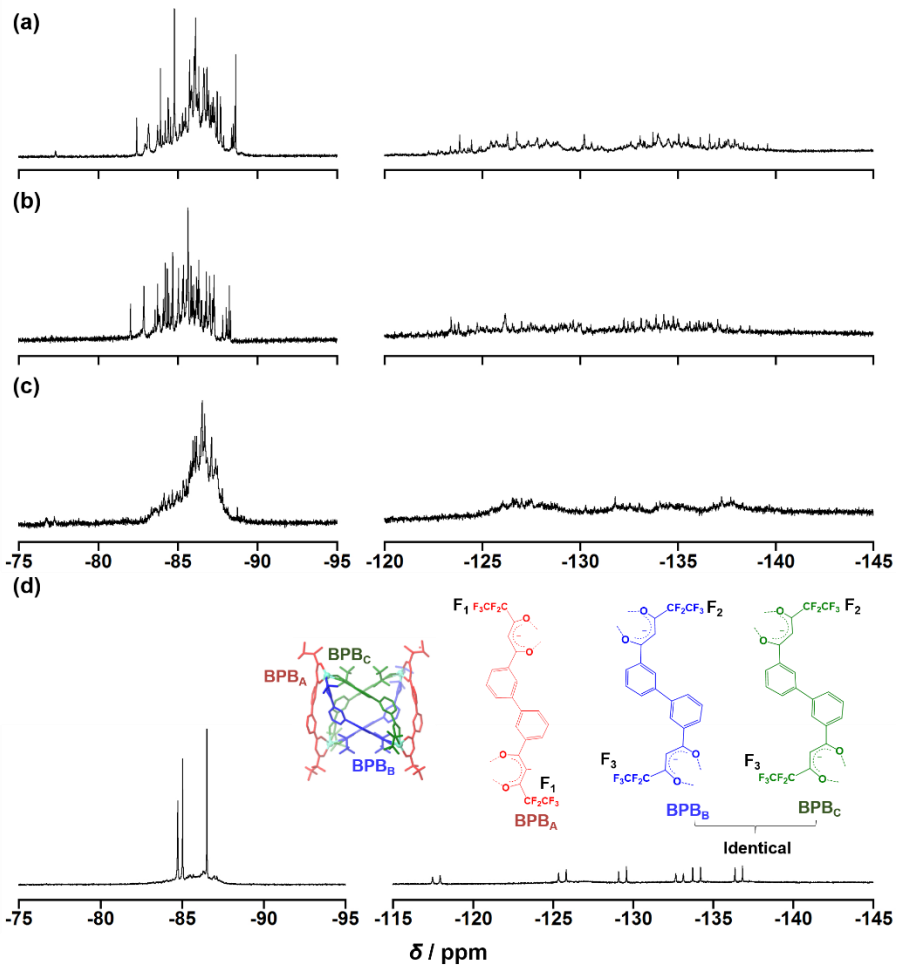

Figure 3.9. ^{19}F-NMR spectrum of **4-Eu^{Ph}*RRRR*** in (a) $CDCl_3$ (b) C_7D_8. ^{19}F-NMR spectrum of **4-Eu^{iPr}*RRRR*** in (c) $CDCl_3$ (d) C_7D_8.

3.5 Mass Analysis

ESI(+) mass spectrum of **4-Eu^{Ph}*RRRR*/4-Eu^{Ph}*SSSS*** exhibited a weak signal with mass distribution of 5278.307, corresponding to $\{[Ph\text{-}Pybox]_4(Eu^{III})_4(BPB)_6 + Na\}^+$ (Figure 3.10a-ii inset). Although the ESI(+) mass spectrometry of **4-Eu^{iPr}*RRRR*/4-Eu^{iPr}*SSSS*** do not detect the mass signals of $[iPr\text{-}Pybox]_4(Eu^{III})_4(BPB)_6$, exact molecular mass losing four ^{i}Pr-pybox ligands, $[(Eu^{III})_4(BPB)_6 + Na]^+$ with mass distribution m/z = 3778.146 was detected (Figure 3.10b-ii inset). Mass signal assignable to $Eu^{III}_2L_3$ type complex, $[(Eu^{III})_2(BPB)_3 + Na]^+$ at m/z = 1910.941 was also found in both mass spectrum of **4-Eu^{Ph}*RRRR*/4-Eu^{Ph}*SSSS*** and **4-Eu^{iPr}*RRRR*/4-Eu^{iPr}*SSSS*.** The detected signals give a mass pattern similar with the theoretical isotopic distribution pattern. $Eu^{III}_2L_3$ type complex can be interpreted as coexisting conformer in solution. Thus, the photophysical characterization of self-assemblies were investigated in solution phase and solid-state to evaluate consistency of solution and solid-state structure.

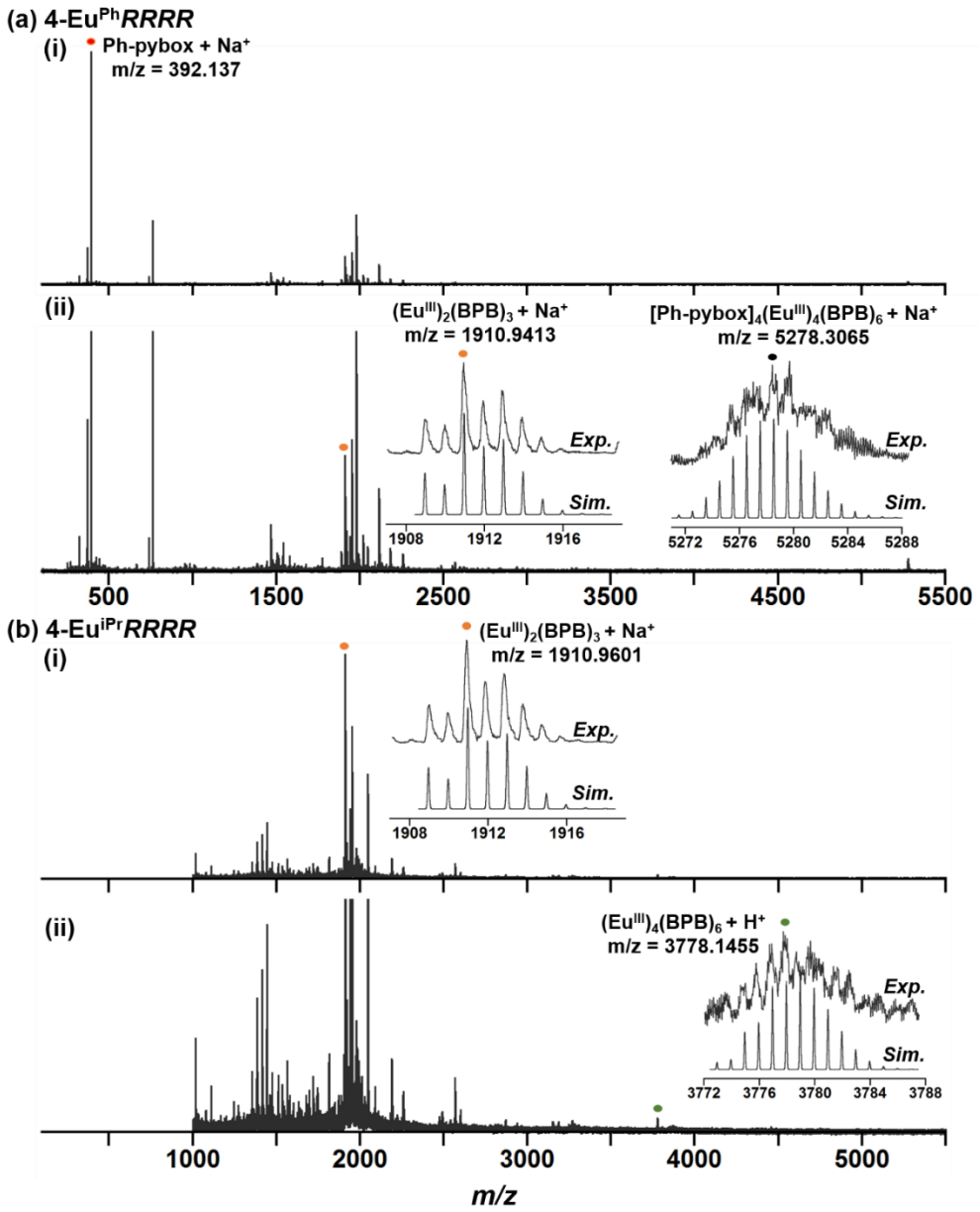

Figure 3.10. (a-i) ESI(+)-MS of **4-Eu^{Ph}*RRRR*** in chloroform with the flow of methanol. (a-ii) ESI(+)-MS of **4-Eu^{Ph}*RRRR*** with the intensity scaled down. Inset: Isotopically resolved signals at *m*/*z* = 5278.30 and *m*/*z* = 1910.94 with the calculated isotopic distributions for $\{[(R)\text{-Ph-pybox})]_4Eu_4(BPB)_6 + Na\}^+$ and $\{Eu_2(BPB)_3 + Na\}^+$, respectively. (b-i) ESI(+)-MS of **4-Eu^{iPr}*RRRR*** in chloroform with the flow of methanol. Inset: Isotopically resolved signals at *m*/*z* = 1910.96 with the calculated isotopic distributions for $\{Eu_2(BPB)_3 + Na\}^+$. (a-ii) ESI(+)-MS of **4-Eu^{iPr}*RRRR*** with the intensity scaled down. Inset: Isotopically resolved signals at *m*/*z* = 3778.15 with the calculated isotopic distributions for $\{Eu_4(BPB)_6 + Na\}^+$.

3.6 Emission and CPL Profile

Upon excitation at 360nm, the Eu^{III} self-assemblies gave characteristics red ($^5D_0 \rightarrow {}^7F_J$, J = 0-4) luminescence, respectively in solution (chloroform or toluene) and solid-state (KBr pellet). Nearly quantitative fits between the crystal-field splitting of emission in solution and solid state are observed for all the Eu^{III} self-assemblies (Figure 3.11). The $^5D_0 \rightarrow {}^7F_0$ emission band displays one narrow line, whereas $^5D_0 \rightarrow {}^7F_1$ and $^5D_0 \rightarrow {}^7F_2$ emission bands split into several crystal-field level. Intense peak is always observed at hypersensitive $^5D_0 \rightarrow {}^7F_2$ transition with respect to the $^5D_0 \rightarrow {}^7F_1$ transition, indicating non-centrosymmetric nature of the nona-coordinated Eu^{III} geometries. The degree of Eu^{III} site symmetry can be assessed through the relative total intensity ratio of the $^5D_0 \rightarrow {}^7F_2$ transition to $^5D_0 \rightarrow {}^7F_1$ transition, A_{rel}(TI)[61-62]. Taking into 5% measurement error, all the $(Pybox)_4(Eu^{III})_4(BPB)_6$ self-assemblies have a similar A_{rel}(TI) value of about 13 (Table 3.2).

Table 3.2. Relative Total Intensity Ratio of Eu^{III} self-assemblies in chloroform, toluene and KBr pellet.

Eu^{III} self-assemblies	**Relative Total Intensity Ratio, A_{rel}(TI)**		
	$CHCl_3$	**C_7H_8**	**KBr**
4-Eu^{Ph}*RRRR* (4-Eu^{Ph}*SSSS*)	13.48 (13.56)	13.28 (13.29)	12.51 (12.21)
4-Eu^{iPr}*RRRR* (4-Eu^{iPr}*SSSS*)	13.49 (13.53)	13.81 (13.81)	12.44 (12.85)

* Estimated measurement error for A_{rel}(TI) = 5%.

The CPL profile of (*R*)- and (*S*)-isomers display almost complete mirror signals with each other (Figure 3.11c,d,e and f) The CPL profile of **4-Eu^{Ph}*RRRR*/4-Eu^{Ph}*SSSS*** in solution are non-identical to the solid state (Figure 3.11c and e), suggesting that the solution structure of **4-Eu^{Ph}*RRRR*/4-Eu^{Ph}*SSSS*** deviates from a D_2 symmetry, in agreement with the NMR analysis (Figure 3.9a and b). On the other hand, **4-Eu^{iPr}*RRRR*/4-Eu^{iPr}*SSSS*** displays identical CPL signature in both solution and solid-state (Figure 3.11d and f). Deviation from D_2 symmetrical structure of **4-Eu^{iPr}*RRRR*/4-Eu^{iPr}*SSSS*** in chloroform suggested in NMR analysis

(Figure 3.9c) gave a similar CPL profile to solid state spectra, suggesting there should be some structural similarity of **4-Eu^{iPr}*RRRR*/4-Eu^{iPr}*SSSS*** in chloroform and solid-state.

In the solution CPL spectra of **4-Eu^{Ph}*RRRR***, the sign of CPL follows the sequence of (+) at $^5D_0 \rightarrow {}^7F_1$ transition and (–, +, –) at $^5D_0 \rightarrow {}^7F_2$ transition. Conversely, the sign of CPL follows the sequence of (–) at $^5D_0 \rightarrow {}^7F_1$ transition and (–, +, –) at $^5D_0 \rightarrow {}^7F_2$ transition in the solution CPL spectra of **4-Eu^{iPr}*RRRR***. The CPL efficiency of **4-Eu^{Ph}*RRRR*/4-Eu^{Ph}*SSSS*** and **4-Eu^{iPr}*RRRR*/4-Eu^{iPr}*SSSS*** in toluene at the magnetic transition ($^5D_0 \rightarrow {}^7F_1$) band are ~|0.17| and ~|0.10| respectively.

Table 3.3. Luminescence dissymmetry factor (g_{lum}) and quantum yield (ϕ_{em})

Eu^{III} self-assemblies	**g_{lum} ($^5D_0 \rightarrow {}^7F_1$)**		**ϕ_{em}**
	$CHCl_3$	**C_7H_8**	**($CHCl_3$)**
4-Eu^{Ph}*RRRR*	(~598 nm)		0.14
(4-Eu^{Ph}*SSSS*)	0.16	0.17	(0.14)
	(-0.16)	(-0.17)	
4-Eu^{iPr}*RRRR*	(~594.5nm)		0.14
(4-Eu^{iPr}*SSSS*)	-0.23	-0.09	(0.14)
	(0.24)	(0.10)	

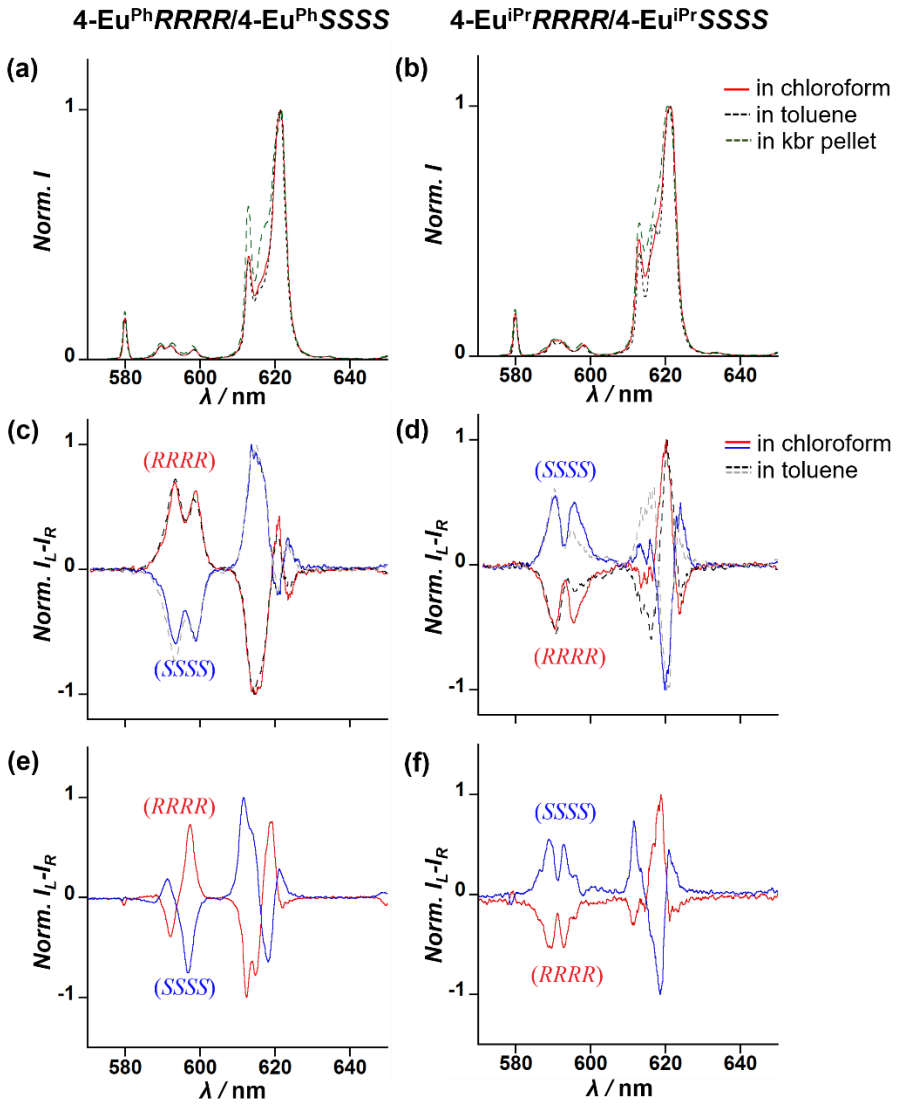

Figure 3.11. Emission spectra of (a) **4-Eu^{Ph}*RRRR*** , and (b) **4-Eu^{iPr}*RRRR*** in chloroform (red solid, conc. = 3.4 × 10^{-6} M), toluene (black dashed, conc. = 3.4 × 10^{-6} M) and kbr pellet (green dashed) at 298K. Normalized CPL spectra of (c) **4-Eu^{Ph}*RRRR*/4-Eu^{Ph}*SSSS***, and (d) **4-Eu^{iPr}*RRRR*/4-Eu^{iPr}*SSSS*** in chloroform and toluene at 298K (conc. = 3.4 × 10^{-6} M; red solid and black dashed for the (*R*)-enantiomers in chloroform and toluene, respectively; blue and grey dashed line for the (*S*)- enantiomers in chloroform and toluene, respectively). Normalized CPL spectra of (e) **4-Eu^{Ph}*RRRR*/4-Eu^{Ph}*SSSS***, and (f) **4-Eu^{iPr}*RRRR*/4-Eu^{iPr}*SSSS*** in KBr pellet (red and blue solid line for the (*R*)- and (*S*)-enantiomers, respectively).

4.0 CHIRAL SELF-ASSEMBLED OF SQUARE ANTIPRISM $Ln^{III}_8L_8(Pybox)_8$

4.1 Introduction

In the chapter 2 and 3, tetranuclear Eu^{III} grid and tetrahedron based on achiral anionic bis-*β*-diketonates, L ligands with larger GC ($[Eu^{III}_4L_6]$ = 10) were fabricated through sequential reaction of $[Eu^{III}_2L_3]$ (GC of 5) with chiral co-ligands (*R*)- or (*S*)-Pybox. Rational design of new CPL-active self-assemblies was demonstrated by controlling the length of the spacer in the bis-*β*-diketonates ligand. Different type of ligand-to-ligand interactions revealed in the X-ray crystal structures are found to stimulate different ligands wrapping arrangement around Eu^{III} cores.

In this chapter, rational design of new chiral Ln^{III} self-assemblies with larger GC was demonstrated by manipulating the GC factor in the Ln_mL_n precursor complexes. Increasing the connectivity of the bridging ligands enables formation of precursor complexes with larger GC (m + n) and thus expanded chiral self-assemblies with GC of 2(m + n). Through this GC concept, new geometrical intriguing chiral octanuclear Eu^{III} and Tb^{III} circular helicates based on tris-*β*-diketonates ligand were prepared. The octanuclear Eu^{III} and Tb^{III} exhibit large circular polarization and display remarkable CPL dissymmetry ($|g_{lum}|$ = 1.25 and 0.25 in Eu^{III} and Tb^{III} self-assemblies).

4.2 Preparation

Fluorinated tris-*β*-diketonate, H_3(TTP) and H_3(THP) ligands were synthesized from the Claisen Condensation between a 1,3,5-triacetylbenzene and three non-enolizable trifluoroethyl acetate or ethyl heptafluorobutyrate (Figure 4.1).

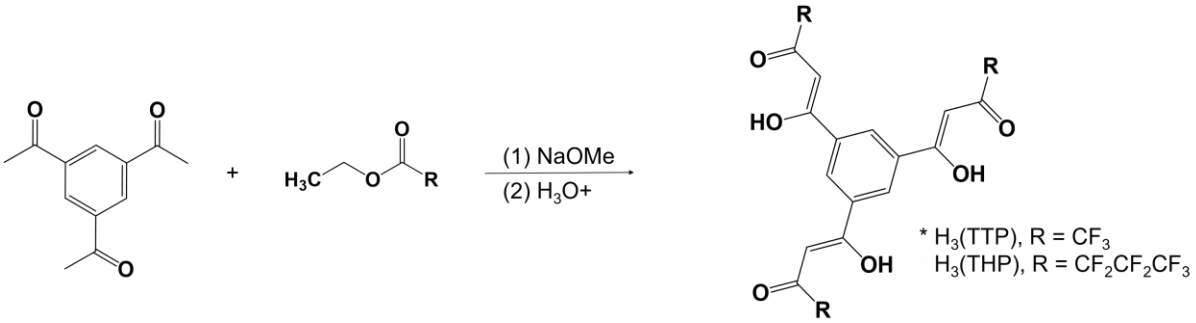

Figure 4.1. Reaction scheme of H_3(TTP) and H_3(THP) ligands

Tris-*β*-diketonate chelated Eu^{III} coordination complexes can be prepared by reacting the ligand, H_3L with Eu^{III} chloride hexahydrate ($Eu^{III}Cl_3.6H_2O$) in an appropriate ratio under basic condition. The reaction of the chelating triple negative charges anion derived from tris-*β*-diketonate, H_3L with the Eu^{III} in a 1:1 ratio produce neutral, tetranuclear, racemic tetrahedral Eu^{III} cluster, ΔΔΔΔ-[$Eu^{III}_4L_4$] and ΛΛΛΛ-[$Eu^{III}_4L_4$] (Figure 4.2). [Eu^{III}_4(THP)$_4$] undergoes structural conformation change to hexanuclear [Eu^{III}_6(THP)$_6$] trigonal antiprism cluster in acetone and DME solution, probably due to the long heptafluoropropyl chains in the THP ligands that induce steric effects in the complexation (refer to Figure *A14*e for ^{19}F- NMR spectrum in acetone; Figure *A2*b for poor resolved [Eu^{III}_6(THP)$_6$·6DME] crystal structure). Nonetheless, it was found that [Eu^{III}_4(THP)$_4$] could be the most probable species in the methanol, as suggested from the ^{19}F-NMR analysis (Figure *A14*d). [Tb^{III}_4(THP)$_4$] can prepared in a similar manner as [Eu^{III}_4(THP)$_4$].

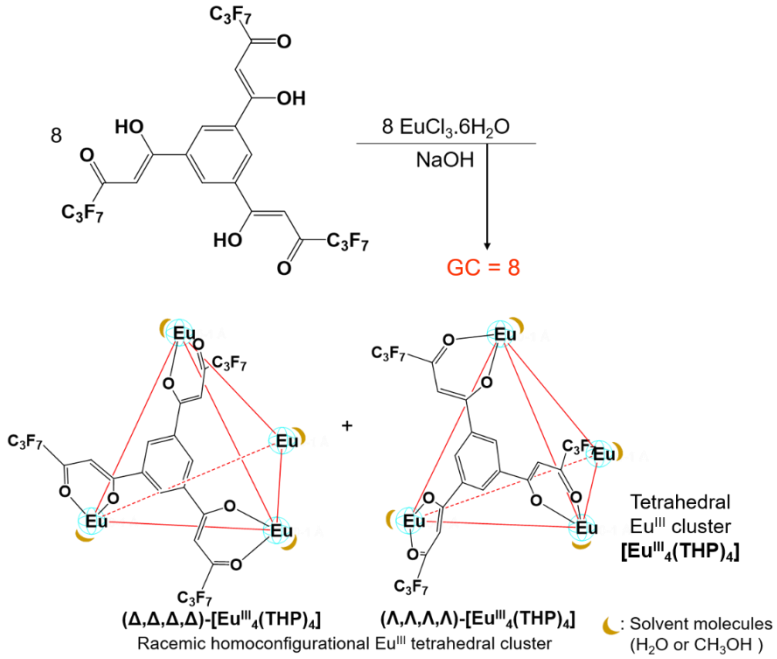

Figure 4.2. Reaction scheme of $[Eu^{III}{}_4L_4]$, L= THP.

Reaction between racemic tetranuclear tetrahedral $[Ln^{III}{}_4(THP)_4]$ cluster and (*R)* or (*S)*-iPr-pybox resulted in stereoselective formation of octanuclear, D_4-point symmetrical square-antiprism Ln^{III} self-assemblies with the general formula of $[(R)$- or (S)-^{i}Pr-Pybox$]_8Ln^{III}{}_8(THP)_8$, where Ln^{III} are Eu^{III} and Tb^{III} (Figure 4.3). Single crystal suitable for analysis can be obtained from the slow evaporation of toluene into the chloroform solution containing sample. X-ray crystallographic analysis revealed that racemic mixtures of homoconfigurational (Δ,Δ,Δ,Δ,Δ,Δ,Δ,Δ)/(Λ,Λ,Λ,Λ,Λ,Λ,Λ,Λ)- stereoisomers no longer be observed in both crystals of **5-Ln^{iPr}*RRRRRRRR*** and **5-Ln^{iPr}*SSSSSSSS***. The presence of chiral ^{i}Pr-pybox ligands have induced selective formation of (Δ,Δ,Δ,Δ,Δ,Δ,Δ,Δ)-$[(R)$-^{i}Pr-pybox$]_8Ln^{III}{}_8(THP)_8$ (**5-Ln^{iPr}*RRRRRRRR***) and (Λ,Λ,Λ,Λ,Λ,Λ,Λ,Λ)-$[(S)$-^{i}Pr-pybox$]_8Ln^{III}{}_8(THP)_8$ (**5-Ln^{iPr}*SSSSSSSS***).

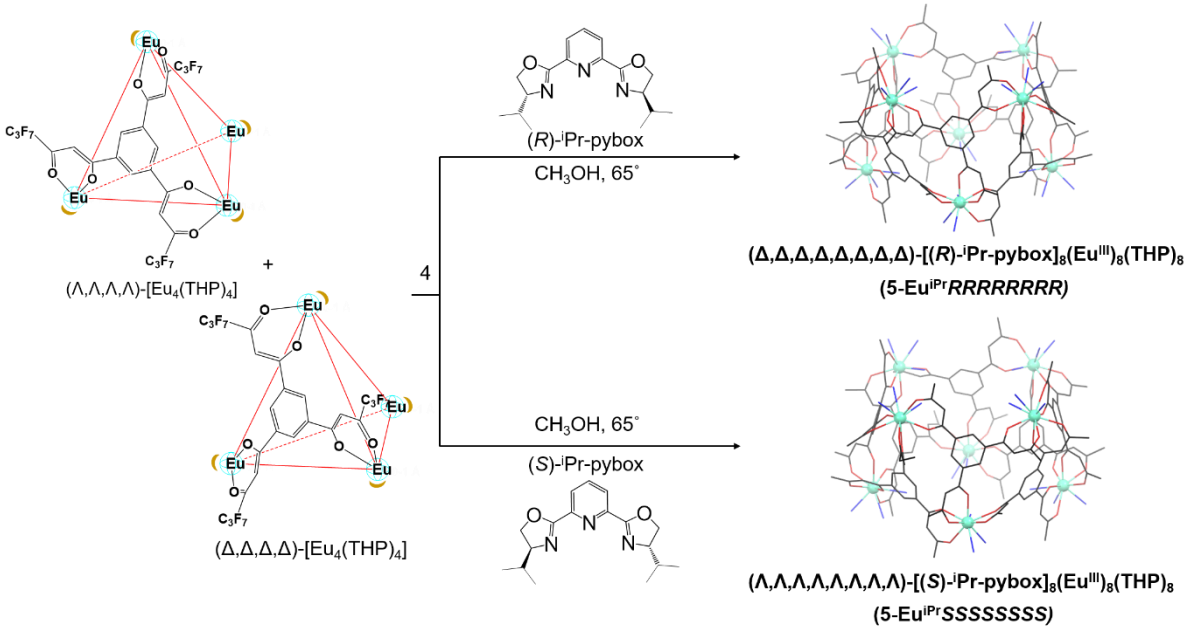

Figure 4.3. Reaction Scheme of **5-Eu^{iPr}*RRRRRRRR*** and **5-Eu^{iPr}*SSSSSSSS***

4.3 Crystal structure

Figure 4.4 shows the crystal structures of **5-Eu^{iPr}*RRRRRRRR*/5-Eu^{iPr}*SSSSSSSS***, where the *R*- and *S*-isomers are non-superimposable complete mirror images of each other (refer to Table *A9* for crystallographic data). **5-Eu^{iPr}*RRRRRRRR*/5-Eu^{iPr}*SSSSSSSS*** are crystallized in tetragonal system with space group of I4.

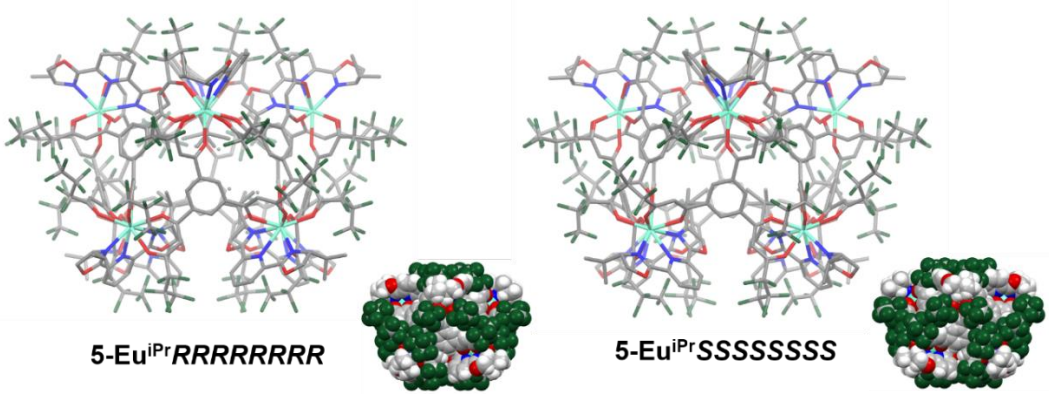

Figure 4.4. X-ray crystal structure of (a) **5-Eu^{iPr}*RRRRRRRR*/5-Eu^{iPr}*SSSSSSSS***

The crystal structure of **5-Eu^{iPr}*RRRRRRRR*/5-Eu^{iPr}*SSSSSSSS*** can be described as square antiprism, with eight Eu^{III} ions defining its vertices and eight THP ligands occupying each of the triangular faces. The antiprism is composed of four asymmetric units of [(*R*)- or (*S*)-iPr-pybox]$_2$$Eu^{III}_2(THP)_2$ helicate, which coordinated in a closed cyclic manner to form a [(*R*)- or (*S*)-iPr-pybox]$_8$$Eu^{III}_8(THP)_8$ circular helicate (Figure 4.5a). The **5-Eu^{iPr}*RRRRRRRR*/5-Eu^{iPr}*SSSSSSSS*** circular helicate can be considered to exhibits D_4-point symmetry, with mean of two parallel Eu-Eu-Eu-Eu square planes perpendicular to the C_4-axis (Figure 4.5b). Due to the crystal packing effects, slight deviation in the Eu-Eu distances, Eu-Eu-Eu angles and dihedral angle of THP ligand from perfect D_4-point symmetry are observed in the crystal structure.

As shown in Figure 4.5b, presence of a C_4 rotational symmetry involves a pair of four equivalent Eu^{III} ions (Eu_1 and Eu_2) in **5-Eu^{iPr}*RRRRRRRR*** with Eu_1-Eu_1, Eu_2-Eu_2, Eu_1-Eu_2 and

Eu_2-Eu_1 distances of 10.626 Å ,10.622 Å, 9.906 Å, and 9.988 Å, respectively. There are two similar pairs of three Eu-Eu-Eu interior angles (64.5˚, 58.1˚, and 57.3˚), making up eight acute scalene triangular Eu-Eu-Eu planes.

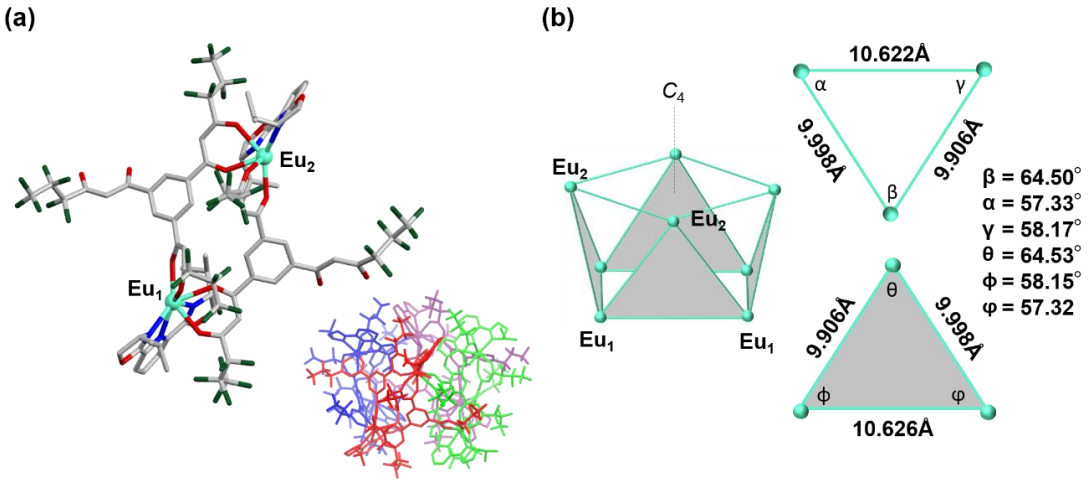

Figure 4.5. (a) Asymmetric units of [(*R*)- or (*S*)-iPr-pybox]$_2$Eu$^{III}_2$(THP)$_2$ helicate of **5-Eu^{iPr}*RRRRRRRR***. (b) Eu-Eu distances and Eu-Eu-Eu angles **5-Eu^{iPr}*RRRRRRRR***.

Table 4.1. Twisting angle of THP ligands in the X-ray crystal structures of **5-Eu^{iPr}*RRRRRRRR***/**5-Eu^{iPr}*SSSSSSSS***.

Eu(III) self-assemblies	**Degree of ligand twisting (˚)**	
	THP$_A$	**THP$_B$**
5-Eu^{iPr}*RRRRRRRR*	-55.27	-55.97
	-70.94	-68.85
	-82.87	-79.11
5-Eu^{iPr}*SSSSSSSS*	55.44	54.44
	68.89	71.12
	78.76	81.30

Each THP coordinates to three Eu^{III} ions as a helical plane, consisting three dihedral angles from two corresponding coordinated Eu^{III} ions. The dihedral angles of two THP ligands (THP$_A$ and THP$_B$) of [(*R*)- or (*S*)-iPr-pybox]$_2$Eu$^{III}_2$(THP)$_2$ asymmetric unit are summarized in Table 4.1. The degree of ligand twisting angles of THP$_A$ and THP$_B$ differ by 1˚ to 4˚. All the

THP ligands of **5-Eu^{iPr}*RRRRRRRR*** are in Δ-form, whereas **5-Eu^{iPr}*SSSSSSSS*** consists of only Λ-form THP ligands.

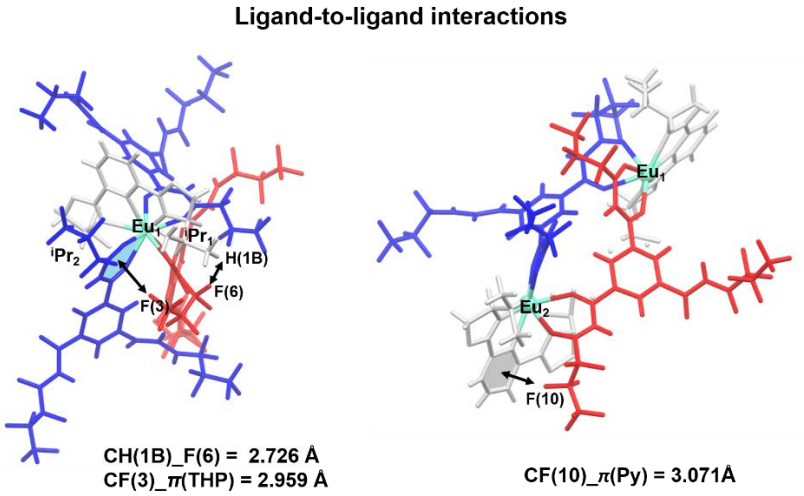

Figure 4.6. Ligand-to-ligand interactions of **5-Eu^{iPr}*RRRRRRRR***.

X-ray crystallography revealed CH_F interactions between heptafluoropropyl units of THP and isopropyl arm ($^{i}Pr^{1}$) of ^{i}Pr-pybox, which are probably the key factor for the stereoselective formation of homoconfigurational and homochiral assembly, (Δ,Δ,Δ,Δ,Δ,Δ,Δ,Δ)-[(*R*)-^{i}Pr-pybox]$_8$(Eu^{III})$_8$(THP)$_8$ and (Λ,Λ,Λ,Λ,Λ,Λ,Λ,Λ)-[(*S*)-^{i}Pr-pybox]$_8$(Eu^{III})$_8$(THP)$_8$ (Figure 4.6, $d_{CH\_F}(Eu_1)$ = 2.726 Å). The other isopropyl arm ($^{i}Pr^{2}$) which reside in the cavity of square antiprism has no appreciable molecular interaction with THP ligands. As mentioned in chapter 2, [Eu$_4$(THP)$_4$] type tetrahedral cluster was formed from the self-assembly of Eu^{III} with THP and 2,2'-bipyridine due to the absence of possible interactions between THP and 2,2'-bipyridine. Therefore, such ligand-to-ligand interactions is believed to facilitate the formation of the [Eu$^{III}_8$(THP)$_8$] circular helicate. Interactions between ^{i}Pr-pybox with ^{i}Pr-pybox (CH_O), ^{i}Pr-pybox with THP (CH_F and CF_π) and THP with THP (CF_F and CF_π) are also found in the crystal structure (Figure *A13*). These intramolecular interactions

probably help to stabilize the final D_4-point symmetrical complex. Detailed interactions analysis is given in Appendices (Table *A16*).

All the Eu^{III} ions can be considered having distorted capped square antiprism geometry, where nine vertices are saturated with three nitrogen atoms of the Ph-pybox ligand and six oxygen atoms of three *β*-diketonates moieties of THP ligands (Figure 4.7a, Figure *A11*, and Table *A15*). Eight Eu^{III} coordination geometries are non-distinguishable in term of the outer-sphere ligand orientations (Figure 4.7b). The ^{i}Pr-Pybox ligand is skewed from the main axis in the Eu^{III} coordination geometries of **5-Eu^{iPr}*RRRRRRRR*/5-Eu^{iPr}*SSSSSSSS***.

Chiral self-assemblies of **5-Tb^{iPr}*RRRRRRRR*/5-Tb^{iPr}*SSSSSSSS*** are isomorphous of the **5-Eu^{iPr}*RRRRRRRR*/5-Eu^{iPr}*SSSSSSSS***. Their X-ray crystal structures are given in the Figure *A8* (refer to Table *A10* for crystallographic data).

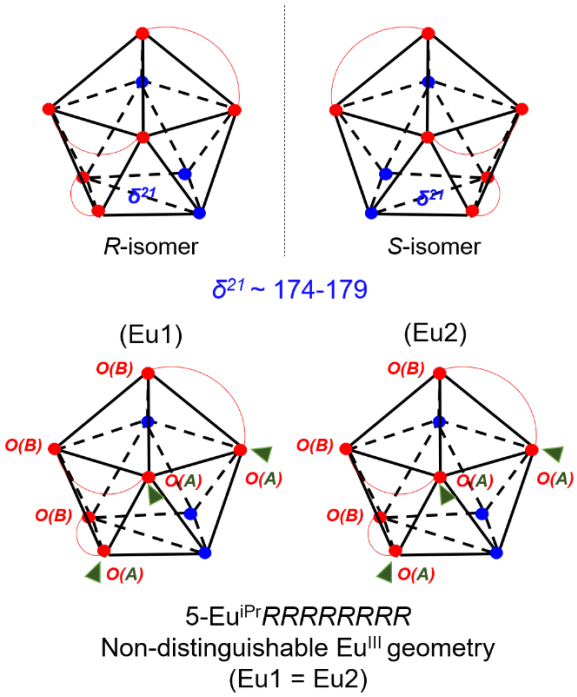

Figure 4.7. (a) Coordination geometry of (a) **5-Eu^{iPr}*RRRRRRRR*/5-Eu^{iPr}*SSSSSSSS***. O(A) and O(B) are oxygen atoms in the carbonyl units of bis-*β*-diketonate ligands which are next to the fluoroalkyl chains and phenyl rings, respectively. Green triangles in the Eu geometries designate linkage of the fluoroalkyl chain.

4.3 NMR Analysis

The ^{19}F NMR spectrum of **5-Eu^{iPr}*RRRRRRRR*** shows three characteristic CF_3 fluorine peaks, in agreement with the D_4-point symmetrical square antiprism structure of $Eu^{III}_8(THP)_8$ circular helicate (Figure 4.8). Each fluoroalkyl chain of THP ligands contribute to one fluorine NMR signals. Individual pairs of geminal CF_2 fluorine peaks are found, probably due to the chiral coordination environment.

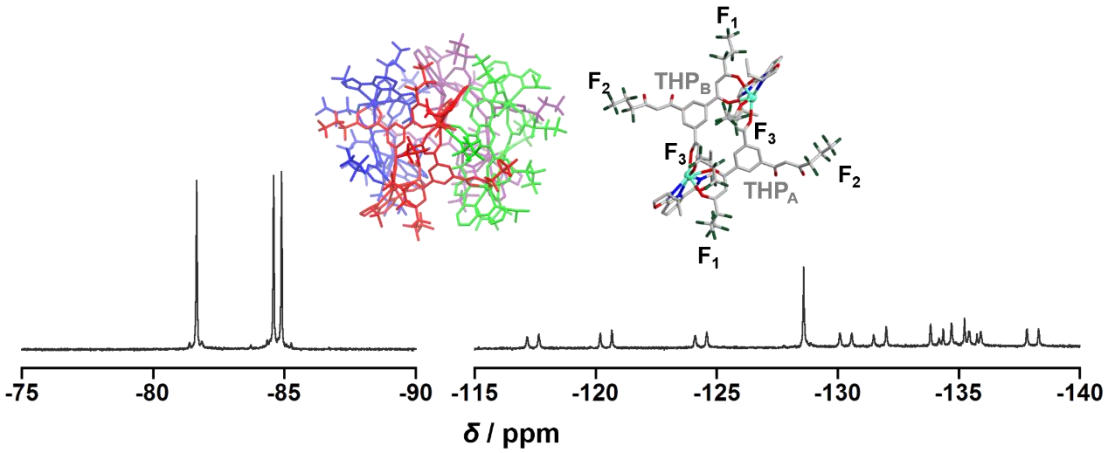

Figure 4.8. ^{19}F-NMR spectrum of **5-Eu^{iPr}*RRRRRRRR*** in $CDCl_3$.

4.4 Mass Analysis

The mass signals of $[^{i}Pr\text{-pybox}]_8(Eu^{III})_8(THP)_8$ could not be detected in both ESI(+) and MALDI mass spectrometry However, the ESI(+)-MS of **5-Eu^{iPr}*RRRRRRRR*/5-Eu^{iPr}*SSSSSSSS*** detect a weak signal of $Eu^{III}{}_8(THP)_8$ type complex with mass distribution *m*/*z* = 9662.578, which can be assigned to the mass of $\{[^{i}Pr\text{-pybox}]_7(Eu^{III})_8(THP)_8 + Na\}^+$ (Figure 4.9a-ii inset). In the MALDI-MS spectra of **5-Eu^{iPr}*RRRRRRRR*/5-Eu^{iPr}*SSSSSSSS***, mass peaks with mass distribution of *m*/*z* = 7661.953 and *m*/*z* = 7853.981 are displayed, corresponding to the mass of $[(Eu^{III})_8(THP)_8(OH_2)(C_7H_8) + Na]^+$ and $\{[(R)\text{-}^{i}Pr\text{-pybox}](Eu^{III})_8(THP)_8 + Na\}^+$ respectively (Figure 4.9a-iii inset). Similarly, mass signals of $Tb^{III}{}_8(THP)_8$ type complex were detected in both ESI(+) and MALDI-MS of **5-Tb^{iPr}*RRRRRRRR*/5-Tb^{iPr}*SSSSSSSS***. The detected mass signals with theoretical isotopic distribution are shown in the Figure 4.9b.

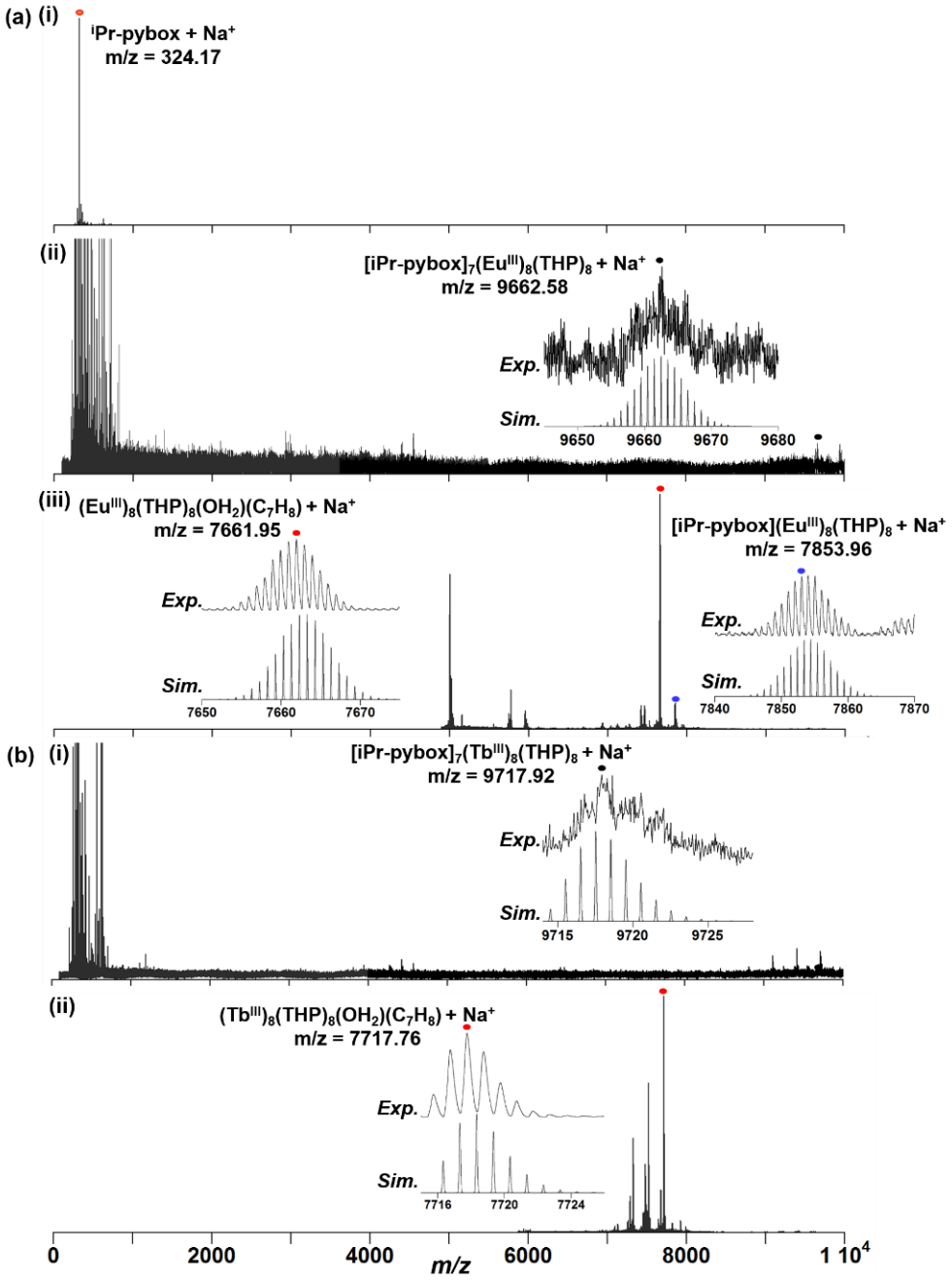

Figure 4.9. (a-i) ESI(+)-MS of **5-Eu^{iPr}*RRRRRRRR*** in chloroform with the flow of methanol. (a-ii) ESI(+)-MS of **5-Eu^{iPr}*RRRRRRRR*** with the intensity scaled down. Inset: Isotopically resolved signals at *m*/*z* = 9662.58 with the calculated isotopic distributions for $\{[(R)\text{-}^{i}\text{Pr-pybox})]_7Eu_8(THP)_8 + Na\}^+$. (a-iii) MALDI-MS of **5-Eu^{iPr}*RRRRRRRR*** in DCTB matrix. Inset: Isotopically resolved signals at *m*/*z* = 7661.95 and *m*/*z* = 7853.96, with their calculated isotopic distributions for $\{[(R)\text{-iPr-pybox})]Eu_8(THP)_8 + Na\}^+$ and $\{Eu_8(THP)_8(OH_2)(C_7H_8) + Na\}^+$, respectively. (b-i) ESI(+)-MS of **5-Tb^{iPr}*RRRRRRRR*** in chloroform with the flow of methanol. Inset: Isotopically resolved signals at *m*/*z* = 9717.92 with the calculated isotopic distributions for $\{[(R)\text{-}^{i}\text{Pr-pybox})]_7Tb_8(THP)_8 + Na\}^+$. (b-ii) MALDI-MS of **5-Tb^{iPr}*RRRRRRRR*** in DCTB matrix. Inset: Isotopically resolved signals at *m*/*z* = 7717.76 with their calculated isotopic distributions for $\{Tb_8(THP)_8(OH_2)(C_7H_8) + Na\}^+$.

4.5 Emission and CPL Profile

Upon excitation at 360nm, the Tb^{III}, and Eu^{III} self-assemblies gave characteristics green ($^5D_4 \rightarrow {}^7F_J$, J = 6-3) and red ($^5D_0 \rightarrow {}^7F_J$, J = 0-4) luminescence, respectively in solution (chloroform or toluene) or solid-state (KBr pellet). Nearly quantitative fit between the crystal-field splitting of emission in solution and solid state are observed in Eu^{III} self-assemblies (Figure 4.11a). In emission spectra of Eu^{III} self-assemblies, the $^5D_0 \rightarrow {}^7F_0$ emission band displays one narrow line, whereas $^5D_0 \rightarrow {}^7F_1$ and $^5D_0 \rightarrow {}^7F_2$ emission bands split into several crystal-field level. Intense peak is always observed at hypersensitive $^5D_0 \rightarrow {}^7F_2$ transition with respect to the $^5D_0 \rightarrow {}^7F_1$ transition, indicating non-centrosymmetric nature of the nona-coordinated Eu^{III} geometries. The degree of Eu^{III} site symmetry can be assessed through the relative total intensity ratio of the $^5D_0 \rightarrow {}^7F_2$ transition to $^5D_0 \rightarrow {}^7F_1$ transition, $A_{rel}(TI)$[61-62]. Octanuclear $(^i\text{Pr-Pybox})_8(Eu^{III})_8L_8$ circular helicates give a $A_{rel}(TI)$ value of ~ 8.5.

Table 4.2. Relative Total Intensity Ratio of Eu^{III} self-assemblies in chloroform and KBr pellet.

Eu^{III} self-assemblies	**Relative Total Intensity Ratio, $A_{rel}(TI)$**	
	$CHCl_3$	**KBr**
5-Eu^{iPr}*RRRRRRRR* **(5-Eu^{iPr}*SSSSSSSS*)**	8.25 (9.03)	8.25 (8.81)

* Estimated measurement error for $A_{rel}(TI)$ = 5%.

The CPL profiles of *R*- and *S*- isomers display almost complete mirror signals with each other (Figure 4.11c, d, and e). The CPL spectra of **5-Eu^{iPr}*RRRRRRRR*** and **5-Eu^{iPr}*SSSSSSSS*** in solution are nearly identical to the corresponding spectra in solid state (Figure 4.11c, and e). The octanuclear circular helicate, $(^i\text{Pr-pybox})_8Ln^{III}{}_8(THP)_8$ achieve highest g_{lum} value among these studied Ln^{III} self-assemblies of bis-/tris-β-diketonates. g_{lum} value of the chiral self-assembly of **5-Eu^{iPr}*RRRRRRRR*** and **5-Eu^{iPr}*SSSSSSSS*** were determined to be -1.25 and +1.24 at λ = 591 nm in chloroform respectively. Such large g_{lum} value results in a visible

luminescence through left and right circularly polarized filter at 592nm in solution and PMMA film (Figure 4.10; clear distinct emission between *R*- and *S*-isomers were observed). The octanuclear Tb^{III} counterpart, **5-Tb^{iPr}*RRRRRRRR*/5-Tb^{iPr}*SSSSSSSS*** exhibited g_{lum} value of +0.25/-0.25 in chloroform (Figure 4.11d for CPL spectra).

Table 4.3. Luminescence dissymmetry factor (g_{lum}), quantum yield (ϕ_{em}) and emission lifetime (τ) of Eu^{III} self-assemblies

Eu^{III} self-assemblies	**g_{lum} ($^5D_0 \rightarrow {}^7F_1$)**		**ϕ_{em} ($CHCl_3$)**	**τ/ms ($CHCl_3$)**
	$CHCl_3$	**C_7H_8**		
5-Eu^{iPr}*RRRRRRRR*	(~592.5 nm)		0.15	0.86
(5-Eu^{iPr}*SSSSSSSS*)	-1.25 (1.24)	-1.25 (1.24)	(0.15)	(0.86)
Tb^{III} self-assemblies	**g_{lum} ($^5D_4 \rightarrow {}^7F_5$) ($CHCl_3$)**		**ϕ_{em} ($CHCl_3$)**	**τ/μs ($CHCl_3$)**
5-Tb^{iPr}*RRRRRRRR	(~541 nm)		0.0013	5.37
(5-Tb^{iPr}*SSSSSSSS*)	0.25 (-0.25)			

* g_{lum} value was obtained from the CPL instruments.

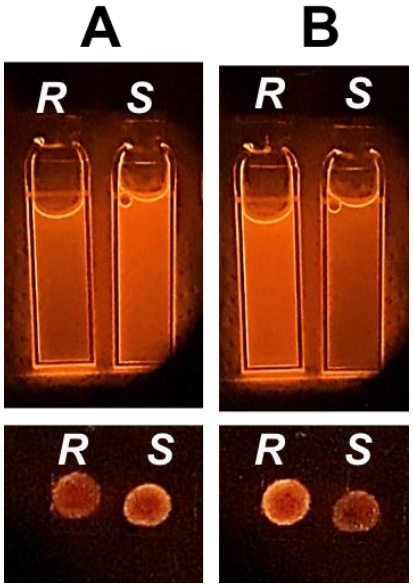

Figure 4.10. Visible luminescence images of **5-Eu^{iPr}*RRRRRRRR*** (*R*) and **5-Eu^{iPr}*SSSSSSSS*** (*S*) in chloroform (top) and PMMA films (bottom) with a band path filter (592 nm) and (A) left-, (B) right-circularly polarized filter.

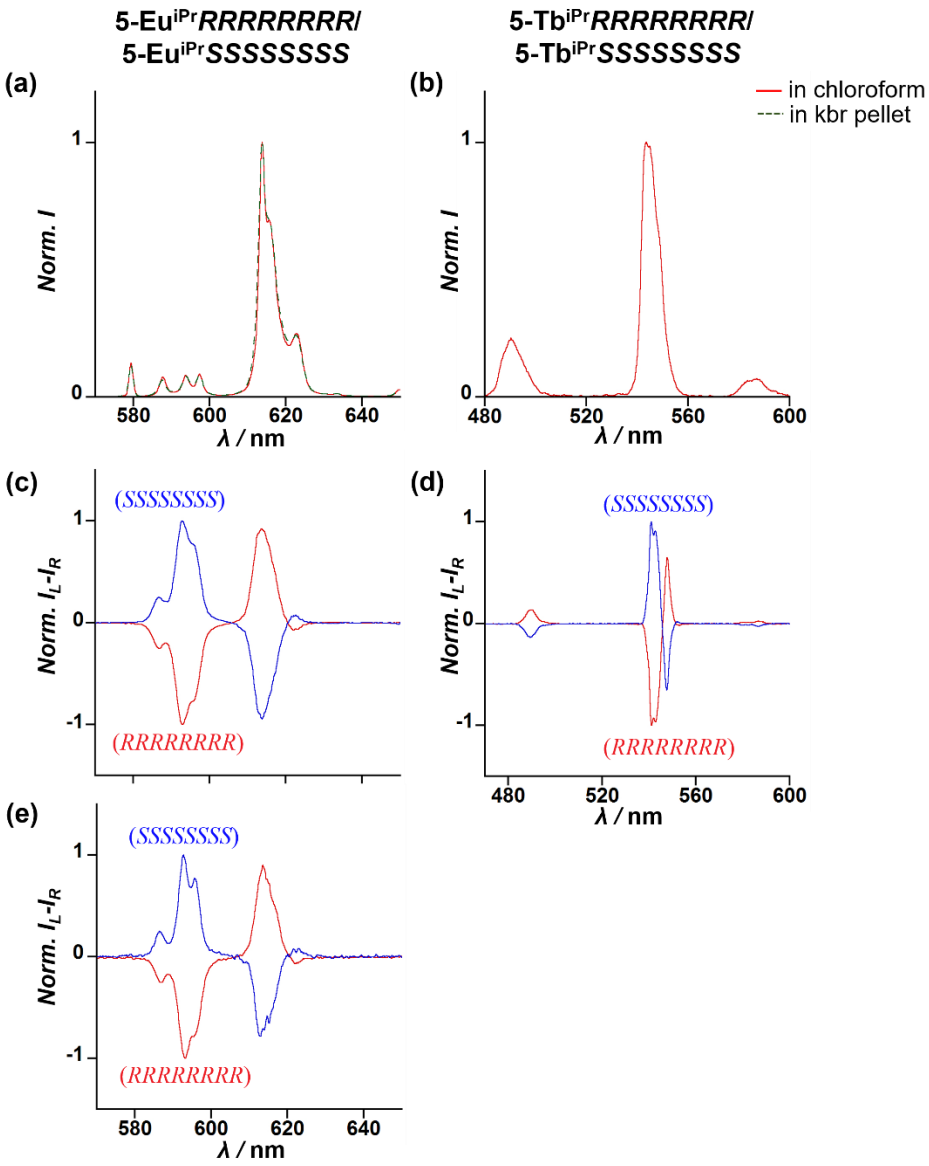

Figure 4.11. Emission spectra of (a) **5-Eu^{iPr}*RRRRRRRR***, and (b) **5-Tb^{iPr}*RRRRRRRR*** in chloroform (red solid, conc. = 2.6 × 10^{-5} M), and kbr pellet (green dashed) at 298K. Normalized CPL spectra of (c) **5-Eu^{iPr}*RRRRRRRR*/5-Eu^{iPr}*SSSSSSSS***, and (d) **5-Tb^{iPr}*RRRRRRRR*/5-Tb^{iPr}*SSSSSSSS*** in chloroform at 298K (conc. = 2.6 × 10^{-5} M; red and blue solid line for the (*R*)- and (*S*)- enantiomers in chloroform, respectively). Normalized CPL spectra of (e) **5-Eu^{iPr}*RRRRRRRR*/5-Eu^{iPr}*SSSSSSSS*** in KBr pellet (red and blue solid line for the (*R*)- and (*S*)- enantiomers in chloroform, respectively).

5.0 CONCLUSION AND PROSPECT

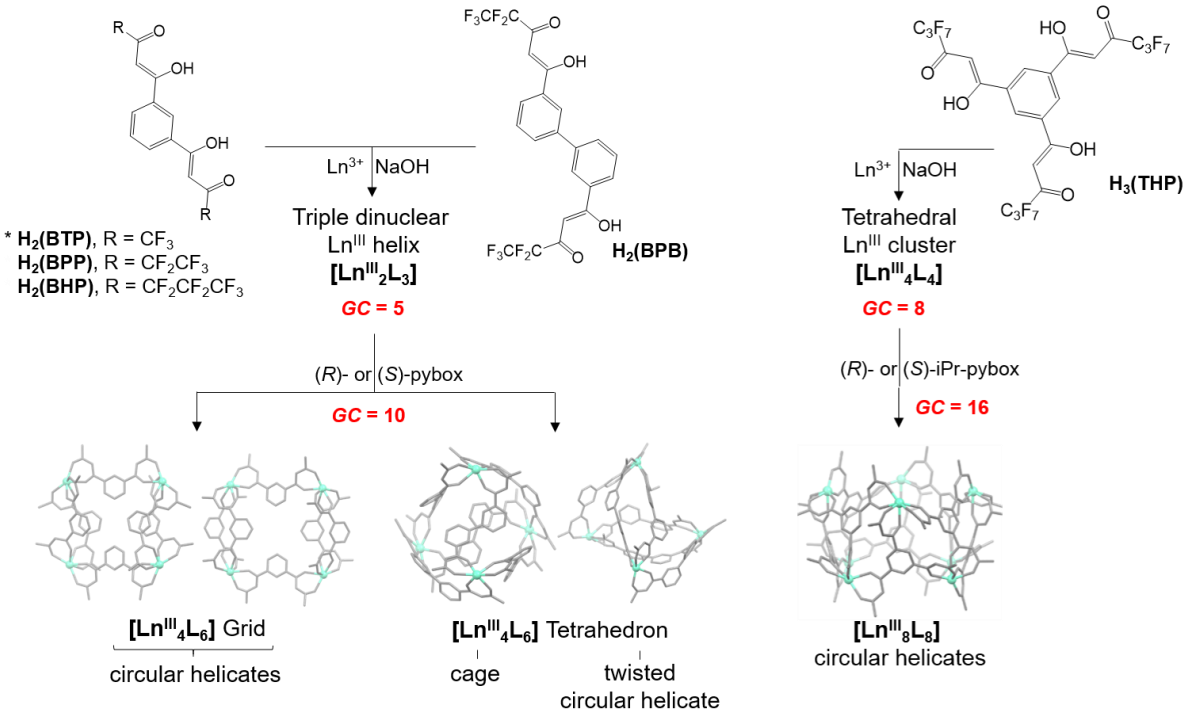

Figure 5.1. Reaction scheme of $[Ln^{III}_4L_6]$ alternating circular helicate or tetrahedral cluster and $[Ln^{III}_8L_8]$ circular helicate.

Novel expanded nona-coordinated lanthanide(III) self-assemblies ($Ln^{III}_4L_6$ or $Ln^{III}_8L_8$) with a larger global complexity (*GC* = 4 + 6 = 10 for $Ln^{III}_4L_6$; *GC* = 8 + 8 = 16 for $Ln^{III}_8L_8$) are successfully generated by sequential coordination of $[Ln^{III}_2L_3]$ (*GC* = 2 + 3 = 5) or $[Ln^{III}_4L_4]$ (*GC* = 4 + 4 = 8) with chiral co-ligands (*R*)- or (*S*)-Pybox. Three new types of lanthanide(III) (Ln^{III}) self-assemblies based on the achiral anionic bis-/tris-*β*-diketonate (L) and chiral Pybox ligands were developed: (a) D_2- or C_{2h}-symmetrical tetranuclear $[Ln^{III}_4L_6]$ quadrilateral grid-like circular helicates, (b) D_2-symmetrical tetranuclear $[Ln^{III}_4L_6]$ tetrahedron and (c) D_4-point symmetrical octanuclear $[Ln^{III}_8L_8]$ square antiprism (Figure 5.1). X-ray crystallographic analysis revealed that ligand-to-ligand interactions between the achiral L and chiral Pybox ligands successfully direct the formation of the $[Ln^{III}_4L_6]$ and $[Ln^{III}_8L_8]$ self-assemblies.

Difference types of ligand-to-ligand (π-π or CH-π) interactions are found to stimulate different anionic L arrangement around the Ln^{III} in the final $[Ln^{III}_4L_6]$ self-assemblies. In addition, interactions between tris-β-diketonate and ^{i}Pr-Pybox have also caused stereoselective formation of ($\Delta,\Delta,\Delta,\Delta,\Delta,\Delta,\Delta,\Delta$)- or ($\Lambda,\Lambda,\Lambda,\Lambda,\Lambda,\Lambda,\Lambda,\Lambda$)- [(*R*)-or (*S*)-iPr-pybox]$Ln^{III}_8L_8$ self-assemblies. All the Eu^{III} self-assemblies show consistent $[Eu^{III}_4L_6]$ structure between the solution and solid-state analysis, except for the **4-Eu^{Ph}*RRRR*/4-Eu^{Ph}*SSSS***. Ligand-to-ligand interactions should thermodynamically stabilize the polynuclear self-assemblies of $[Ln^{III}_4L_6]$ circular helicates and $[Ln^{III}_8L_8]$ square antiprism in solution.

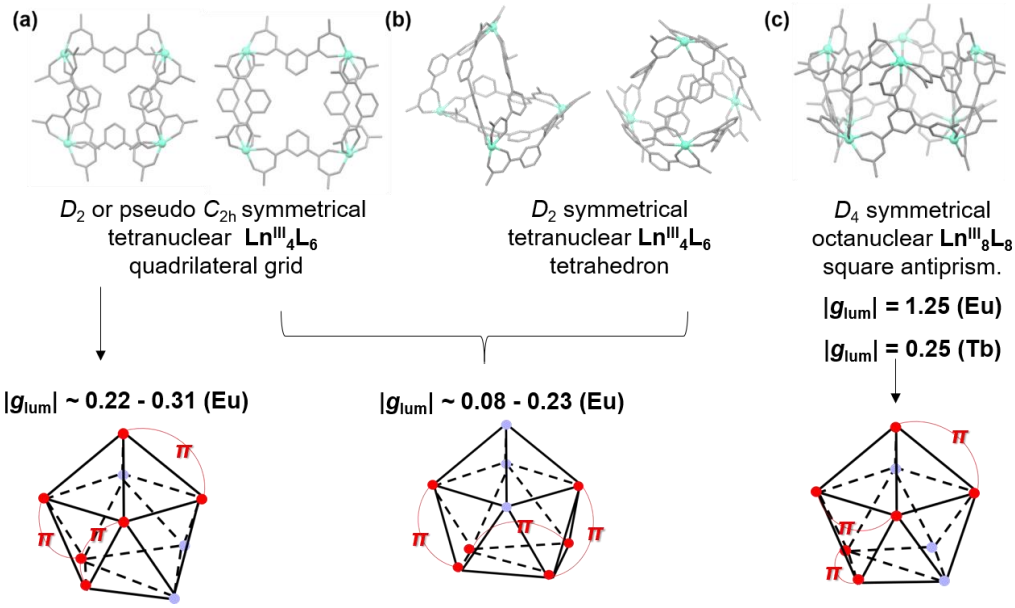

Figure 5.2. Structure, coordination geometry and luminescence dissymmetry factor of (a) $[Ln^{III}_4L_6]$ alternating circular helicates (b) $[Ln^{III}_4L_6]$ tetrahedral cage or twisted circular helicate and (c) $[Ln^{III}_8L_8]$ circular helicate.

All the Ln^{III} self-assemblies exhibit intense CPL with different observed $|g_{lum}|$ values. Eu^{III} self-assemblies possess higher $|g_{lum}|$ value than the Tb^{III} and Sm^{III} counterpart. $|g_{lum}|$ values of tetranuclear $[Eu^{III}L_6]$ are found to be in the range of 0.1 to 0.3. D_4- point symmetrical octanuclear $[Eu^{III}_8L_8]$, **5-Eu^{iPr}*RRRRRRRR*/5-Eu^{iPr}*SSSSSSSS*** achieves the highest CPL

performance among the studied self-assemblies, with a $|g_{lum}|$ value of 1.25 at the magnetic dipole $^5D_0 \rightarrow {}^7F_1$ transition. By comparing their primary coordination spheres with the other tetranuclear [$Eu^{III}{}_4L_6$] type self-assemblies, the main key of such high $|g_{lum}|$ value in **5-Eu^{iPr}*RRRRRRRR*/5-Eu^{iPr}*SSSSSSSS*** could be due to dynamic coupling involving the π- π* transition of *β*-diketonate moieties. All the Eu^{III} ions of each type of self-assemblies are nona-coordinated and exhibit distorted capped square antiprism (SAP) geometry but different helically aligned *β*-diketonate moieties in the Eu^{III} coordination spheres (Figure 5.2). These different ligands orientation should be the predominant factor affecting the magnitude of the g_{lum} value. The dynamic coupling of the helically arranged π-conjugated system of *β*-diketonate ligands in Eu coordination spheres of **5-Eu^{iPr}*RRRRRRRR*/5-Eu^{iPr}*SSSSSSSS*** (Figure 5.2c) could be close to the ideal orientation to give rise to high rotatory strength and thus large g_{lum} value. Besides, homochiral and identical helical configuration of ligands around all Eu^{III} cores of **5-Eu^{iPr}*RRRRRRRR*/5-Eu^{iPr}*SSSSSSSS*** may cooperatively contribute to significant CPL activity. Similar coordination geometry can be observed in [(*R*)- or (*S*)-iPr-pybox]Eu(D-facam)$_3$ which exhibits $|g_{lum}|$ value of 0.8-1.0.[55] Besides, Eu^{III} coordination spheres of **2-Eu^{iPr}*RRRR*/2-Eu^{iPr}*SSSS*** and **4-Eu^{iPr}*RRRR*/4-Eu^{iPr}*SSSS*** with Pybox ligand lies on the top always resulted in lower $|g_{lum}|$ values in comparison with the Eu^{III} geometries of **2-Eu^{Ph}*RRRR*/2-Eu^{Ph}*SSSS*** and **5-Eu^{iPr}*RRRRRRRR*/5-Eu^{iPr}*SSSSSSSS***, which seems to be due to the contribution of pseudo mirror symmetry and the degree of helical arranged π- π* transition of *β*-diketonate moieties to the chiroptical properties.

In conclusion, the present global complexity synthesis strategy will be promising for the rational design of self-assembled Ln^{III} showing geometrically intriguing chiral structures. Sequential reaction between Ln^{III} precursor complex with GC of x and chiral (*R*)- or (*S*)-Pybox ligands could give rise to the final chiral self-assemblies with a larger GC of 2x. However, one should give notice about the solubility of the final targeted supramolecular self-assemblies in

the ease for characterization process. Besides, structure and CPL correlation study based on the primary coordination sphere analysis suggests that the sign and magnitude of the g_{lum} in those stable polynuclear Ln^{III} system are predominantly influenced by dynamic coupling involving the π- π* transition of *β*-diketonate moieties and the number of non-distinguishable Ln^{III} ions which have similar ligand coordination mode. The Eu coordination spheres of **5-Eu^{iPr}*RRRRRRRR*/5-Eu^{iPr}*SSSSSSSS*** should be one of the ideal models for designing high g_{lum} Ln^{III} materials. Nonetheless, one should not rule out the influence of nature of ligand field to the luminescence dissymmetry.

REFERENCES

1. Symmetry. (2020, June 14). Retrieved from https://en.wikipedia.org/wiki/Symmetry
2. (a) (n.d.). Retrieved from https://www.theanimalfiles.com/glossary/bilateral_ symmetry.html (b) Mason, N. (2018, July 30). 8 examples of perfect symmetry in nature Retrieved from https://www.prolandscapermagazine.com/nature-showing-symmetry/. (c) Kirkpatrick, N. (n.d.). Everything You Need to Know About Clouds. Retrieved from https://www.mnn.com/earth-matters/climate-weather/stories/types-of-clouds (d) 2"- 4" River Rock. (2020, May 01). Retrieved from https://www. laneslandscaping.ca/product/aggregates/aggregates-2-4inch-river-rock/
3. Carter R. L. Molecular Symmetry and Group Theory. Wiley: New York, 1998.
4. Compiled by McNaught A.D.; Wilkinson.A. IUPAC. Compendium of Chemical Terminology, 2nd ed. (the "Gold Book"). Black Scientific Publications: Oxford, 1994. Chirality. (n.d.). Retrieved from https://goldbook.iupac.org/terms/view/C01058
5. Chirality. (2020, June 14). Retrieved from https://en.wikipedia.org/wiki/Chirality
6. Bruice P. Y. Organic Chemistry 6th ed. Pearson Prentice Hall: Boston, 2011.
7. Cahn R.S.; Ingold C.; Prelog V. Specification of Molecular Chirality *Angew. Chem. Int. Ed.*, **1966**, *5*, 385-415
8. (a) Hellou N.; Srebro-Hopper M.; Favereou L.; Zinna F.; Caytan E.; Toupet L.; Dorcet V.; Jean M.; Vanthuyne N.; Williams J. A. G.; Di Bari L.; Autshbach J.; Crassous J. Enantiopure Cycloiridiated Complxes Bearing a Pentahelicenic N-Heterocyclic Carbene and Displaying Long-Lived Circularly Polarized Phosphorecence. *Angew. Chem. Int. Ed.*, **2017**, *56*, 8236-8239. (b) Biet T.; Martin K.; Hankache, J.; Hellou N.; Hauser A.; Burgi T.; Vanthuyne N.; Aharon T.; Caricato M.; Crassous J.; Avarvari N. Triggering Emission with Helical Turn in Thiadiazole-Helicenes. *Chem.Eur. J.* **2017**, *23*, 437-446
9. Circular polarization. (2019, November 27). Retrieved from https://en.wikipedia.org/ wiki/Circular_polarization
10. Compiled by McNaught A.D.; Wilkinson.A. IUPAC. Compendium of Chemical Terminology, 2nd ed. (the "Gold Book"). Black Scientific Publications: Oxford, 1994. Photoluminescence. (n.d.). Retrieved from https://goldbook.iupac.org/terms/view/ P04623
11. (a) Riehl, J. P.; Muller, G. Circularly Polarised Luminescence Spectroscopy from Lanthanide Systems. In Handbook on the Physics and Chemistry of Rare Earths; Gschneidner, K. A., Bünzli, J.-C., Pecharsky, V., Eds,; North Holland Publishing Company: Amsterdam, **2004**; Vol. 34, Chapter 220, pp 289–357. (b) Luminescence of Lanthanide Ions in Coordination Compounds and Nanomaterials; Bettencourt-Dias A. de, John Wiley and Sons, Ltd: 2014.
12. (a) Lunkley, J. L.; Shirotani, D.; Yamanari, K.; Kaizaki, S.; Muller, G. Extraordinary Circularly Polarised Luminescence Activity Exhibited by Cesium Tetrakis(3-heptafluoro-butyryl-(+)-camphorato) Eu(III) Complexes in EtOH and $CHCl_3$ Solutions. *J. Am. Chem. Soc.*, **2008**, *130*, 42, 13814-13815. (b) Lunkley, J. L.; Shirotani, D.; Yamanari, K.; Kaizaki, S.; Muller, G. Chiroptical Spectra of a Tetrakis((+)-3-heptafluorobutylyrylcamphorato) lanthanide(III) with an Encapsulated Alkali Metal Ion: Circularly Polarized Luminescence

and Absolute Chiral Structures for the Eu(III) and Sm(III) Complexes. *Inorg. Chem.* **2011**, *50*, 12724-12732

13. Kumar, J.; Marydasan, B.; Nakashima, T.; Kawai, T.; Yuasa, J. Chiral Supramolecular Polymerization Leading to Eye Differentiable Circular Polarization in Luminescence. *Chem. Commun*. **2016**, *52*, 9885–9888
14. (a) Sánchez-Carnerero, E. M.; Agarrabeitia, A. R.; Moreno, F.; Maroto, B. L.; Muller, G.; Ortiz, M. J.; De La Moya, S. Circularly Polarized Luminescence from Simple Organic Molecules. *Chem. Eur. J.* **2015**, *21*, 13488-13500 (b) Kumar J.; Nakashima T.; Tsumatori H.; Kawai T. Chiral Polarized Luminescence in Chiral Aggregates: Dependence of Morphology on Luminescence Dissymmetry. *J. Phys. Chem. Lett.* **2014**, *5*, 316–321 (c) Sato S.; Yoshii. A.; Takahashi S.; Furumi S.; Takeuchi M.; Isobe H. Chiral interwined spirals and magnetic transition dipole moments dictated by cylinder helicity. *PNAS.* **2017**, *114*, 13097-13101
15. Jeong S. M.; Ohtsuka Y.; Ha N. Y.; Takanishi Y.; Ishikawa K.; Takezoe H.; Nichimura S.; Suzaki G. Highly circularly polarized electroluminescence from organic light-emitting diodes with wide-band reflective polymeric cholesteric liquid crystal films. *Appl. Phys. Lett*. **2007**, *90*, 211106
16. Yuasa, J.; Ohno, T.; Miyata, K.; Tsumatori, H.; Hasegawa, Y.; Kawai, T. Non-covalent Ligand-to-Ligand Interactions Alter Sense of Optical Chirality in Luminescent Tris(β-diketonate) Lanthanide(III) Complexes Containing a Chiral Bis(oxazolinyl) Pyridine Ligand. *J. Am. Chem. Soc.*, 2011, *133*, 9892-9902
17. Okayasu. Y.; Yuasa J. Evaluation of circularly polarized luminescence in a chiral lanthanide ensemble. *Mol. Syst. Des. Eng*. **2018**, *3*, 66-72
18. Richardson, F.; Berry, M.; Reid, M. Ligand Polarisation Contributions to Lanthanide 4*f*→4*f* Magnetic Dipole Transition Moments and Rotatory Strengths. *Molecular Physics*, **1986**, *58*, 929-945
19. (a) Di Pietro, S.; Di Bari, L. The Structure of *MLn(hfbc)*$_4$ and a Key to High Circularly Polarized Luminescence. *Inorg. Chem.* **2012**, *51*, 12007-12014. (b) Zinna, F.; Di Bari, L. Lanthanide Circularly Polarized Luminescence: Bases and Applications. *Chirality*, **2015**, *27*, 1-13
20. (a) Bruce, J.; Parker, D.; Lopinski, S.; Peacock, R. Survey of Factors Determining the Circularly Polarised Luminescence of Macrocyclic Lanthanide Complexes in Solution. *Chirality*, **2002**, *14*, 562-567. (b) Carr, R.; Evans, N.; Parker, D. Lanthanide Complexes as Chiral Probes Exploiting Circularly Polarized Luminescence. *Chem. Soc. Rev.*, 2012, **41**, 7673-7686
21. Zhang, Y. J.; Oka, T.; Suzuki, R.; Ye, J. T.; Iwasa, Y. Electrically Switchable Chiral Light-Emitting Transistor. *Science* **2014**, *344*, 725-728. (b) Zinna, F.; Giovanella, U.; Di Bari, L. Highly Circularly Polarized Electroluminescence from a Chiral Europium Complex. *Adv. Mater*. **2015**, *27*, 1791-1795
22. Montgomery, C. P.; New, E. J.; Parker, D.; Peacock, R. D. Enantioselective Regulation of a Metal Complex in Reversible Binding to Serum Albumin: Dynamic Helicity Inversion Signalled by Circularly Polarised Luminescence. *Chem. Commun.* **2008**, 4261-4263
23. Yu, J. H.; Parker, D.; Pal, R.; Poole, R. A.; Cann, M. J. A Europium Complex That Selectively Stains Nucleoli of Cells. *J. Am. Chem. Soc.* **2006**, *128*, 2294-2299

24. Montgomery, C. P.; Murray, B. S.; New, E. J.; Pal, R.; Parker, D. Cell-Penetrating Metal Complex Optical Probes: Targeted and Responsive Systems Based on Lanthanide Luminescence. *Acc. Chem. Res.* **2009**, *42*, 925-937
25. Carr, R.; Di Bari, L.; Lo Piano, S.; Parker, D.; Peacock, R. D.; Sanderson, J. M. A Chiral Probe for the Acute Phase Proteins Alpha-1-acid Glycoprotein and Alpha-1-antitrypsin based on Europium Luminescence. *Dalton Trans.* **2012**, *41*, 13154-13158
26. Smith, D. G.; Pal, R.; Parker, D. Measuring Equilibrium Bicarbonate Concentrations Directly in Cellular Mitochondria and in Human Serum Using Europium/Terbium Emission Intensity Ratios. *Chem.–Eur J.* **2012**, *18*, 11604-11613
27. Charbonnière, L. J.; Williams, A. F.; Frey, U.; Merbach, A. E.; Kamalaprija, P.; Schaad, O. A Comparison of the Lability of Molecular Octahedral and Dinuclear Triple-Helical Complexes of Cobalt(II). *J. Am. Chem. Soc*. **1997**, *119*, 2488–2496
28. Bünzli, J-C. G.; Piguet, C. Lanthanide-Containing Molecular and Supramolecular Polymetallic Functional Assemblies. *Chem. Rev.* **2002**, *102*, 6, 1897-1928
29. Barry, D. E.; Caffrey, D. F.; Gunnlaugsson, T. Lanthanide-directed synthesis of luminescent self-assembly supramolecular structure and mechanically bonded systems from acyclic coordinating organic ligands. *Chem. Soc. Rev.* **2016**, ***45***, 3244-3274
30. Floquet, S.; Ouali, N.; Bocquet, B.; Bernardinelli, G.; Imbert D.; Bünzli, J-C. G.; Hopfgartner, G.; Piguet, C. A Novel Extended Covalent Tripod for Assembling Nine-Coordinate Lanthanide(III) Podates: A Delicate Balance between Flexibility and Rigidity. *Chem. Eur. J.* **2003**, *9*, 1860-1975
31. Piguet, C.; Bernardinelli, G.; Hopfgartner, G. Helicates as Versatile Supramolecular Complexes. *Chem. Rev.*, **1997**, *97*, 6, 2005-2062
32. Aroussi, B. E.; Zebret,S.; Besnard, C.; Perrottet, P. Rational Design of a Ternary Supramolecular System: Self-Assembly of Pentanuclear Lanthanide Helicates. *J. Am. Chem. Soc.* **2011**, *133*, 10764–10767
33. Saalfrank, R. W.; Glaser, H.; Demleitner, B.; Hampel, F.; Chowdhry, M. M.; Schünemann, V.; Trautwein, A. X.; Vaughan, G. B. M.; Yeh, R.; Davis, A. V.; Raymond, K. N. Self-Assembly of Tetrahedral and Trigonal Antiprism Cluster $[Fe_6(L^4)4]$ and $[Fe_6(L^5)_6]$ on the basis of Trigonal Tris-Bidendate Chelators. *Chem. Eur. J.*, **2001**, *7*, 2770–2774
34. Saalfrank, R. W.; Maid, H.; Scheurer, A. Supramolecualr Coordination Chemistry: The Synergistic Effect of Serendipity and Rational Design. *Angew. Chem. Int. Ed.*, **2008**, *47*, 8794-8824
35. Piguet, C.; Williams, A.; Bernardinelli, G. The First Self-Assembled Dinulear Triple-Helical Lanthanide Complex: Synthesis and Structure. *Angew. Chem. Int. Ed.*, **1992**, *31*, 1622-1624.
36. Piguet, C.; Bünzli, J-C. G.; Bernardinelli, G.; Hopfgartner, G.; Williams, A. F. Self-assembly and photophysical properties of lanthanide dinuclear triple-helical complexes. *J. Am. Chem. Soc.*, **1993**, *115*, 18, 8197-8206
37. Piguet, C.; Borkovec, M.; Hamacek, J.; Zerkert, K. Strict self-assembly of polymetallic helicates:the concepts behind the semantics. *Coor. Chem. Rev.*, **2005**, *249*, 705-726
38. Bassett, A. P.; Magennis, S. W.; Glover, P. B.; Lewis, D. J.; Spencer, N.; Parsons, S.; Williams, R. M.; De Cola, L.; Pikramenou, Z. Highly Luminescent, Triple- and

Quadruple-Stranded, Dinuclear Eu, Nd, and Sm(III) Lanthanide Complexes Based on Bis-diketonate Ligands. *J. Am. Chem. Soc*. **2004**, *126*, 9413–9424

39. Mamula O.; Lama M.; Telfer S. G.; Nakamura A.; Kuroda R.; Stoeckli-Evans H.; Scopelitti R. A Trinuclear Eu^{III} Array within a Diastereoselectively Self-Assembled Helix Formed by Chiral Bipyridine-Carboxylate Ligands. *Angew. Chem., Int. Ed.*, **2005**, *44*, 2527-2531
40. Bretonniere Y.; Mazzanti M.; Wietzke R.; Pecaut J. Unpredented self-assembly of M_3L_2 trinuclear lanthanide complexes assisted by a flexible tripodal ligand containing terpyridine binding units. *Chem. Commun.*, **2000**, 1543-1544
41. Yeung, C-T.; Yim, K-H.; Wong, H-Y.; Pal, R.; Lo, W-S.; Yan, S-C.; Wong, M. Y-M.; Yufit, D.; McCormick, L. J.; Teat, S. J.; Shuh, D. K.; Wong, W-T.; Law, G. L. Chiral Transcription in Self-assembled Tetrahedral Eu_4L_6 Chiral Cages Displaying Sizable Circularly Polarized Luminescence. *Nature Communications*, **2017**, *8*:*1128*, 1-10
42. Yan, L-L.; Tan, C-H.; Zhang, G-L.; Zhou, L-P.; Bünzli, J-C. G.; Sun, Q-S. Stereocontrolled Self-Assembly and Self-Sorting of Luminescent Europium Tetrahedral Cages. *J. Am. Chem. Soc.*, **2015**, *137*, 8550-8555
43. Hamacek, J.; Bernardinelli, G.; Filinchuk, Y. Tetrahedral Assembly with Lanthanides: Toward Discrete Polynuclear Complexes. *Eur. J. Inorg. Chem.* **2008**, 3419–3422
44. Hamacek, J.; Poggiali, D.; Zebret, S.; Aroussi, B. E.; Schneider, M. W.; Mastalerz, M. Building Large Supramolecular Nanocapsules with Europium Cations. *Chem. Commun.*, **2012**, *48*, 1281–1283
45. Bretonniere Y.; Mazzanti M.; Pecaut J.; Olmstead M. M. Cation-Controlled Self-Assembly of a Hexameric Europium Wheel. *J. Am. Chem. Soc.*, **2002**, *124*, 9012-9013
46. Senegas, J.-M.; Koeller, S.; Bernardinelli, G.; Piguet, C. Isolation and Characterization of the First Circular Single-Stranded Polymetallic Lanthanide-containing Helicate. *Chem. Commun*. **2005**, 2235–2237
47. Paneerselvam, A.P.; Mishra, S.S.; Chand, D.K. Linear and circular helicates: A brief review. *J Chem Sci*, **2018**, *130:96*, 1- 18
48. Wang, B.; Zang, Z.; Wang, H.; Dou, W.; Tang, X.; Liu, W.; Shao, Y.; Ma, J.; Li, Y.; Zhou, J. Mutiple Lanthanide Helicate Clusters and the Effects of Anions on Their Configuration. *Angew. Chem. Int. Ed.*, **2013**, *52*, 3756 –3759.
49. Lu, J.; Montigaud, V.; Cador, O.; Wu, J.; Zhao, L.; Li, X-L.; Guo, M.; Guennic B. L.; Tang, J. Lanthanide(III) Hexanuclear Circular Helicates: Slow Magnetic Relaxation, Toroidal Arrangement of Magnetic Moments, and Magnetocaloric Effects. *Inorg. Chem*, **2019,** *58*, 18, 11903-11911
50. Ouellette R. J. Condensation Reactions of Carbonyl Compounds. Organic Chemistry: Elsevier: 2018; Chapter 23, pp 711-762
51. Shi. J; Hou W.; Chu W.; Shi X.; Gu H.; Wang B.; Sun Z. Crystal Structure and Highly Luminescent Properties Studies of Bis-β-diketonate Lanthanide Complexes. *Inorg. Chem.*, 2013, *52*, 5013–5022
52. Li H-F.; Yan P-F.; Chen P.; Wang Y.; Xu H.; Li G-M. Highly luminescent bis-diketonate lanthanide complexes with triple-standed dinuclear structure. *Dalton Trans.* **2012**, *41*, 900-907

53. Xu, J.; Radkov, E.; Ziegler, M.; Raymond, K.N. Plutonium(IV) Sequestration: Structural and Thermodynamic Evaluation of the Extraordinary Stable Cerium(IV) Hydroxypyridinonate Complexes. *Inorg. Chem.***, 2000**, *39*, 4156-4164
54. Harada, T.; Nakano, Y.; Fujiki, M.; Naito, M.; Kawai, T.; Hasegawa, Y. Circularly Polarized Luminescence of Eu(III) Complexes with Point- and Axial-Chiral Ligands Dependent on Coordination Structures. *Inorg. Chem.*, **2009**, *48*, 11242-11250
55. Harada, T.; Tsumatori, H.; Nishiyama, K.; Yuasa, J.; Hasegawa, Y.; Kawai, T. Nona-Coordinated Chiral Eu(III) Complexes with Stereoselective Ligand-Ligand Noncovalent Interactions for Enhanced Circularly Polarized Luminescence. *Inorg. Chem.*, **2012**, *51*, 6476-6485
56. Mosquera, J.; Ronson, T. K.; Nitshke, J. R. Subcomponent Flexibility Enables Conversion between D_4- Symmetrical $Cd^{II}_8L_8$ and *T*-symmetrical $Cd^{II}_4L_4$ Assemblies. *J. Am. Chem. Soc.*, **2016**, *138*, 6, 1812-1815
57. Bünzli, J-C. G.; Piguet, C. Taking advantage of luminescent lanthanide ions. *Chem. Soc.Rev.* **2005**, *34*, 1048-1077
58. *Telfer, S. G. et al. reported a detailed theoretical study focusing on Cotton effects in CD spectra result from excitonic couplings between the coordinated ligands, see: (*a) Telfer, S. G.; Tajima, N.; Kuroda, R.; Cantuel, M.; Piguet, C. CD Spectra of d-f Heterobimetallic Helicates with Segmental Di-Imine Ligands. *Inorg. Chem. **2004***, 43, 5302–5310. (b) Telfer, S. G.; Tajima, N.; Kuroda, R. CD Spectra of Polynuclear Complexes of Diimine Ligands: Theoretical and Experimental Evidence for the Importance of Internuclear Exciton Coupling. *J. Am. Chem. Soc., **2004***, 126, 1408–1418. (c) Telfer, S. G.; Kuroda, R.; Sato, T. Stereoselective Formation of Dinuclear Complexes with Anomalous CD Spectra. *Chem. Commun.*, **2003**, 1064–1065
59. Morcillo, S. P.; Miguel, D.; de Cienfuegos, L. Á.; Justicia, J.; Abbate, S.; Castiglioni, E.; Bour, C.; Ribagorda, M.; Cárdenas, D. J.; Paredes, J. M.; Crovetto, L.; Choquesillo-Lazarte, D.; Mota, A. J.; Carreño, M. C.; Longhi, G.; Cuerva, J. M. Stapled Helical o-OPE Foldamers as New Circularly Polarized Luminescence Emitters based on Carbophilic Interactions with Ag(I)-sensitivity. *Chem. Sci.*, **2016**, 7, 5663–5670
60. Bruhn, T.; Pescitelli, G.; Jurinovich, S.; Schaumlöffel, A.; Witterauf, F.; Ahrens, J.; Bröring, M.; Bringmann, G. Axially Chiral BODIPY DYEmers: An Apparent Exception to the Exciton Chirality Rule. *Angew. Chem., Int. Ed., **2014***, 53, 14592–14595
61. Binnemans, K. Interpretation of Europium(III) Spectra. *Coordination Chem. Reviews*, **2015**, *295*, 1-45
62. Tanner, P. A. Some Misconceptions Concerning the Electronic Spectra of Tri-positive Europium and Cerium. *Chem. Soc. Rev.*, **2013**, *42*, 5090-5101

ACKNOWLEDGEMENT

I would like to express my sincere gratitude to the following people, without whom the research works presented in this dissertation would not have been possible.

(a) My main supervisor: Prof. Tsuyoshi Kawai, for the research inspiration and guidance he has provided.

(b) My co-supervisors: Assoc. Prof. Junpei Yuasa, and Asst. Prof. Mihoko Yamada, for the research advices and supports they have given.

(c) My research supervision committees: Prof. Hisao Yanagi (Quantum Materials Science Laboratory), Assoc. Prof. Takuya Nakashima, and Assoc. Prof. Naoki Aratani (Photofunctional Organic Chemistry Laboratory), for their insightful research comments.

(d) Prof. Jeanne Crassous in University of Rennes I, for hosting me a 3 months lab-stay in her laboratory.

(e) The technical staffs: Mr Shohei Katao, Ms Yoshiko Nishikawa, Mr Fumio Asanoma, and Mr Yasuo Okajima, for their technical support in single crystal X-ray diffraction, MS, NMR spectroscopy, and emission decay analysis.

(f) Past and present members of Photonic Molecular Science Laboratory, who have created a harmonic and comfortable research environment.

(g) Yuasa's group member, who took the photograph of Figure 4.10.

(h) MEXT and NAIST-GSMS, for their scholarship and financial support awarded to me.

Finally, I would also like thank my parents and rest of my family members for their encouragement and support.

APPENDICES

APPENDIX- EXPERIMENTAL AND INSTRUMENTAL

Reagents used were purchased from Tokyo Chemical Industry (TCI) Co. Ltd. or Wako-Pure Chemical Industries Ltd and used without further purification. The chiral Pybox ligands {2,6-bis[(4*R*)-4-phenyl-2-oxazolinyl]pyridine [(*R*)-Ph-pybox], 2,6-bis[(4*S*)-4-phenyl-2-oxazolinyl] pyridine [(*S*)-Ph-pybox], 2,6-Bis[(4*R*)-(+)-isopropyl-2-oxazolinyl-2-yl]pyridine [(*R*)-^{i}Pr-pybox], and 2,6-Bis[(4*S*)-(-)-isopropyl-2-oxazolinyl-2-yl]pyridine [(*S*)-^{i}Pr-pybox]} were obtained from TCI Co. Ltd. Preparation of the bis/tris-*β*-diketonate ligands were performed under inert atmosphere at room temperature. Synthesis of the bis/tris-*β*-diketonates chelated Ln^{III} complexes ($[Ln^{III}_2L_3]$ and $[Ln^{III}_4L_4]$) and the final Ln^{III} self-assemblies ($[Ln^{III}_4L_6]$ and $[Ln^{III}_8L_8]$) were carried out under normal air condition.

Single crystal was mounted with epoxy resin on a glass fiber. X-ray diffraction intensity was collected with a Rigaku RAXIS RAPID (3 kW) imaging plate area detector with graphite monochromated Mo Ka radiation at 123 K. All calculations were performed with the Rigaku CrystalStructure 3.8.1 software.

^{1}H and ^{19}F NMR spectra were measured with JEOL JNM-ECA (600 MHz), JEOL JNM-ECP (400MHz), or JEOL JNM-ECX (400MHz). The 2D-NMR spectra of COSY, NOESY, and DOSY were measured with JEOL JNM-ECA (600 MHz). Mass spectra were measured with mass spectrometers (JEOL AccuTOF JMS-T100LC for ESI, JMS-700 MStation for EI, JEOL spiralTOF, JMS-S3000 for MALDI).

The emission and UV-vis absorption spectra were measured at room temperature using JASCO FP-6500/FP-8500 and V-660, respectively. CD spectra were measured by JASCO J-725 Spectropolarimeter. The CPL spectra were measured by our order-made CPL measurement system. g_{lum} value are determined and evaluated from the g_{lum} measurement system based on the fluorescence spectrofluorometer (JASCO FP-6500). The emission lifetimes of Eu samples were recorded using FluoroCube (HORIBA, 3000U-YSP). Emission lifetime of Tb^{III} sample was studied using a picosecond fluorescence measurement system (Hamamatsu C4780) with a streak scope (Hamamatsu C4334) The emission quantum yield (ϕ_{em}) was measured using a calibrated integrating sphere system (JASCO IL-533) in chloroform upon excitation of the ligand absorption band.

Solid state sample are prepared by incorporating the powder sample with KBr in pellet.

APPENDIX-SYNTHESIS

1.0.0 Synthesis of bis/tris-*β*-diketonate ligand

1.0.1 Synthesis of 1,3-bis(3-trifluoromethyl-3-oxopropanoyl)benzene, H_2(BTP)

H_2(BTP) ligand was prepared according to the literature[51]. The round-bottomed flask was dried, evacuated and filled up with argon gas before used. To the flask, dried THF (40 ml) was introduced. Sodium methoxide (4 ml, 0.005 M) in the methanol, ethyl trifluoroacetate (3.4 ml, 2.9 mmol) and 1,3-bis-acetophenone (1.623 g, 10.0 mmol) were added subsequently. The reaction mixture was then stirred for 24 hours. After that, the resultant mixture was poured into the ice-cold water (100ml) and acidified by hydrochloric acid (1M) to pH of 2-3. The yellow precipitate formed upon acidification was filtered and purified by recrystallization from isopropanol. Yield: 81.0 %. EI-MS (+): *m/z* 354.0 [M^+].^{1}H-NMR ($CDCl_3$, 300MHz, 298K): δ 8.50 (t, J = 1.7 Hz, 1H), 8.18 (dd, J = 7.9, 1.8 Hz, 2H), 7.70 (t, J = 7.8 Hz, 1H), 6.64 (s, 2H). ^{19}F-NMR ($CDCl_3$, 400MHz, 298K): δ -76.33 (s, 6F)

1.0.2 Synthesis of 1,3-bis(3-pentafluoroethyl-3-oxopropanoyl)benzene, H_2(BPP)

H_2(BPP) ligand was prepared as the H_2(BTP) ligand, by replacing the ethyl trifluoroacetate with ethyl pentafluoropropionate in the synthesis. The round-bottomed flask was dried, evacuated and filled up with argon gas before used. To the flask, dried THF (25 ml) was introduced. Sodium methoxide (2 ml, 0.005 M) in the methanol, ethyl pentafluoropropionate (1.6 ml, 10.8 mmol) and 1,3-bis-acetophenone (0.694 g, 4.28 mmol) were added subsequently. The reaction mixture was then stirred for 24 hours. After that, the resultant mixture was poured into the ice-cold water (100ml) and acidified by hydrochloric acid (1M) to pH of 2-3. The yellow precipitate formed upon acidification was filtered and purified by recrystallization from isopropanol. Yield: 77.6 %. EI-MS (+): *m/z* 454.03 [M^+]. ^{1}H-NMR ($CDCl_3$, 400MHz, 298K): δ 8.50 (t, J = 1.7 Hz, 1H), 8.18 (dd, 2H), 7.69 (t, J = 7.8 Hz, 1H), 6.69 (s, 2H). ^{19}F-NMR ($CDCl_3$, 400MHz, 298K): δ -82.32 (s, 3F), -123.65 (s, 2F)

1.0.3 Synthesis of 1,3-bis(3-heptafluoropropyl-3-oxopropanoyl)benzene, H_2(BHP)

H_2(BHP) ligand can be prepared as the preparation of H_2(BPP**)** ligand**,** by replacing the ethyl pentafluoropropionate with ethyl perfluorobutyrate. The round-bottomed flask was dried, evacuated and filled up with argon gas before used. To the flask, dried THF (20 ml) was introduced. Sodium methoxide (2 ml, 0.005 M) in the methanol, ethyl perfluorobutyrate (1.7 ml, 11.5 mmol) and 1,3-bis-acetophenone (0.702 g, 4.33 mmol) were added subsequently. The reaction mixture was then stirred for 24 hours. After that, the resultant mixture was poured into the ice-cold water (100ml) and acidified by hydrochloric acid (1M) to pH of 2-3. The yellow

precipitate formed upon acidification was filtered and purified by recrystallization from isopropanol. Yield: 76.8 %. EI-MS (+) *m/z* 554.02 [M^+]. ^{1}H-NMR ($CDCl_3$, 600MHz, 298K): δ 8.51 (s, 1H), 8.19 (dd, 2H), 7.70 (t, J = 7.8 Hz, 1H), 6.68 (s, 2H). ^{19}F-NMR ($CDCl_3$, 600MHz, 298K): δ -80.35 (t, J = 8.7 Hz, 6F), -121.49--121.46 (m, 4F), -126.59 (s, 4F)

1.0.4 Synthesis of 3,3-bis(3-pentafluoroethyl-3-oxopropanoyl)biphenyl, H_2(BPB)

H_2(BPB) ligand was prepared according to the synthesis of H_2(BTB), as reported in literature[52]. Non-commercially available 3,3'diacetylbiphenyl was synthesized to the process described in the literature. The round-bottomed flask was dried, evacuated and filled up with argon gas before used. To the flask, dried THF (20 ml) was introduced. Sodium methoxide (1.3 ml, 0.005 M) in the methanol, ethyl pentafluoropropionate (0.95 ml, 6.43 mmol) and 3,3'diacetylbiphenyl (0.602 g, 2.53 mmol) were added subsequently. The reaction mixture was then stirred for 24 hours. After that, the resultant mixture was poured into the ice-cold water (100ml) and acidified by hydrochloric acid (1M) to pH of 2-3. The white precipitate formed upon acidification was filtered and purified by recrystallization from acetone. Yield: 71.9 %. EI-MS (+) *m/z* 530.06. ^{1}H-NMR ($CDCl_3$, 600MHz, 298K) δ 8.18 (s, 2H), 7.98 (d, J = 7.3 Hz, 2H), 7.88 (d, J = 7.3 Hz, 2H), 7.66 (t, J = 7.8 Hz, 2H), 6.71 (s, 2H). ^{19}F-NMR ($CDCl_3$, 600MHz, 298K): δ -82.37 (s, 6F), -123.68 (s, 4F).

1.0.5 Synthesis of 1,3,5-tris(3-trifluoromethyl-3-oxopropanoyl)benzene, H_3(TTP)

The two-necked round-bottomed flask was dried, evacuated, and filled up with argon gas before used. To the flask, dried THF (25 ml) was introduced. Sodium methoxide (2 ml, 0.005 M) in the methanol, ethyl trifluoroacetate (1.7 ml, 14.00 mmol) and 1,3,5-triacetylbenzene (0.554 g, 2.71 mmol) were added subsequently. The reaction mixture was then stirred for 24 hours. After that, the resultant mixture was poured into the ice-cold water (100 ml) and acidified by hydrochloric acid (1 M) to pH of 2-3. The solution was then extracted with ethyl acetate (25 ml, 3 times), washed with water and brine solution and dried with anhydrous magnesium sulphate ($MgSO_4$). Precipitate was obtained from the evaporation of the resultant solution under reduced pressure. Recrystallisation from isopropanol gives suitable crystal for X-ray analysis. Yield: 54.7%. EI-MS (+): *m/z* = 492 [M^+]. ^{1}H-NMR ($CDCl_3$, 600 MHz, 298 K): *δ* 8.679 (s, 3H), 6.728 (s, 3H). ^{19}F-NMR ($CDCl_3$, 600 MHz, 298 K): *δ* -76.243 (s, 9F).

1.0.6 Synthesis of 1,3,5-tris(3-heptafluoropropyl-3-3-oxopropanoyl)benzene, H_3(THP)

H_3(THP) ligand was prepared as the H_3(TTP) ligand, by replacing the ethyl trifluoroacetate with ethyl perfluorobutyrate in the synthesis. The two-necked round-bottomed flask was dried, evacuated and filled up with argon gas before used. To the flask, dried THF (35 ml) was introduced. Sodium methoxide (2.4 ml, 0.005 M) in the methanol, ethyl perfluorobutyrate (2.1

ml, 12.00 mmol) and 1,3,5-triacetylbenzene (0.819 g, 4.01 mmol) were added subsequently. The reaction mixture was then stirred for 24 hours. After the completion of the reaction, the resultant mixture was poured into the ice-cold water (100 ml) and acidified by hydrochloric acid (1 M) to pH of 2-3. The yellow precipitate formed upon acidification was filtered and purified by recrystallization from isopropanol. Yield: 82.6%. EI-MS (+): *m*/*z* = 792 [M^+]. ^{1}H-NMR ($CDCl_3$, 600 MHz, 298 K): *δ* 8.677 (s, 3H), 6.751 (s, 3H). ^{19}F-NMR ($CDCl_3$, 600 MHz, 298 K): *δ* -80.32 (t, *J* = 8.7 Hz, 9F), -121.35 (q, *J* = 8.7 Hz, 6F), -126.48 (s, 6F).

1.1.0 Synthesis of bis/tris-*β*-diketonates chelated Ln^{III} complexes

1.1.1 Synthesis of [$M^{III}_2L_3$], M^{III} = Eu, Sm, Tb, Y and L = BTP, BPP, BHP

A solution of NaOH (2 eq.) in methanol (5 cm^3) was added into the solution of H_2L (1 eq.) in methanol (5 cm^3). Then, a solution of $LnCl_3.6H_2O$ (0.67 eq) in methanol (5 cm^3) was added dropwise. The reaction mixture was stirred overnight. Water was then added to induce precipitation. The precipitate formed was filtered, washed with water and dried under vacuum.

[Eu^{III}_2(BTP)$_3$]: ESI-MS (+) *m*/*z* = 1380.8812 [Eu_2(BTP)$_3$ + Na]$^+$. ^{19}F-NMR (acetone-d_6, 400MHz, 298K): δ -82.05 (s,18F)

[Tb^{III}_2(BTP)$_3$]: ESI-MS (+) *m*/*z* = 1396.8883 [Tb_2(BTP)$_3$ + Na]$^+$.

[Sm^{III}_2(BTP)$_3$]: ESI-MS (+) *m*/*z* = 1379.8779 [Sm_2(BTP)$_3$ + Na]$^+$.

[Y^{III}_2(BTP)$_3$]: ESI-MS (+) *m*/*z* = 1256.8529 [Y_2(BTP)$_3$ + Na]$^+$. ^{1}H-NMR (acetone-d_6, 400MHz, 298K): δ 8.92 (s, 3H), 8.08 (dd, J = 7.7, 1.8 Hz, 6H), 7.53 (t, J = 7.7 Hz, 3H), 6.41 (s, 6H)

[Eu^{III}_2(BPP)$_3$]: ESI-MS (+) *m*/*z* = 1682.861 [Eu_2(BPP)$_3$ + Na]$^+$, *m*/*z* = 1660.860 [Eu_2(BPP)$_3$ + H]$^+$. ^{19}F-NMR ($CDCl_3$, 400MHz, 298K): δ -84.53 (s, 6F), -85.24 (s, 12F), -126.67 (s, 4F), -128.95 (s, 8F)

[Eu^{III}_2(BHP)$_3$]: ESI-MS (+) *m*/*z* = 1982.8433 [Eu_2(BHP)$_3$ + Na]$^+$, *m*/*z* = 1960.8812 [Eu_2(BHP)$_3$ + H]$^+$. ^{19}F-NMR ($CDCl_3$, 600MHz, 298K): δ -82.33 (s, 6F), -83.07 (s, 12F), -123.53 (s, 3F), -127.30 (s, 9F), -128.13 (s, 3F), -130.17 (s, 9F)

1.1.2 Synthesis of [Eu^{III}_2(BPB)$_3$]

A solution of NaOH in ethanol (0.106 M, 7.1 cm^3) was added into the solution of H_2BPB (0.215g, 0.405 mmol) in ethanol (5 cm^3). Then, the reaction mixture was heated to dissolve the ligand completely. After cooling down the mixture to room temperature, a solution of $EuCl_3.6H_2O$ (0.092g, 0.251 mmol) in ethanol (5 cm^3) was added dropwise. The reaction mixture was stirred overnight. After that, 1ml of water was added and the reaction mixture was evaporated to dryness. The collected powder was washed with water, filtered and dried under vacuum.

[Eu^{III}_2(BPB)$_3$]: ESI-MS (+) *m*/*z* = 1953.0309 [Eu_2(BPB)$_3$ + H]$^+$. ^{19}F-NMR (acetone-d_6, 600MHz, 298K): δ -87.34 (s, 18F), -130.74 (s, 12F).

1.1.3 Synthesis of $[Ln^{III}_4L_4]$, Ln^{III} = Eu or Tb and L = TTP, THP

A solution of NaOH (2 eq.) in methanol (5 cm^3) was added into the solution of H_3L (1 eq.) in methanol (5 cm^3). Then, a solution of $LnCl_3.6H_2O$ (1 eq.) in methanol (5 cm^3) was added dropwise. The reaction mixture was stirred overnight. Water was then added to induce precipitation. The precipitate formed was filtered, washed with water and dried under vacuum.

$[Eu^{III}_4(TTP)_4]$: ESI-MS(+): *m*/*z* = 2780.729 $[Eu_4(TTP)_4(CH_3OH)_5(H_2O) + Na]^+$, *m*/*z* = 2746.787 $[Eu_4(TTP)_4(CH_3OH)_5 + Na]^+$. ^{19}F-NMR ($CDCl_3$, 600 MHz, 298 K): δ -81.493 (s, 36F). Recrystallization from the solvent pair of dimethoxyethane (DME) and hexane gives poor quality crystals of a racemic mixtures of (Δ,Δ,Δ,Δ)- and (Λ,Λ,Λ,Λ)- $[Eu_4(TTP)_4(DME)_4]$.

$[Eu^{III}_4(THP)_4]$: ESI-MS(+): *m*/*z* = 5808.413 $[Eu_6(THP)_6(CH_3OH)_5 + H]^+$, *m*/*z* = 3916.640 $[Eu_4(THP)_4(CH_3OH)_4 + Na]^+$. ^{19}F-NMR ($CD_3OD$, 600 MHz, 298K): δ -83.93 (s, 36F), -125.26 (s, 6F), -125.75 (s, 6F), -128.89 (s, 6F), -129.37 (s, 6F), -131.40 (s, 12F), -131.46 (s, 12F) ^{19}F-NMR (acetone-d_6, 600 MHz, 298K): δ -82.05, -83.54, -84.13, -85.53 (CF_3 peaks, 36F); -120.75, -121.23, -126.01, -126.48, -127.21, -127.57, -127.78, -128.05, -128.35, -129.20, -129.63, -130.10, -130.30, -130.81, -130.90, -131.20, -132.30, -132.40, -134.40, -135.83, -136.31 (CF_2 peaks, 48F). Recrystallization from the solvent pair of dimethoxyethane (DME) and hexane gives poor quality crystals of a racemic mixtures of (Δ,Δ,Δ,Δ,Δ,Δ)- and (Λ,Λ,Λ,Λ,Λ,Λ)- $[Eu_6(THP)_6(DME)_6]$.

$[Tb^{III}_4(THP)_4]$: ESI-MS(+): *m*/*z* = 5747.767029 $[Tb_6(THP)_6(OH_2)_2 + Na]^+$, *m*/*z* = 5747.767029

1.2.0 Synthesis of chiral Ln^{III} self-assemblies

1.2.1 Synthesis of $[(R)$- or (S)-Ph-Pybox$]_4(M^{III})_4(BTP)_6$ (M^{III} = Eu^{III}, Tb^{III}, Sm^{III}, Y^{III})

Under the reflux condition at 65 °C, 2,6-bis[(4*R*)-4-phenyl-2-oxazolinyl]pyridine or 2,6-bis[(4*S*)-4-phenyl-2-oxazolinyl]pyridine (0.14 mmol) was dissolved in methanol (5 mL) in the two-necked round-bottomed flask. To this solution, $[(M^{III})_2(BTP)_3]$ (0.07 mmol) in methanol solution (10 mL) was added dropwise. The reaction mixture was stirred for 1 day at 65 °C. Powder was obtained after removing the solvent by rotatory evaporator. Recrystallization from appropriate solvent pairs gives suitable crystal for X-ray analysis.

$[(R)$-Ph-Pybox$]_4(Eu^{III})_4(BTP)_6$: Yield: 74.5%. ESI-MS(+): *m*/*z* = 2101.1837 $\{[(R)$-Ph-Pybox$]_2Eu^{III}_2(BTP)_3 + H\}^+$, *m*/*z* = 2123.1788 $\{[(R)$-Ph-Pybox$]_2Eu^{III}_2(BTP)_3 + Na\}^+$. ^{19}F-NMR ($CDCl_3$, 400 MHz, 298 K): δ -79.59 (s, 12F), -84.83 (s, 12F), -87.06 (s, 12F). ^{1}H-NMR ($CDCl_3$, 600 MHz, 298 K): δ 17.8 (br, 4H), 15.9 (br, 4H), 13.6 (br, 4H), 13.1 (br, 4H), 12.4 (br, 2H), 11.7 (br, 4H), 11.6 (br, 4H), 10.9 (br, 10H), 10.5 (br, 4H), 9.78 (br, 4H), 9.41 (br, 4H), 9.23 (br, 6H), 9.12 (br, 4H), 8.52 (br, 4H), 8.42 (br, 4H), 7.58 (br, 4H), 7.35 (br, 4H), 6.27 (br, 10H), 6.19 (br, 10H), 6.07 (br, 4H), 4.68 (br, 4H), 3.70 (br, 2H), –2.14 (br, 4H), –2.38 (br, 4H).

[(*S*)-Ph-Pybox]$_4$(Eu^{III})$_4$(BTP)$_6$: Yield: 59.2%. ESI-MS(+): *m*/*z* = 4201.3528 {[(*S*)-Ph-Pybox]$_4$Eu$^{III}_4$(BTP)$_6$+ H}$^+$, *m*/*z* = 4223.2978 {[(*S*)-Ph-Pybox]$_4$Eu$^{III}_4$(BTP)$_6$+ Na}$^+$, *m*/*z* = 2101.1961 {[(*S*)-Ph-Pybox]$_2$Eu$^{III}_2$(BTP)$_3$+ H}$^+$, *m*/*z* = 2123.1724 {[(*S*)-Ph-Pybox]$_2$Eu$^{III}_2$(BTP)$_3$+ Na}$^+$

[(*R*)-Ph-Pybox]$_4$(Tb^{III})$_4$(BTP)$_6$: Yield: 80.8%. ESI-MS(+): *m*/*z* = 4225.8439 {[(*R*)-Ph-Pybox]$_4$Tb$^{III}_4$(BTP)$_6$+ H}$^+$, *m*/*z* = 4246.7907 {[(*R*)-Ph-Pybox]$_4$Tb$^{III}_4$(BTP)$_6$+ Na}$^+$, *m*/*z* = 2113.2023 {[(*R*)-Ph-Pybox]$_2$Tb$^{III}_2$(BTP)$_3$+ H}$^+$, *m*/*z* = 2135.2140 {[(*R*)-Ph-Pybox]$_2$Tb$^{III}_2$(BTP)$_3$+ Na}$^+$

[(*S*)-Ph-Pybox]$_4$(Tb^{III})$_4$(BTP)$_6$: Yield: 69.2%. ESI-MS(+): *m*/*z* = 4225.7845 {[(*S*)-Ph-Pybox]$_4$Tb$^{III}_4$(BTP)$_6$+ H}$^+$, *m*/*z* = 4247.3842 {[(*S*)-Ph-Pybox]$_4$Tb$^{III}_4$(BTP)$_6$+ Na}$^+$, *m*/*z* = 2113.1741 {[(*S*)-Ph-Pybox]$_2$Tb$^{III}_2$(BTP)$_3$+ H}$^+$, *m*/*z* = 2135.1587 {[(*S*)-Ph-Pybox]$_2$Tb$^{III}_2$(BTP)$_3$+ Na}$^+$

[(*R*)-Ph-Pybox]$_4$(Sm^{III})$_4$(BTP)$_6$: Yield: 72.3%. ESI-MS(+): *m*/*z* = 2097.1220 {[(*R*)-Ph-Pybox]$_2$Sm$^{III}_2$(BTP)$_3$+ H}$^+$, *m*/*z* = 2121.1390 {[(*R*)-Ph-Pybox]$_2$Sm$^{III}_2$(BTP)$_3$+ Na}$^+$

[(*S*)-Ph-Pybox]$_4$(Sm^{III})$_4$(BTP)$_6$: Yield: 73.2%. ESI-MS(+): *m*/*z* = 2097.1249 {[(*S*)-Ph-Pybox]$_2$Sm$^{III}_2$(BTP)$_3$+ H}$^+$, *m*/*z* = 2121.1635 {[(*S*)-Ph-Pybox]$_2$Sm$^{III}_2$(BTP)$_3$+ Na}$^+$

[(*R*)-Ph-Pybox]$_4$(Y^{III})$_4$(BTP)$_6$: Yield: 70.1%. ^{19}F-NMR ($CDCl_3$, 400 MHz, 298 K): *δ* -75.20 (s, 12F), -75.50 (s, 11F), -76.05 (s, 12F). ^{1}H-NMR ($CDCl_3$, 600 MHz, 298 K): *δ* 8.31 (t, *J* = 8.4 Hz, 4H), 8.27 (d, 4H), 8.16 (d, *J* = 6.6 Hz, 4H), 8.04 (d, *J* = 7.8 Hz, 4H), 7.65 (d, *J* = 7.2 Hz, 4H), 7.59 (s, 4H), 7.38 (s, 2H), 7.25 (br, 8H), 7.20 (d, *J* = 6.6 Hz, 4H), 7.15 (t, *J* = 6.6 Hz, 8H), 7.03 (t, *J* = 7.2 Hz, 4H), 6.91 (m, 4H), 6.87 (t, *J* = 6.6 Hz, 4H), 6.79 (m, 16H), 6.60 (t, *J* = 7.2 Hz, 2H), 6.49 (s, 4H), 5.84 (s, 4H), 5.66 (s, 4H), 5.47 (t, *J* = 10.2 Hz, 4H), 5.16 (t, *J* = 10.2 Hz, 4H), 5.11 (dd, *J* = 10.2 Hz, 7.2 Hz, 4H), 4.79 (t, *J* = 10.2 Hz, 4H), 4.52 (t, *J* = 9.6 Hz, 4H), 4.37 (dd, *J* = 9.0 Hz, 6.6 Hz, 4H).

1.2.2 Synthesis of [(*R*)- or (*S*)-Ph-Pybox]$_4$(Eu^{III})$_4$(L)$_6$, L= BPP, BHP

Under the reflux condition at 65 °C, 2,6-bis[(4*R*)-4-phenyl-2-oxazolinyl]pyridine or 2,6-bis[(4*S*)-4-phenyl-2-oxazolinyl]pyridine (0.060 mmol) was dissolved in methanol (5 mL) in the two-necked round-bottomed flask. To this solution, [(Eu^{III})$_2$(L)$_3$] (0.030 mmol) in methanol solution (5 mL) was added dropwise. The reaction mixture was stirred for 1 day at 65 °C. Powder was obtained after removing the solvent by rotatory evaporator. Recrystallization from ethyl acetate/hexane gives suitable crystal for X-ray analysis.

[(*R*)-Ph-Pybox]$_4$Eu$^{III}_4$(BPP)$_6$: Yield: 41.7%. ESI-MS(+): *m*/*z* = 4821.315 {[(*R*)-Ph-Pybox]$_4$Eu$^{III}_4$(BPP)$_6$ + Na}$^+$, *m*/*z* = 4799.782 {[(*R*)-Ph-Pybox]$_4$Eu$^{III}_4$(BPP)$_6$+ H}$^+$. ^{19}F-NMR ($CDCl_3$, 400MHz, 298K): -83.87(s, 12F), -86.01(s, 12F), -88.49(s, 12F), -124.21, -124.98, -126.27, -126.93, -129.89, -130.41, -130.68, -131.18, -132.46, -133.34, -140.99, -141.60. ^{19}F-NMR (Toluene-d8, 600MHz, 298K): δ -83.57(s, 12F), -85.90(s, 12F), -87.96(s, 12F), -124.12,

-124.60, -125.42, -125.90, -129.54, -129.72, -130.02, -130.20, -132.50, -132.98, -139.76, -140.33.

[(*S*)-Ph-Pybox]$_4$Eu$^{III}_4$(BPP)$_6$: Yield: 57.8%. ESI-MS(+): *m*/*z* = 4821.945 {[(*S*)-Ph-Pybox]$_4$(Eu^{III})$_4$(BPP)$_6$ + Na}$^+$, *m*/*z* = 4799.888 {[(*S*)-Ph-Pybox]$_4$Eu$^{III}_4$(BPP)$_6$ + H}$^+$.

[(*R*)-Ph-Pybox]$_4$Eu$^{III}_4$(BHP)$_6$: Yield: 40.7%. ESI-MS(+): *m*/*z* = 5422.276 {[(*R*)-Ph-Pybox]$_4$Eu$^{III}_4$(BHP)$_6$ + Na}$^+$, *m*/*z* = 5399.639 {[(*R*)-Ph-Pybox]$_4$Eu$^{III}_4$(BHP)$_6$+ H}$^+$. ^{19}F-NMR ($CDCl_3$, 400MHz, 298K): -81.20(s, 12F), -81.91(s, 12F), -85.14(s, 12F), -122.13, -122.81, -124.07, -124.61, -124.79, -125.35, -126.16, -126.95, -127.42, -128.00, -128.20, -128.75, -130.91, -131.66, -132.76, -133.52, -133.90, -134.71, -138.99, -139.71. ^{19}F-NMR (Toluene-d8, 600MHz, 298K): δ -81.09(s, 12F), -81.81(s, 12F), -84.87(s, 12F), -121.78, -122.29, -123.27, -123.76, -126.27, -126.77, -127.10, -127.56, -130.27, -130.77, -130.90, -131.23, -131.42, -131.73, -132.18, -132.68, -133.41, -133.91, -138.07, -138.56.

[(*S*)-Ph-Pybox]$_4$Eu$^{III}_4$BHP$_6$: Yield: 44.4%. ESI-MS(+): *m*/*z* = 5422.296 {[(*S*)-Ph-Pybox]$_4$(Eu^{III})$_4$(BHP)$_6$ + Na}$^+$, *m*/*z* = 5399.953 {[(*S*)-Ph-Pybox]$_4$Eu$^{III}_4$(BHP)$_6$ + H}$^+$.

1.2.3 Synthesis of [(*R*)- or (*S*)-^{i}Pr-Pybox]$_4$(Eu^{III})$_4$(BPP)$_6$

Under the reflux condition at 65 °C, 2,6-bis[(4*R*)-(+)-isopropyl-2-oxazolin-2-yl]pyridine or 2,6-bis[(4*S*)-(-)-isopropyl-2-oxazolin-2-yl]pyridine (0.060 mmol) was dissolved in methanol (5 mL) in the two-necked round-bottomed flask. To this solution, [(Eu^{III})$_2$(BPP)$_3$] (0.030 mmol) in methanol solution (5 mL) was added dropwise. The reaction mixture was stirred for 1 day at 65 °C. Powder was obtained after removing the solvent by rotatory evaporator. Recrystallization from acetone/pentane gives suitable crystal for X-ray analysis.

[(*R*)-^{i}Pr-Pybox]$_4$Eu$^{III}_4$BPP$_6$: Yield: 36.8 %. ESI-MS (+): *m*/*z* = 4549.662 {[(*R*)-^{i}Pr-Pybox]$_4$Eu$^{III}_4$(BPP)$_6$ + Na}$^+$, *m*/*z* = 4527.834 {[(*R*)-^{i}Pr-Pybox]$_4$Eu$^{III}_4$(BPP)$_6$+ H}$^+$. ^{19}F-NMR ($CDCl_3$, 600MHz, 298K): δ -89.08--82.99, -142.07--122.93. ^{19}F-NMR (Toluene-d_8, 600MHz, 298K δ -82.66(s, 12F), -83.70(s, 12F), -88.76(s, 12F), 123.20, -123.68, -124.03, -124.50, -125.25, -125.72, -132.86, -133.34, -136.26, -136.48, -136.73, -136.97.

[(*S*)-^{i}Pr-Pybox]$_4$Eu$^{III}_4$BPP$_6$: Yield: 55.1 %. ESI-MS (+): *m*/*z* = 4549.675 {[(*R*)-^{i}Pr-Pybox]$_4$Eu$^{III}_4$(BPP)$_6$ + Na}$^+$, *m*/*z* = 4527.742 {[(*R*)-^{i}Pr-Pybox]$_4$Eu$^{III}_4$(BPP)$_6$+ H}$^+$.

1.2.4 Synthesis of [(*R*)- or (*S*)-Ph-Pybox]$_4$(Eu^{III})$_4$(BPB)$_6$

Under the reflux condition at 65 °C, 22,6-bis[(4*R*)-(+)-isopropyl-2-oxazolin-2-yl]pyridine or 2,6-bis[(4*S*)-(-)-isopropyl-2-oxazolin-2-yl]pyridine (0.046 mmol) was dissolved in methanol (5 mL) in the two-necked round-bottomed flask. To this solution, [Eu$^{III}_2$(BPB)$_3$] (0.023 mmol) in methanol solution (5 mL) was added dropwise. The reaction mixture was stirred for 1 day at 65 °C. Powder was obtained after removing the solvent by rotatory evaporator. Crystal can be recrystallized from toluene/hexane.

[(*R*)-Ph-Pybox]$_4$(Eu^{III})$_4$(BPB)$_6$: Yield: 46.7%. ESI-MS (+): *m*/*z* = 5278.3065 {[(*R*)-Ph-Pybox]$_4$(Eu^{III})$_4$(BPB)$_6$+Na}$^+$, *m*/*z* = 2258.0979 {[(*R*)-Ph-Pybox]$_1$(Eu^{III})$_2$(BPB)$_3$+H}$^+$, *m*/*z* = 1910.9413 [(Eu^{III})$_2$(BPB)$_3$+Na]$^+$.

[(*S*)-Ph-Pybox]$_4$(Eu^{III})$_4$(BPB)$_6$: Yield: 49.2%. ESI-MS (+): *m*/*z* = 2258.1644 {[(*R*)-Ph-Pybox]$_1$(Eu^{III})$_2$(BPB)$_3$+H}$^+$, *m*/*z* = 1910.9670 [(Eu^{III})$_2$(BPB)$_3$+Na]$^+$.

1.2.5 Synthesis of [(*R*)- or (*S*)-^{i}Pr-Pybox]$_4$(Eu^{III})$_4$(BPB)$_6$

Under the reflux condition at 65 °C, 2,6-bis[(4*R*)-4-phenyl-2-oxazolinyl]pyridine or 2,6-bis[(4*S*)-4-phenyl-2-oxazolinyl]pyridine (0.050 mmol) was dissolved in methanol (5 mL) in the two-necked round-bottomed flask. To this solution, [Eu$^{III}_2$(BPB)$_3$] (0.025 mmol) in methanol solution (5 mL) was added dropwise. The reaction mixture was stirred for 1 day at 65 °C. Powder was obtained after removing the solvent by rotatory evaporator. Recrystallization from toluene/hexane gives suitable crystal for X-ray analysis.

[(*R*)-^{i}Pr-Pybox]$_4$(Eu^{III})$_4$(BPB)$_6$: Yield: 59.8%. ESI-MS(+): *m*/*z* = 4984.0185 {[(*R*)-^{i}Pr-Pybox]$_4$(Eu^{III})$_4$(BPB)$_6$+ H}$^+$, *m*/*z* = 2491.3483 {[(*R*)-^{i}Pr-Pybox]$_2$(Eu^{III})$_2$(BPB)$_3$+ H}$^+$. ^{19}F-NMR ($CDCl_3$, 600 MHz, 298 K): δ-84.72 (s, 12F), -85.02 (s, 13F), -86.51 (s, 12F), -117.46 (s, 2F), -117.94 (s, 2F), -125.35 (s, 2F), -125.82 (s, 2F), -129.09 (s, 2F), -129.58 (s, 2F), -132.66 (s, 2F), -133.14 (s, 2F), -133.73 (s, 2F), -134.21 (s, 2F), -136.35 (s, 2F), -136.83 (s, 2F).

[(*S*)-^{i}Pr-Pybox]$_4$(Eu^{III})$_4$(BPB)$_6$: Yield: 64.8 %. ESI-MS (+): *m*/*z* = 4985.6363 {[(*R*)-^{i}Pr-Pybox]$_4$(Eu^{III})$_4$(BPB)$_6$+ H}$^+$, *m*/*z* = 2491.3952 {[(*R*)-^{i}Pr-Pybox]$_2$(Eu^{III})$_2$(BPB)$_3$+ H}$^+$

1.2.6 Synthesis of (Δ,Δ,Δ,Δ,Δ,Δ,Δ,Δ)-[(*R*)-^{i}Pr-pybox]$_8$(Ln^{III})$_8$(THP)$_8$ or (Λ,Λ,Λ,Λ,Λ,Λ,Λ,Λ)-[(*S*)-^{i}Pr-pybox]$_8$(Ln^{III})$_8$(THP)$_8$, Ln =Eu, Tb

Under the reflux condition, [Ln$^{III}_4$(THP)$_4$] (0.0085 mmol) in methanol (5 ml) was dissolved in a two-necked flask. To this solution, 2,6-Bis[(4*R*)-(+)-isopropyl-2-oxazolin-2-yl]pyridine, (*R*)-^{i}Pr-pybox or 2,6-Bis[(4*S*)-(-)-isopropyl-2-oxazolin-2-yl]pyridine, (*S*)-^{i}Pr-pybox (0.015 g, 0.050 mmol) in methanol (5 ml) was added dropwise. The reaction mixture was stirred overnight at 65°C. Powder are obtained after removing the solvent by rotatory evaporator. Recrystallization from the solvent pair of chloroform and toluene gives suitable crystals for X-ray analysis.

(Δ,Δ,Δ,Δ,Δ,Δ,Δ,Δ)-[(*R*)-^{i}Pr-pybox]$_8$(Eu^{III})$_8$(THP)$_8$ Yield: 50.3%. ESI-MS(+): *m*/*z* = 9662.578 {[(*R*)-^{i}Pr-pybox)]$_7$Eu$_8$(THP)$_8$ + Na}$^+$ MALDI-MS: *m*/*z* = 9715.370 {[(*R*)-^{i}Pr-pybox)]$_7$Eu$_8$(THP)$(OH_2)_3$ + Na}$^+$, *m*/*z* = 7853.960 {[(*R*)-^{i}Pr-pybox)]Eu$_8$(THP)$_8$ + Na}$^+$. ^{19}F-NMR ($CDCl_3$, 600 MHz, 298 K): δ -81.65 (s, 24F), -84.58 (s, 24F), -84.88 (s, 24F), -117.16 (s, 4F), -117.65 (s, 4F), -120.18 (s, 4F), -120.66 (s, 4F), -124.10 (s, 4F), -124.59 (s, 4F), -128.58 (s, 16F), -130.14 (s, 4F), -130.57 (s, 4F), -131.48 (s, 4F), -131.99 (s, 4F), -133.82 (s, 4F), -134.19 (s, 1F), -134.34 (s, 3F), -134.69 (s, 6F), -135.23 (s, 4F), -135.42 (s, 3F), -135.74 (s, 1F), -135.89 (s, 2F), -137.81 (s, 4F), -138.28 (s, 4F)

(Λ,Λ,Λ,Λ,Λ,Λ,Λ,Λ)-[(*S*)-^{i}Pr-pybox]$_8$(Eu^{III})$_8$(THP)$_8$ Yield: 64.5%. ESI-MS(+): *m*/*z* = 9489.036 {[(*S*)-^{i}Pr-pybox)]$_6$Eu$_8$(THP)$_8$(CH$_3$OH)$_4$ + Na}$^+$ MALDI-MS: *m*/*z* = 9715.475 {[(*S*)-^{i}Pr-pybox)]$_7$Eu$_8$(THP)$_8$(OH$_2$)$_3$ + Na}$^+$, *m*/*z* = 7854.664 {[(*S*)-^{i}Pr-pybox)]Eu$_8$(THP)$_8$ + Na}$^+$. ^{19}F-NMR (CDCl$_3$, 600 MHz, 298K): *δ* -81.64 (s, 24F), -84.58 (s, 24F), -84.88 (s, 24F), -117.20 (s, 4F), -117.63 (s, 4F), -120.17 (s, 4F), -120.66 (s, 4F), -124.09 (s, 4F), -124.58 (s, 4F), -128.59 (s, 16F), -129.98 (s, 4F), -130.53 (s, 4F), -131.47 (s, 4F), -131.93 (s, 4F), -133.84 (s, 4F), -134.35 (s, 1F), -134.70 (s, 3F), -134.90 (s, 6F), -135.22 (s, 4F), -135.42 (s, 3F), -135.76 (s, 1F), -135.89 (s, 2F), -137.74 (s, 4F), -138.30 (s, 4F)

(Δ,Δ,Δ,Δ,Δ,Δ,Δ,Δ)-[(*R*)-^{i}Pr-pybox]$_8$(Tb^{III})$_8$(THP)$_8$ Yield: 54.6%. ESI-MS(+): *m*/*z* = 9717.919 {[(*R*)-^{i}Pr-pybox)]$_7$Tb$_8$(THP)$_8$ + Na}$^+$ MALDI-MS: *m*/*z* = 9419.541 {[(*R*)-^{i}Pr-pybox)]$_6$Tb$_8$(THP)$_8$ + Na}$^+$, *m*/*z* = 7717.764 {Tb$_8$(THP)$_8$(OH$_2$)(C$_7$H$_8$) +Na}$^+$.

(Λ,Λ,Λ,Λ,Λ,Λ,Λ,Λ)-[(*S*)-^{i}Pr-pybox]$_8$(Tb^{III})$_8$(THP)$_8$ Yield: 52.4%. ESI-MS(+): *m*/*z* = 9717.803 {[(*S*)-^{i}Pr-pybox)]$_7$Tb$_8$(THP)$_8$ + Na}$^+$, MALDI-MS: *m*/*z* = 9419.547 {[(*S*)-^{i}Pr-pybox)]$_6$Tb$_8$(THP)$_8$ + Na}$^+$, *m*/*z* = 7717.743{Tb$_8$(THP)$_8$(OH$_2$)(C$_7$H$_8$) + Na}$^+$.

APPENDIX-CRYSTALLOGRAPHIC DATA

Table A1. Crystallographic parameters and refinement details for H_2BPP, H_2BHP, H_2BPB, and H_3THP

	H_2BPP	**H_2BHP**	**H_2BPB**	**H_3THP**
formula sum	$C_{16}H_8F_{10}O_4$	$C_{18}H_8F_{14}O_4$	$C_{22}H_{12}F_{10}O_4$	$C_{24}H_9F_{21}O_6$
formula weight	454.22	554.24	530.06	792.30
crystal system	Monoclinic	Monoclinic	Triclinic	Triclinic
Space group	C2/c	$P2_1/n$	P-1	P-1
a (Å)	18.1798	5.1654	4.93175	5.0938
b (Å)	10.9943	31.843	9.3345	14.6539
c (Å)	9.29667	12.0412	11.4297	18.6644
α (deg)	90.000	90.000	106.824	80.974
β (deg)	118.606	90.444	92.101	89.293
γ (deg)	90.000	90.000	91.704	82.793
V (Å^3)	1631.34	1980.5	502.87	1365.04
T (K)	103	103	123	123
Z	4	4	1	2
ρ calcd (g cm^{-3})	1.849	1.859	1.751	1.927
R1 [I > 2σ(I]]	0.0297	0.0474	0.0402	0.0579
wR2 [I > 2σ(I]]	0.0810	0.1426	0.1066	0.1598

Table A2. Crystallographic parameters and refinement details for $(Eu^{III})_2(BTP)_3(DME)_2$, $Eu^{III}_2(BPP)_3(DME)_2$, and $Eu^{III}_2(BHP)_3(DME)_2$

	$(Eu^{III})_2(BTP)_3(DME)_2$	**$Eu^{III}_2(BPP)_3(DME)_2$**	**$Eu^{III}_2(BHP)_3(DME)_2$**
formula sum	$Eu_2C_{50}H_{38}F_{18}O_{16}$	$Eu_2C_{56}H_{38}F_{30}O_{16}$	$Eu_2C_{66}H_{48}F_{42}O_{18}$
formula weight	1540.73	1840.78	2230.95
crystal system	Monoclinic	Monoclinic	Triclinic
space group	C2/c	C2/c	P-1
a (Å)	15.2207	15.3552	14.2319
b (Å)	12.9148	13.0069	14.6279
c (Å)	28.6104	32.4509	19.8264
α (deg)	90.000	90.000	83.457
β (deg)	90.782	92.424	87.082
γ (deg)	90.000	90.000	89.971
V (Å^3)	5623.47	6475.4	4095.26
T (K)	123.15	123	123
Z	4	4	2
ρ calcd (g cm^{-3})	1.820	1.888	1.809
R1 [I > 2σ(I)]	0.0185	0.0288	0.0264
wR2 [I > 2σ(I)]	0.0463	0.0835	0.0682

Table A3. Crystallographic parameters and refinement details for $Eu^{III}_4(TPP)_4(bipy)_4(MEK)_2(OH_2)_2$, $Eu^{III}_4(THP)_4(bipy)_4$, and (Λ,Λ,Λ,Λ,Λ,Λ)-$[Eu^{III}_6(THP)_8]^{6-}.4Na^+.6OH_2$.

	$Eu^{III}_4(TPP)_4(bipy)_4(MEK)_2(OH_2)_2$	**$Eu^{III}_4(THP)_4(bipy)_4$**	**(Λ,Λ,Λ,Λ,Λ,Λ)-$[Eu^{III}_6(THP)_8]^{6-}.4Na^+.6OH_2$**
formula sum	$Eu_4C_{120}H_{76}F_{36}N_8O_{28}$	$Eu_4C_{136}H_{56}F_{84}N_8O_{24}$	$Eu_6C_{144}H_{48}F_{72}O_{55}Na_4$
formula weight	3369.75	4389.70	5029.53
crystal system	tetragonal	Triclinic	Monoclinic
space group	P-4c2	P-1	C2
a (Å)	27.0056	20.3217	37.8422
b (Å)	27.0056	21.4128	37.7953
c (Å)	20.3637	24.1786	19.8443
α (deg)	90	75.276	90
β (deg)	90	71.953	97.933
γ (deg)	90	64.363	90
V (Å^3)	14851.3	8929.7	28110.9
T (K)	123	123	123
Z	4	2	4
ρ calcd (g cm^{-3})	1.636	1.767	1.188
R1 [I > 2σ(I)]	0.0256	0.0602	0.0708
wR2 [I > 2σ(I)]	0.0603	0.1694	0.1839

Table A4. Crystallographic parameters and refinement details for [(*R*)-Ph-Pybox]$_4$Eu$^{III}_4$(BTP)$_6$ (**1-Eu^{Ph}*RRRR***), [(*S*)-Ph-Pybox]$_4$Eu$^{III}_4$(BTP)$_6$ (**1-Eu^{Ph}*SSSS***), and racemic mixture of **1-Eu^{Ph}*RRRR*/1-Eu^{Ph}*SSSS***.

	1-Eu^{Ph}*RRRR*	**1-Eu^{Ph}*SSSS***	**1-Eu^{Ph}*RRRR* and 1-Eu^{Ph}*SSSS***
formula sum	$Eu_4C_{176}H_{112}F_{36}N_{12}O_{32}$	$Eu_4C_{176}H_{112}F_{36}N_{12}O_{32}$	$Eu_4C_{176}H_{112}F_{36}N_{12}O_{32}$
formula weight	4200.38	4200.38	4200.38
crystal system	Monoclinic	Monoclinic	Monoclinic
space group	C2	C2	C2/c
a (Å)	25.7603	25.7797	34.96910
b (Å)	35.0350	34.9694	31.24155
c (Å)	12.4435	12.4506	24.90153
α (deg)	90.000	90.000	90.000
β (deg)	101.626	101.770	117.60500
γ (deg)	90.000	90.000	90.000
V (Å^3)	11000.0	10988.3	24107.75288
T (K)	123.15	123.15	123.15
Z	2	2	4
ρ calcd (g cm^{-3})	1.312	1.336	1.152
R1 [I > 2σ(I)]	0.0221	0.0205	0.0554
wR2 [I > 2σ(I)]	0.0500	0.0514	0.1480

Table A5. Crystallographic parameters and refinement details for [(*R*)-Ph-Pybox]$_4$Y$^{III}_4$(BTP)$_6$ (**1-Y^{Ph}*RRRR***), [(*R*)-Ph-Pybox]$_4$Sm$^{III}_4$(BTP)$_6$ (**1-Sm^{Ph}*RRRR***), and [(*S*)-Ph-Pybox]$_4$Sm$^{III}_4$(BTP)$_6$ (**1-Sm^{Ph}*SSSS***).

	1-Y^{Ph}*RRRR*	**1-Sm^{Ph}*RRRR***	**1-Sm^{Ph}*SSSS***
formula sum	$Y_4C_{176}H_{112}F_{36}N_{12}O_{32}$	$Sm_4C_{176}H_{112}F_{36}N_{12}O_{32}$	$Sm_4C_{176}H_{112}F_{36}N_{12}O_{32}$
formula weight	3944.3165	4340.67	4340.67
crystal system	Monoclinic	Monoclinic	Monoclinic
space group	C2	C2	C2
a (Å)	33.7309	25.7590	25.5689
b (Å)	32.1542	35.1455	35.2088
c (Å)	22.2394	12.4630	12.4439
α (deg)	90.000	90.000	90.000
β (deg)	101.685	102.001	101.736
γ (deg)	90.000	90.000	90.000
V (Å^3)	23650.8	11036.3	10968.4
T (K)	123.15	123.15	123.15
Z	4	2	2
ρ calcd (g cm^{-3})	1.201	1.306	1.314
R1 [I > 2σ(I)]	0.0512	0.0252	0.0225
wR2 [I > 2σ(I)]	0.1197	0.0538	0.0530

Table A6. Crystallographic parameters and refinement details for [(*R*)-Ph-Pybox]$_4$Tb$^{III}_4$(BTP)$_6$ (**1-Tb^{Ph}*RRRR***), [(*S*)-Ph-Pybox]$_4$Tb$^{III}_4$(BTP)$_6$ (**1-Tb^{Ph}*SSSS***), and [(*R*)-Ph-Pybox]$_4$Eu$^{III}_4$(BPP)$_6$ (**2-Eu^{Ph}*RRRR***).

	1-Tb^{Ph}*RRRR*	**1-Tb^{Ph}*SSSS***	**2-Eu^{Ph}*RRRR***
formula sum	$Tb_4C_{176}H_{112}F_{36}N_{12}O_{32}$	$Tb_4C_{176}H_{112}F_{36}N_{12}O_{32}$	$Eu_4C_{188}H_{112}F_{60}N_{12}O_{32}$
formula weight	4224.39	4224.39	4800.34
crystal system	monoclinic	monoclinic	Tetragonal
space group	C2	C2	$P4_322$
a (Å)	33.9749	25.5303	23.4712
b (Å)	31.8951	35.1251	23.4712
c (Å)	22.5994	12.3994	50.4764
α (deg)	90.000	90.000	90.000
β (deg)	102.326	101.829	90.000
γ (deg)	90.000	90.000	90.000
V (Å^3)	23924.9	10883.1	27807.3
T (K)	123.15	123.15	123.15
Z	4	2	4
ρ calcd (g cm^{-3})	1.173	1.335	1.146
R1 [I > 2σ(I)]	0.0350	0.0244	0.0307
wR2 [I > 2σ(I)]	0.0711	0.0558	0.0885

Table A7. Crystallographic parameters and refinement details for [(*S*)-Ph-Pybox]$_4$Eu$^{III}_4$(BPP)$_6$ (**2-Eu^{Ph}*SSSS***), [(*R*)-^{i}Pr-Pybox]$_4$Tb$^{III}_4$(BTP)$_6$ (**2-Eu^{iPr}*RRRR***), and [(*S*)-^{i}Pr-Pybox]$_4$Tb$^{III}_4$(BTP)$_6$ (**2-Eu^{iPr}*SSSS***).

	2-Eu^{Ph}*SSSS*	**2-Eu^{iPr}*RRRR***	**2-Eu^{iPr}*SSSS***
formula sum	$Eu_4C_{188}H_{112}F_{60}N_{12}O_{32}$	$Eu_4C_{164}H_{128}F_{60}N_{12}O_{32}$	$Eu_4C_{164}H_{128}F_{60}N_{12}O_{32}$
formula weight	4800.34	4528.46	4528.46
crystal system	Tetragonal	Monoclinic	Monoclinic
space group	$P4_122$	$P2_1$	$P2_1$
a (Å)	23.5055	19.5403	19.5604
b (Å)	23.5055	25.7217	25.7392
c (Å)	49.8319	21.0558	21.0306
α (deg)	90.000	90.000	90.000
β (deg)	90.000	110.290	110.270
γ (deg)	90.000	90.000	90.000
V (Å^3)	27532.5	9926.2	9932.5
T (K)	123.15	123.15	123.15
Z	4	2	2
ρ calcd (g cm^{-3})	1.202	1.569	1.571
R1 [I > 2σ(I)]	0.0403	0.0339	0.0537
wR2 [I > 2σ(I)]	0.1126	0.0850	0.1505

Table A8. Crystallographic parameters and refinement details for [(*R*)-Ph-Pybox]$_4$Eu$^{III}_4$(BPB)$_6$ (**4-Eu^{Ph}*RRRR***), [(*S*)-Ph-Pybox]$_4$Eu$^{III}_4$(BPB)$_6$ (**4-Eu^{Ph}*SSSS***), and [(*R*)-Ph-Pybox]$_4$Y$^{III}_4$(BPB)$_6$ (**4-Y^{Ph}*RRRR***).

	4-Eu^{Ph}*RRRR*	**4-Eu^{Ph}*SSSS***	**4-Y^{Ph}*RRRR***
formula sum	$Eu_4C_{224}H_{136}F_{60}N_{12}O_{32}$	$Eu_4C_{224}H_{136}F_{60}N_{12}O_{32}$	$Y_4C_{224}H_{136}F_{60}N_{12}O_{32}$
formula weight	5256.53	5256.53	5000.47
crystal system	monoclinic	Orthorhombic	monoclinic
space group	C2	$P2_12_12$	C2
a (Å)	35.3525	30.0176	35.2610
b (Å)	18.6848	18.7836	18.5579
c (Å)	20.3515	20.2816	20.2992
α (deg)	90.000	90.000	90.000
β (deg)	121.026	90.000	120.970
γ (deg)	90.000	90.000	90.000
V (Å^3)	11519.9	11435.5	11389.4
T (K)	123.15	123.15	123.15
Z	2	2	2
ρ calcd (g cm^{-3})	1.568	1.526	1.512
R1 [I > 2σ(I)]	0.0821	0.1194	0.0562
wR2 [I > 2σ(I)]	0.1824	0.2930	0.1103

Table A9. Crystallographic parameters and refinement details for (Δ,Δ,Δ,Δ,Δ,Δ,Δ,Δ)-[(*R*)-^{i}Pr-pybox]$_8$(Eu^{III})$_8$$L^2_8$ (**5-Eu^{iPr}*RRRRRRRR***) and (Λ,Λ,Λ,Λ,Λ,Λ,Λ,Λ)-[(*S*)-^{i}Pr-pybox]$_8$(Eu^{III})$_8$$L^2_8$ (**5-Eu^{iPr}*SSSSSSSS***).

	5-Eu^{iPr}*RRRRRRRR*	**5-Eu^{iPr}*SSSSSSSS***
formula sum	$Eu_8C_{328}H_{232}F_{168}N_{24}O_{64}$	$Eu_8C_{328}H_{232}F_{168}N_{24}O_{64}$
formula weight	9941.01	9941.01
crystal system	tetragonal	tetragonal
space group	I4	I4
a (Å)	30.7047	30.7803
b (Å)	30.7047	30.7803
c (Å)	23.1299	23.1544
α (deg)	90	90
β (deg)	90	90
γ (deg)	90	90
V (Å^3)	21806.5(19)	21937.0
T (K)	123.15	123.15
Z	2	2
ρ calcd (g cm^{-3})	1.561	1.555
R1 [I > 2σ(I]]	0.0670	0.0489
wR2 [I > 2σ(I]]	0.1673	0.1153

Table A10. Crystallographic parameters and refinement details for (Δ,Δ,Δ,Δ,Δ,Δ,Δ,Δ)-[(*R*)-^{i}Pr-pybox]$_8$(Tb^{III})$_8$$L^2_8$ (**5-Tb^{iPr}*RRRRRRRR***) and (Λ,Λ,Λ,Λ,Λ,Λ,Λ,Λ)-[(*S*)-^{i}Pr-pybox]$_8$(Tb^{III})$_8$$L^2_8$ (**5-Tb^{iPr}*SSSSSSSS***).

	5-Tb^{iPr}*RRRRRRRR*	**5-Tb^{iPr}*SSSSSSSS***
formula sum	$Tb_8C_{328}H_{232}F_{168}N_{24}O_{64}$	$Tb_8C_{328}H_{232}F_{168}N_{24}O_{64}$
formula weight	9996.70	9996.70
crystal system	tetragonal	tetragonal
space group	I4	I4
a (Å)	30.7532	30.7233
b (Å)	30.7532	30.7233
c (Å)	23.0554	23.0251
α (deg)	90	90
β (deg)	90	90
γ (deg)	90	90
V (Å^3)	21804.9	21733.9
T (K)	123.15	123.15
Z	2	2
ρ calcd (g cm^{-3})	1.570	1.575
R1 [I > 2σ(I]]	0.0493	0.0489
wR2 [I > 2σ(I]]	0.1152	0.1171

APPENDIX-CRYSTAL STRUCTURE

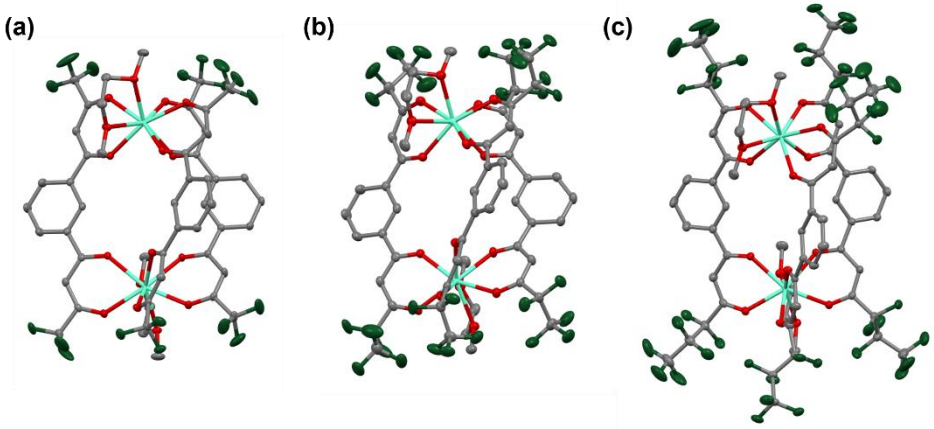

Figure A1. Crystal structures of (a) $Eu^{III}_2(BTP)_3(DME)_2$, (b) $Eu^{III}_2(BPP)_3(DME)_2$ (c) $Eu^{III}_2(BHP)_3(DME)_2$. Hydrogens atoms are omitted for clarity.

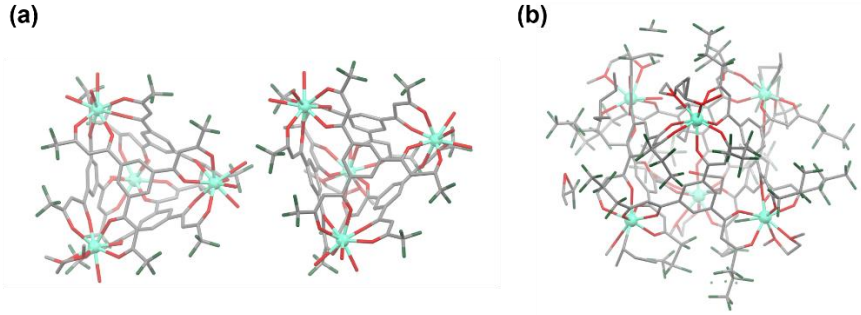

Figure A2. Poor resolved crystal structures of (a) (Δ,Δ,Δ,Δ)-/(Λ,Λ,Λ,Λ)-$Eu^{III}_4(TTP)_4(DME)_4(OH_2)_4$ and (b) (Δ,Δ,Δ,Δ,Δ,Δ)-/(Λ,Λ,Λ,Λ,Λ,Λ)- $[Eu_6(THP)_6(DME)_6]$. Only (Λ,Λ,Λ,Λ,Λ,Λ)- form is shown.

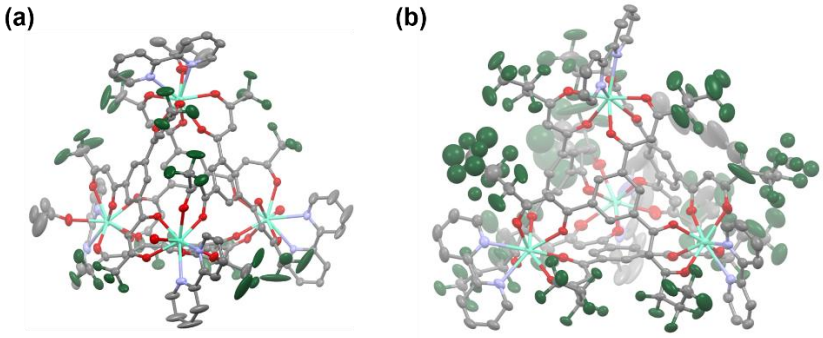

Figure A3. Crystal structures of (a) (Δ,Δ,Δ,Δ)-/(Λ,Λ,Λ,Λ)-$Eu^{III}_4(TTP)_4(bipy)_4(MEK)_2(OH_2)_2$ Only (Λ,Λ,Λ,Λ)- form is shown. and (b) (Δ,Δ,Δ,Δ)-/(Λ,Λ,Λ,Λ)- $[Eu_6(THP)_6(MEK)_6]$. Only (Λ,Λ,Λ,Λ)-form is shown. Hydrogens atoms are omitted for clarity.

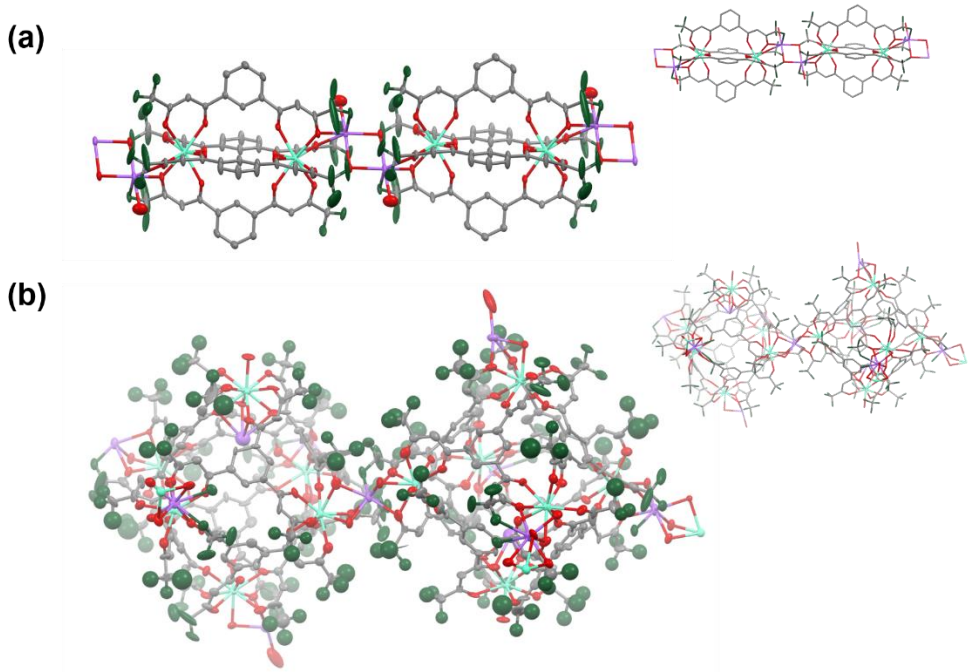

Figure A4. Crystal structures of (a) $2Na^{+}[Eu^{III}_{2}(BTP)_{4}]^{2-}$ and (b) $6Na^{+}[Eu^{III}_{6}(TTP)_{8}]^{6-}$. Hydrogens atoms are omitted for clarity.

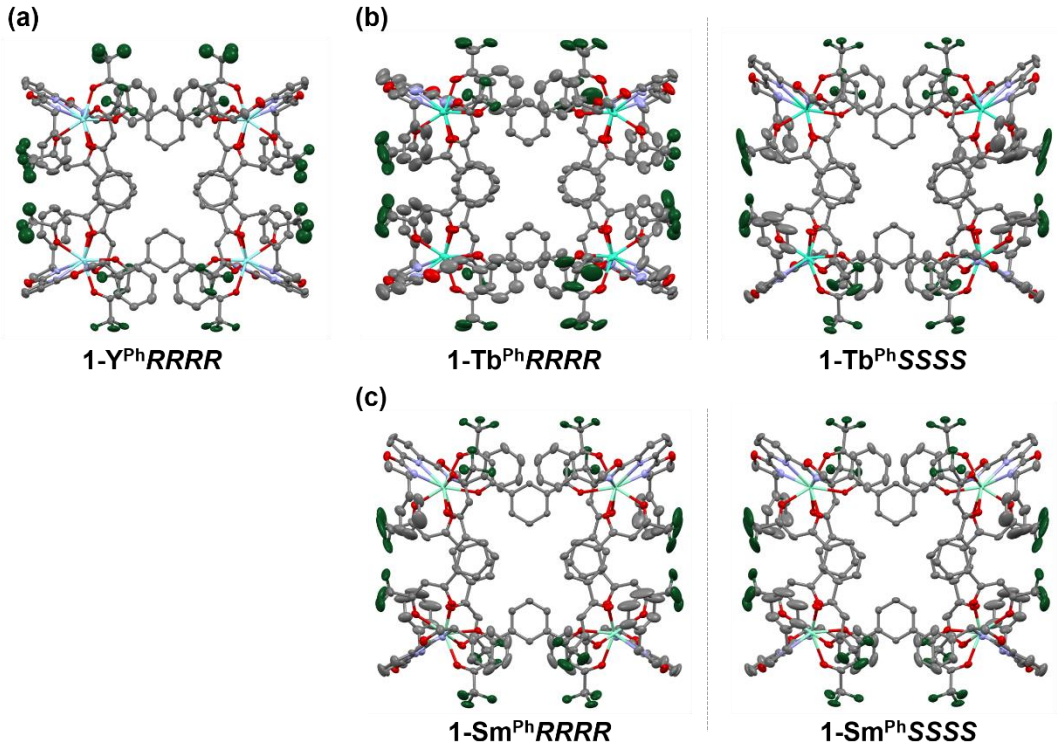

Figure A5. Crystal structures of (a) **1-Y^{Ph}*RRRR*** (b) **1-Tb^{Ph}*RRRR*** and **1-Tb^{Ph}*SSSS*** and (c) **1-Sm^{Ph}*RRRR*** and **1-Sm^{Ph}*SSSS***. Solvents and hydrogens atoms are omitted for clarity.

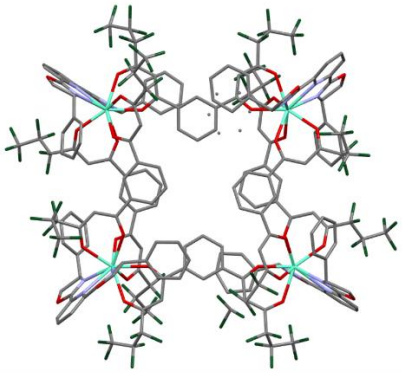

3-Eu^{Ph}*RRRR*

Figure A6. Poor resolved crystal structures of **3-Eu^{Ph}*RRRR***.

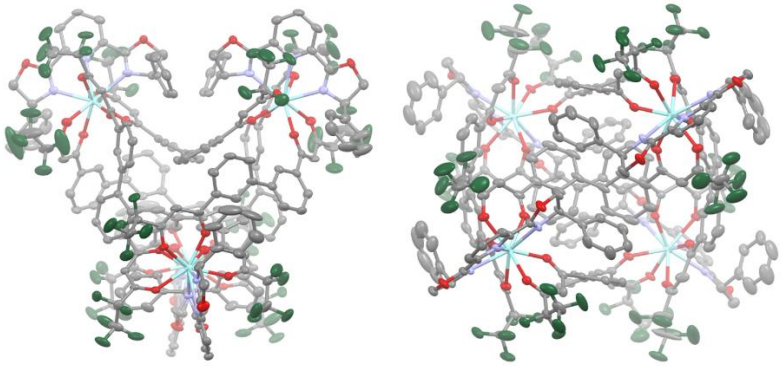

4-Y^{Ph}*RRRR*

Figure A7. Crystal structures of **4-Y^{Ph}*RRRR***. Solvents and hydrogens atoms are omitted for clarity.

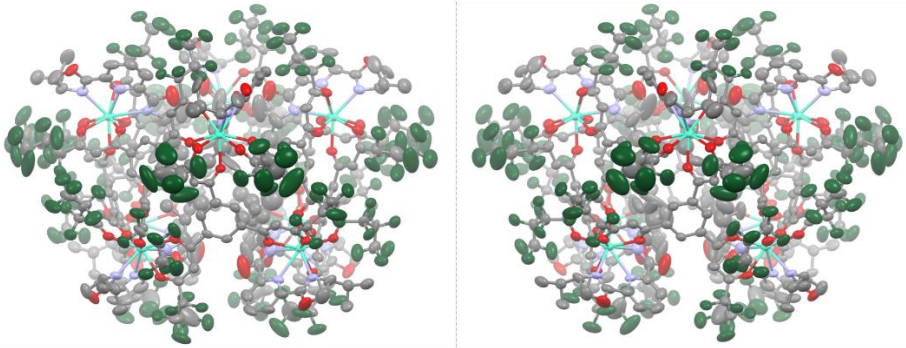

5-Tb^{iPr}*RRRRRRRR* **5-Tb^{iPr}*SSSSSSSS***

Figure A8. Crystal structures of **5-Tb^{iPr}*RRRRRRRR*** and **5-Tb^{iPr}*SSSSSSSS.*** Solvents and hydrogens atoms are omitted for clarity.

APPENDIX-EU COORDINATION GEOMETRIES (from X- ray crystal structure)

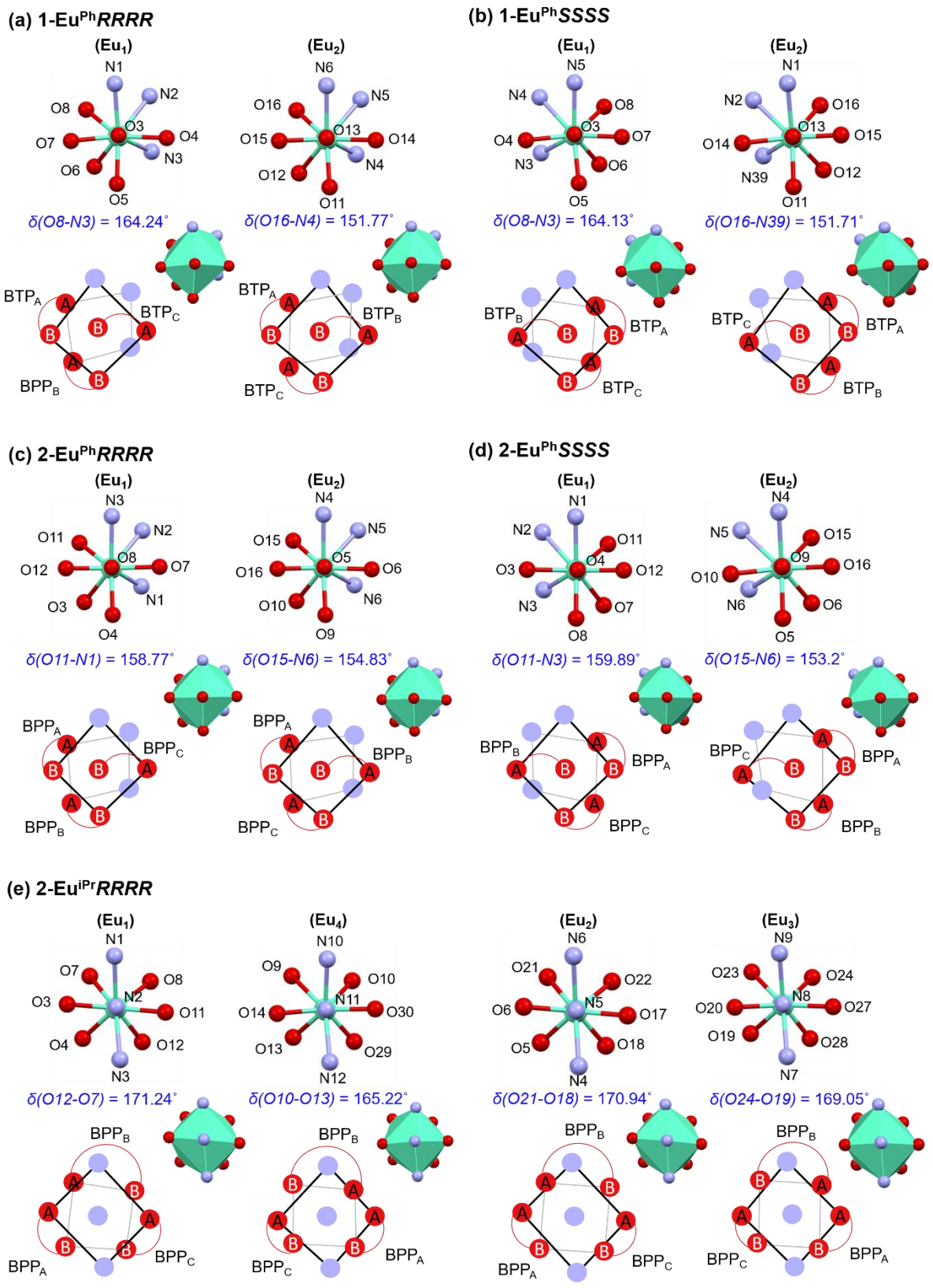

Figure A9. Eu^{III} coordination geometries of (a) **1-Eu^{Ph}*RRRR***, (b) **1-Eu^{Ph}*SSSS***, (c) **2-Eu^{Ph}*RRRR***, (d) **2-Eu^{Ph}*SSSS***, and (e) **2-Eu^{iPr}*RRRR***.

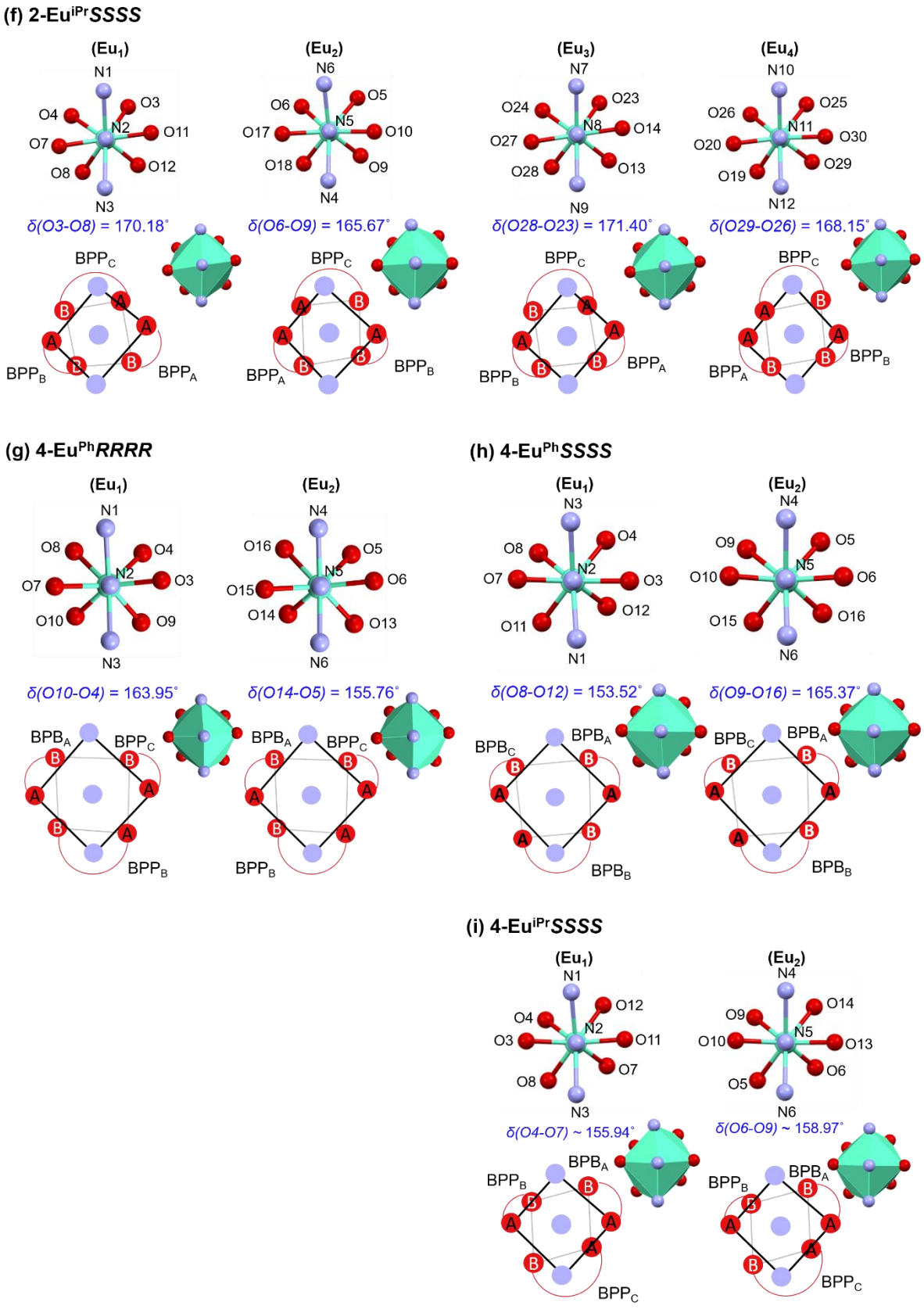

Figure A10. Eu^{III} coordination geometries of (f) **2-Eu^{iPr}*SSSS***, (g) **4-Eu^{Ph}*RRRR***, (h) **4-Eu^{Ph}*SSSS***, and (i) **4-Eu^{iPr}*SSSS***.

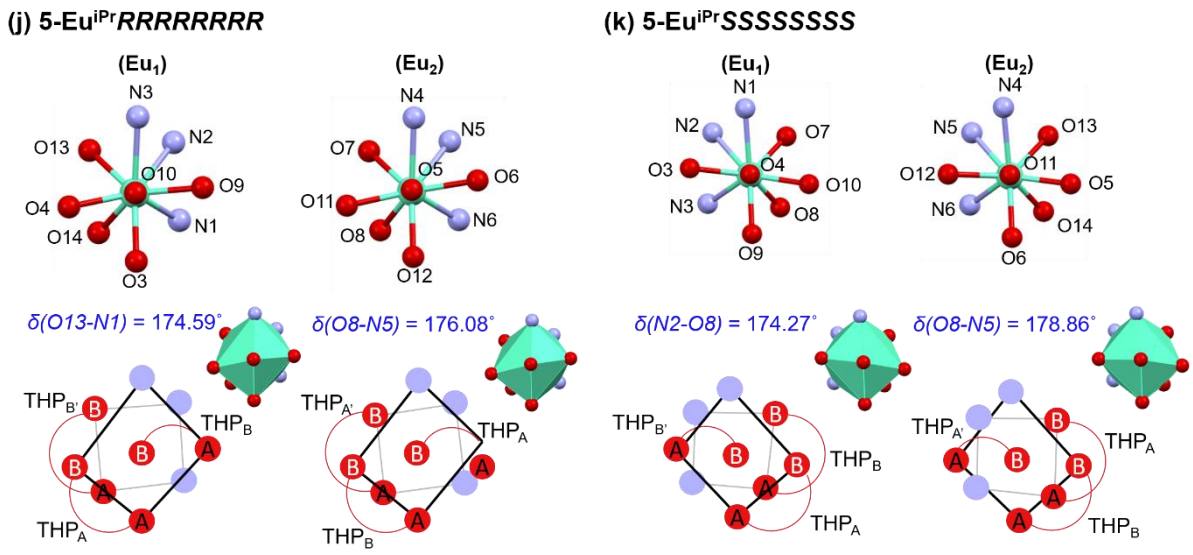

Figure A11. Eu^{III} coordination geometries of (j) **5-Eu^{iPr}*RRRRRRRR***, and (k) **5-Eu^{iPr}*SSSSSSSS***.

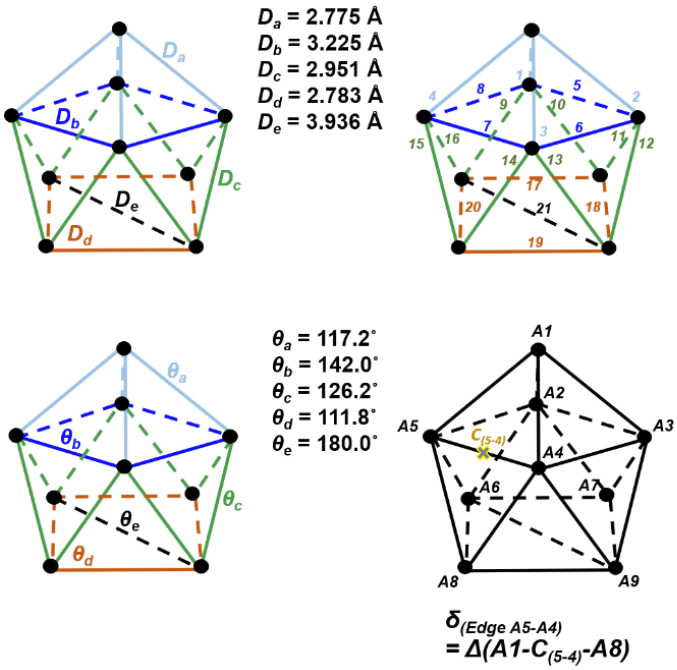

Figure A12. (Top-left) Corresponding estimated distance of an ideal capped square geometry. (Top-center) The numbering of each edge. (Bottom-left) Corresponding estimated dihedral angle of an ideal capped square geometry. (Bottom-center) Observed dihedral angle along the A5-A4 edge.

Table A11. Distance and dihedral angle along each edge of the primary coordination sphere of **1-Eu^{Ph}*RRRR*** and **1-Eu^{Ph}*SSSS***.

i	**1-Eu^{Ph}*RRRR***						**1-Eu^{Ph}*SSSS***					
	Eu_1			**Eu_2**			**Eu_1**			**Eu_2**		
	Edge	**d_i (Å)**	**δ_i (˚)**	**Edge**	**d_i (Å)**	**δ_i (˚)**	**Edge**	**d_i (Å)**	**δ_i (˚)**	**Edge**	**d_i (Å)**	**δ_i (˚)**
1	N1-O3	2.852	108.70	N6-O13	2.787	108.97	O3-N5	2.850	108.88	O13-N1	2.781	109.27
2	O4-O3	2.735	114.53	O14-O13	2.766	123.03	O3-O7	2.700	121.75	O15-O13	2.683	119.16
3	O5-O3	2.839	124.99	O11-O13	2.729	118.99	03-O5	2.837	125.00	O11-O13	2.724	119.04
4	O3-O7	2.707	121.62	O13-O15	2.692	119.72	O3-O4	2.741	114.24	O14-O13	2.770	123.26
5	O4-N1	3.509	155.65	O14-N6	3.368	153.47	N5-O7	3.354	141.30	O15-N1	3.327	141.32
6	O4-O5	3.170	133.07	O14-O11	3.018	128.58	O7-O5	2.942	135.87	O11-O15	3.144	147.39
7	O5-O7	2.944	136.10	O15-O11	3.137	146.66	O5-O4	3.176	133.28	O11-O14	3.009	128.68
8	N1-O7	3.367	141.49	N6-O15	3.332	141.06	O4-N5	3.517	155.91	N1-O14	3.356	153.33
9	N1-O8	2.932	129.11	N6-O16	3.024	129.98	N5-N4	2.697	110.29	N1-N2	2.705	110.99
10	N2-N1	2.696	110.08	N5-N6	2.701	110.66	N5-O8	2.932	128.89	O16-N1	3.026	129.96
11	N2-O4	2.946	124.07	N5-O14	2.789	121.03	O7-O8	2.831	125.55	O15-O16	2.805	128.92
12	N3-O4	2.969	124.98	N4-O14	3.091	131.95	O7-O6	3.028	133.63	O12-O15	2.833	125.08
13	N3-O5	3.469	142.39	N4-O11	3.527	143.25	O5-O6	2.726	119.69	O12-O11	2.758	112.34
14	O6-O5	2.725	119.58	O12-O11	2.762	112.37	O5-N3	3.470	142.40	N39-O11	3.508	143.29
15	O7-O6	3.015	133.17	O15-O12	2.827	125.36	O4-N3	2.958	124.61	N39-O14	3.088	132.31
16	O8-O7	2.826	125.65	O16-O15	2.804	129.16	O4-N4	2.933	123.98	N2-O14	2.781	120.92
17	N2-O8	3.048	122.96	O16-O15	3.000	129.16	N4-O8	3.057	116.59	O16-N2	3.014	125.36
18	N2-N3	2.709	106.90	N5-N4	2.693	108.33	O8-O6	2.700	122.99	012-O16	2.896	123.13
19	N3-O6	2.781	98.83	N4-O12	2.828	104.89	O6-N3	2.781	107.16	O12-N39	2.831	104.98
20	O8-O6	2.702	116.91	O16-O12	2.878	123.31	N3-N4	2.707	98.66	N39-N2	2.693	108.29
21	O8-N3	3.676	164.24	O16-N4	3.437	151.77	N3-O8	3.688	164.13	O16-N39	3.447	151.71

Table A12. Distance and dihedral angle along each edge of the primary coordination sphere of **2-Eu^{Ph}*RRRR*** and **2-Eu^{Ph}*SSSS***.

i	**2-Eu^{Ph}*RRRR***						**2-Eu^{Ph}*SSSS***					
	Eu_1			**Eu_2**			**Eu_1**			**Eu_2**		
	Edge	**d_i (Å)**	**δ_i (˚)**	**Edge**	**d_i (Å)**	**δ_i (˚)**	**Edge**	**d_i (Å)**	**δ_i (˚)**	**Edge**	**d_i (Å)**	**δ_i (˚)**
1	N3-O8	2.835	113.29	N4-O5	2.877	108.83	O4-N1	2.867	112.83	O9-N4	2.829	108.53
2	O7-O8	2.751	120.19	O6-O5	2.750	121.79	O4-O12	2.652	118.86	O9-O16	2.724	121.19
3	O4-O8	2.723	116.97	O9-O5	2.731	118.23	O4-O8	2.729	116.90	O9-O5	2.712	119.54
4	O8-O12	2.645	119.45	O5-O16	2.710	121.36	O4-O3	2.753	119.43	O9-O10	2.755	122.02
5	O7-N3	3.263	148.09	N6-O6	3.434	130.66	N1-O12	3.262	140.26	N4-O16	3.343	139.61
6	O7-O4	3.153	135.26	O6-O9	3.055	132.09	O12-O8	3.066	148.26	O16-O5	3.143	145.74
7	O12-O4	3.099	147.46	O9-O16	3.127	146.12	O8-O3	3.135	136.68	O5-O10	3.013	130.35
8	N3-O12	3.260	139.48	N4-O16	3.343	139.59	O3-N1	3.253	148.85	O10-N4	3.459	155.99
9	N3-O11	3.141	131.87	N4-O15	3.075	128.06	N1-N2	2.718	112.66	N4-N5	2.727	109.25
10	N2-N3	2.722	119.53	N5-N4	2.746	110.01	N1-O11	3.127	131.59	N4-O15	3.069	129.04
11	N2-O7	2.840	125.22	N5-O6	2.757	122.93	O12-O11	2.773	127.61	O16-O15	2.792	128.49
12	N1-O7	3.073	129.32	N6-O6	2.987	130.66	O12-O7	2.958	130.03	O16-O6	2.866	127.10
13	N1-O4	3.398	140.61	N6-O9	3.468	141.62	O8-O7	2.717	114.70	O5-O6	2.760	113.67
14	O3-O4	2.732	114.25	O10-O9	2.768	113.96	O8-N3	3.367	140.60	O5-N6	3.482	143.28
15	O12-O3	2.965	130.07	O16-O10	2.871	127.93	O3-N3	3.049	129.25	O10-N6	2.987	130.35
16	O11-O12	2.777	127.42	O15-O16	2.788	129.21	O3-N2	2.845	125.59	O10-N5	2.776	121.77
17	N2-O11	3.025	112.90	N5-O15	3.106	128.06	N2-O11	3.027	119.14	N5-O15	3.134	124.97
18	N2-N1	2.702	108.09	N5-N6	2.703	108.36	O11-O7	2.783	116.58	O15-O6	2.881	120.69
19	N1-O3	2.827	103.56	N6-O10	2.876	104.46	O7-N3	2.833	103.32	O6-N6	2.872	104.39
20	O11-O3	2.794	117.38	O15-O10	2.847	119.39	N3-N2	2.693	107.69	N6-N5	2.745	109.03
21	O11-N1	3.585	158.77	O15-N6	3.587	154.83	N3-O11	3.591	159.89	N6-O15	3.576	153.20

Table A13. Distance and dihedral angle along each edge of the primary coordination sphere of **2-Eu^{iPr}*RRRR***.

i	**2-Eu^{iPr}*RRRR***											
	Eu_1			**Eu_2**			**Eu_3**			**Eu_4**		
	Edge	**d_i (Å)**	**δ_i (˚)**	**Edge**	**d_i (Å)**	**δ_i (˚)**	**Edge**	**d_i (Å)**	**δ_i (˚)**	**Edge**	**d_i (Å)**	**δ_i (˚)**
1	N2-N1	2.717	109.58	N5-N4	2.736	110.94	N8-N9	2.701	106.51	N11-N10	2.690	110.02
2	N2-O11	2.843	126.15	N5-O6	2.746	123.41	N8-O27	2.922	125.25	N11-O30	2.855	128.11
3	N2-N3	2.723	110.07	N5-N6	2.727	111.46	N8-N7	2.729	111.32	N11-N12	2.742	111.92
4	N2-O3	2.789	122.36	N5-17	2.784	124.22	N8-O20	2.731	124.05	N11-O14	2.702	118.40
5	N1-O11	3.408	147.00	N4-O6	3.397	147.01	N9-O27	3.419	143.30	N10-O30	3.109	138.19
6	O11-N3	2.968	135.85	O6-N6	2.986	137.00	O27-N7	3.083	138.16	O30-N12	3.150	139.37
7	N3-O3	3.446	148.60	N6-O17	3.440	147.50	N7-O20	3.235	140.95	N12-O14	3.212	138.44
8	O3-N1	3.035	137.54	O17-N4	3.008	136.25	O20-N9	3.151	144.42	O14-N10	3.307	151.98
9	N1-O7	3.095	122.91	N4-O18	3.042	123.62	N9-O23	2.949	116.70	N10-O9	2.963	117.80
10	N1-O8	3.262	124.63	N4-O5	3.188	122.55	N9-O24	3.410	128.92	N10-O10	3.169	130.58
11	O11-O8	2.771	122.53	O6-O5	2.842	123.92	O27-O24	2.929	123.99	O30-O10	2.969	129.36
12	O11-O12	2.821	137.55	O6-O21	2.834	133.42	O27-O28	2.773	133.75	O30-O29	2.770	131.39
13	N3-O12	2.959	126.63	N6-O21	3.012	123.94	N7-O28	2.940	119.68	N12-O29	2.923	118.06
14	N3-O4	3.169	123.42	N6-O22	3.139	124.52	N7-O19	3.298	130.11	N12-O13	3.314	130.35
15	O3-O4	2.748	122.72	O17-O22	2.743	124.33	O20-O19	2.749	126.56	O14-O13	2.777	128.33
16	O3-O7	2.979	133.66	O17-O18	2.964	135.79	O20-O23	2.902	134.10	O14-O9	2.890	127.05
17	O7-O8	2.732	109.02	O18-O5	2.732	114.92	O23-O24	2.743	104.17	O9-O10	2.742	108.43
18	O8-O12	2.736	110.73	O5-O21	2.726	108.77	O24-O28	2.760	109.63	O10-O29	2.737	110.92
19	O12-O4	2.678	114.54	O21-O22	2.759	109.45	O28-O19	2.674	108.92	O29-O13	2.738	111.39
20	O4-O7	2.832	108.37	O22-O18	2.802	110.02	O19-O23	2.762	113.70	O13-O9	2.756	113.84
21	O12-O7	3.778	171.24	O21-O18	3.805	170.94	O24-O19	3.748	169.06	O10-O13	3.664	165.22

Table A13. Distance and dihedral angle along each edge of the primary coordination sphere of **2-Eu^{iPr}*SSSS***.

i	**2-Eu^{iPr}*SSSS***											
	Eu_1			**Eu_2**			**Eu_3**			**Eu_4**		
	Edge	**d_i (Å)**	**δ_i (˚)**	**Edge**	**d_i (Å)**	**δ_i (˚)**	**Edge**	**d_i (Å)**	**δ_i (˚)**	**Edge**	**d_i (Å)**	**δ_i (˚)**
1	N2-N1	2.71	109.35	N5-N6	2.710	110.05	N8-N7	2.721	111.15	N11-N10	2.684	106.36
2	N2-O11	2.805	122.23	N5-O10	2.704	118.39	N8-O14	2.790	123.78	N11-O30	2.737	124.82
3	N2-N3	2.742	109.73	N5-N4	2.744	111.37	N8-N9	2.739	110.99	N11-N12	2.724	111.52
4	N2-O7	2.861	125.97	N5-O17	2.870	128.11	N8-O27	2.738	123.61	N11-O20	2.888	124.87
5	N1-O11	3.032	138.81	N6-O10	3.301	151.73	N7-O14	2.977	137.08	N10-O30	3.153	144.11
6	O11-N3	3.450	148.90	O10-N4	3.219	139.05	O14-N9	3.435	147.32	O30-N12	3.218	140.20
7	N3-O7	2.981	135.64	N4-O17	3.156	139.79	N9-O27	2.970	136.55	N12-O20	3.086	138.62
8	O7-N1	3.400	146.66	O17-N6	3.114	138.22	O27-N7	3.403	148.05	O20-N10	3.410	142.82
9	N1-O4	3.254	125.56	N6-O6	3.159	130.64	N7-O24	3.204	124.80	N10-O26	3.417	129.20
10	N1-O3	3.126	122.38	N6-O5	2.953	117.72	N7-O23	3.070	123.80	N10-O25	2.966	116.28
11	O11-O3	2.975	132.90	O10-O5	2.889	127.51	O14-O23	2.968	133.68	O30-O25	2.900	133.89
12	O11-O12	2.751	123.57	O10-O9	2.773	128.04	O14-O13	2.755	124.31	O30-O29	2.768	127.14
13	N3-O12	3.185	123.35	N4-O9	3.313	130.24	N9-O13	3.152	122.83	N12-O29	3.301	130.52
14	N3-O8	2.972	123.64	N4-O18	2.920	117.80	N9-O28	2.976	123.60	N12-O19	2.929	119.43
15	O7-O8	2.861	137.32	O17-O18	2.770	131.31	O27-O28	2.825	135.91	O20-O19	2.779	133.33
16	O7-O4	2.772	122.49	O17-O6	2.949	129.37	O27-O24	2.843	123.91	O20-O26	2.935	124.36
17	O4-O3	2.743	108.87	O6-O5	2.726	108.49	O24-O23	2.745	108.76	O26-O25	2.734	104.76
18	O3-O12	2.837	108.06	O5-O9	2.758	113.65	O23-O13	2.787	107.52	O25-O29	2.759	113.49
19	O12-O8	2.658	114.42	O9-O18	2.743	111.17	O13-O28	2.752	115.36	O29-O19	2.657	109.00
20	O8-O4	2.734	117.07	O18-O6	2.741	111.20	O28-O24	2.725	110.66	O19-O26	2.761	110.28
21	O8-O3	3.795	170.18	O6-O9	3.666	165.67	O28-O23	3.811	171.40	O29-O26	3.715	168.15

Table A14. Distance and dihedral angle along each edge of the primary coordination sphere of **4-Eu^{Ph}*RRRR*** and **4-Eu^{Ph}*SSSS***.

i	**4-Eu^{Ph}*RRRR***						**4-Eu^{Ph}*SSSS***					
	Eu_1			**Eu_2**			**Eu_1**			**Eu_2**		
	Edge	**d_i (Å)**	**δ_i (˚)**	**Edge**	**d_i (Å)**	**δ_i (˚)**	**Edge**	**d_i (Å)**	**δ_i (˚)**	**Edge**	**d_i (Å)**	**δ_i (˚)**
1	N2-N1	2.712	122.06	N5-N4	2.719	110.79	N2-N3	2.702	109.70	N5-N4	2.719	114.48
2	N2-O3	2.719	109.50	N5-O6	2.814	122.85	N2-O3	2.431	124.01	N5-O6	2.778	122.61
3	N2-N3	2.673	124.81	N5-N6	2.680	109.57	N2-N1	2.722	109.92	N5-N6	2.569	109.92
4	N2-O7	2.788	139.71	N5-O15	2.801	124.18	N2-O7	2.825	124.36	N5-O10	2.723	121.22
5	N1-O3	3.131	148.38	N4-O6	3.106	137.4	N3-O3	3.314	148.83	N4-O6	3.127	141.15
6	03-N3	3.243	139.64	O6-N6	3.319	150.53	O3-N1	3.116	135.30	O6-N6	3.139	143.57
7	N3-O7	3.164	140.75	N6-O15	3.092	134.54	N1-O7	3.342	146.50	N6-O10	3.185	148.54
8	O7-N1	3.160	120.75	O15-N4	3.271	145.96	O7-N3	3.116	133.26	O10-N4	3.087	138.16
9	N1-O8	2.933	128.05	N4-O16	2.850	116.51	N3-O8	3.375	137.44	N4-O9	3.343	130.35
10	N1-O4	3.321	125.78	N4-O5	3.290	131.38	N3-O4	2.853	110.90	N4-O5	2.932	120.90
11	O3-O4	2.796	132.73	O6-O5	2.812	128.63	O3-O4	2.777	129.48	O6-O5	2.749	130.07
12	O3-O9	2.949	116.41	O6-O13	2.838	127.85	O3-O12	2.994	127.99	O6-O16	2.906	126.50
13	N3-O9	2.926	132.08	N6-O13	2.942	112.37	N1-O12	3.435	133.65	N6-O16	3.136	132.29
14	N3-O10	3.241	127.81	N6-O14	3.366	135.92	N1-O11	2.915	113.54	N6-O15	2.857	118.94
15	O7-O10	2.936	131.27	O15-O14	2.974	129.16	O7-O11	2.894	127.79	O10-O15	2.984	133.03
16	O7-O8	2.752	110.14	O15-O16	2.762	127.46	O7-O8	2.806	128.50	O10-O9	2.815	124.25
17	O8-O4	2.815	112.11	O16-O5	2.738	114.49	O8-O4	2.756	110.07	O9-O5	2.853	108.00
18	O4-O9	2.827	107.11	O5-O13	2.803	116.97	O4-O12	2.685	118.60	O5-O16	2.738	111.94
19	O9-O10	2.703	111.13	O13-O14	2.727	110.37	O12-O11	2.686	115.89	O16-O15	2.667	106.12
20	O10-O8	2.667	163.95	O14-O16	2.669	114.86	O11-O8	2.756	115.84	O15-O9	2.809	110.97
21	O10-O4	3.760	122.06	O14-O5	3.499	155.76	O8-O12	3.429	153.52	O9-O16	3.799	165.37

Table A15. Distance and dihedral angle along each edge of the primary coordination sphere of **5-Eu^{iPr}*RRRRRRRR*** and **5-Eu^{iPr}*SSSSSSSS***.

i	5-Eu^{iPr}*RRRRRRRR*						5-Eu^{iPr}*SSSSSSSS*					
	Eu$_1$			**Eu$_2$**			**Eu$_1$**			**Eu$_2$**		
	Edge	***d$_i$* (Å)**	**δ_i (˚)**	**Edge**	***d$_i$* (Å)**	**δ_i (˚)**	**Edge**	***d$_i$* (Å)**	**δ_i (˚)**	**Edge**	***d$_i$* (Å)**	**δ_i (˚)**
1	N3-O10	2.984	107.07	O5-N4	2.927	110.76	O4-N1	2.965	111.26	O11-N4	2.960	108.4
2	O9-O10	2.797	121.16	O5-O6	2.750	120.50	O4-O10	2.824	118.93	O11-O5	2.803	117.43
3	O3-O10	2.859	120.58	O5-O12	2.836	120.60	O4-O9	2.800	119.40	O11-O6	2.829	120.38
4	O10-O4	2.797	117.29	O5-O11	2.839	110.76	O4-O3	2.756	120.07	O11-O12	2.765	120.55
5	O9-N3	3.166	140.85	N4-O6	3.048	138.33	N1-O10	3.741	152.04	N4-O5	3.697	153.07
6	O9-O3	3.273	141.06	O6-O12	3.412	144.91	O10-O9	2.860	132.46	O5-O6	2.882	136.16
7	O4-O3	2.86	135.67	O12-O11	2.862	132.53	O9-O3	3.423	146.28	O6-O12	3.267	141.41
8	N3-O4	3.741	153.55	O11-N4	3.777	152.65	O3-N1	3.081	137.80	O12-N4	3.150	140.33
9	N3-O13	2.913	119.58	N4-O7	2.895	120.92	N1-N2	2.741	120.88	N4-N5	2.765	118.67
10	N2-N3	2.776	118.07	N4-N5	2.703	120.07	N1-O7	2.854	119.60	N4-O13	2.894	120.48
11	N2-O9	2.889	133.42	O6-N5	2.817	133.67	O10-O7	2.860	122.21	O5-O13	2.860	123.26
12	N1-O9	2.996	126.70	O6-N6	2.990	124.66	O10-O8	2.827	128.97	O5-O14	2.805	128.57
13	N1-O3	3.279	130.33	O12-N6	3.192	127.1	O9-O8	2.906	130.26	O6-O14	2.855	127.2
14	O14-O3	2.854	127.52	O12-O8	2.907	129.78	O9-N3	3.171	125.21	O6-N6	3.226	130.51
15	O4-O14	2.786	128.49	O11-O8	2.879	128.14	O3-N3	2.942	124.00	O12-N6	2.982	125.97
16	O13-O4	2.900	123.96	O11-O7	2.884	121.81	O3-N2	2.816	133.81	O12-N5	2.933	133.55
17	N2-O13	2.793	115.85	O7-N5	2.781	120.76	N2-O7	2.789	120.23	N5-O13	2.774	117.89
18	N2-N1	2.612	102.16	N5-N6	2.716	108.37	O7-O8	2.735	113.86	O13-O14	2.777	113.42
19	N1-O14	2.709	100.73	N6-O8	2.706	107.62	O8-N3	2.740	109.41	O14-N6	2.689	108.43
20	O13-O14	2.759	112.08	O8-O7	2.763	112.86	N3-N2	2.706	108.55	N6-N5	2.642	103.44
21	O13-N1	3.805	174.59	O8-N5	3.871	176.08	N2-O8	3.822	174.27	N5-O14	3.870	178.86

APPENDIX-LIGAND-TO-LIGAND INTERACTIONS

Table A16. Summary of ligand-ligand interactions found in the crystal structure of **1-Eu^{Ph}*RRRR***, **1-Eu^{Ph}*SSSS***, **2-Eu^{Ph}*RRRR***, **2-Eu^{Ph}*SSSS***, **2-Eu^{iPr}*RRRR***, **2-Eu^{iPr}*SSSS***, **4-Eu^{Ph}*RRRR***, **4-Eu^{Ph}*SSSS***, and **5-Eu^{iPr}*RRRRRRRR*** and **5-Eu^{iPr}*SSSSSSSS***.

Self-assemblies	Ligand-ligand Interactions		Around	Distance (Å)
1-Eu^{Ph}*RRRR*	π(β-diketonate)_ π(Ph$_1$)		Eu$_1$ Eu$_2$	3.511 3.636
1-Eu^{Ph}*SSSS*	π(β-diketonate)_ π(Ph$_1$)		Eu$_1$ Eu$_2$	3.517 3.642
2-Eu^{Ph}*RRRR*	π(β-diketonate)_ π(Ph$_1$)		Eu$_1$ Eu$_2$	3.894 3.781
	CF_F	F(5)_F(25) F(15)_F(7)	Eu$_1$ Eu$_2$	2.880 2.839
2-Eu^{Ph}*SSSS*	π(β-diketonate)_ π(Ph$_1$)		Eu$_1$ Eu$_2$	3.897 3.740
	CF_F	F(14)_F(25) F(30)_F(6)	Eu$_1$ Eu$_2$	2.846 3.837
2-Eu^{iPr}*RRRR*	CH(^{i}Pr)_π(β-diketonate)	H(15D)_π H(14)_π H(2)_π H(68C)_π H(81)_π H(69)_π H(11E)_π H(130)_π H(118)_π H(16H)_π H(151)_π H(161)_π	Eu$_1$ Eu$_1$ Eu$_1$ Eu$_2$ Eu$_2$ Eu$_2$ Eu$_3$ Eu$_3$ Eu$_3$ Eu$_4$ Eu$_4$ Eu$_4$	3.172 2.861 2.586 2.978 2.459 3.057 2.817 2.508 2.883 2.765 2.978 2.907
	CH_F	H(1C)_F(12) H(4)_F(13) H(82B)_F(45) H(12D)_F(50) H(13E)_F(48) H(13C)_F(51) H(149)_F(17) H(14B)_F(17) H(15F)_F(57)	Eu$_1$ Eu$_1$ Eu$_2$ Eu$_3$ Eu$_3$ Eu$_3$ Eu$_4$ Eu$_4$ Eu$_4$	2.927 2.698 3.146 3.002 2.707 2.676 2.817 2.863 2.976
	CF_F	F(13)_F(1) F(48)_F(53)	Eu$_1$ Eu$_3$	2.944 2.944
2-Eu^{iPr}*SSSS*	CH(^{i}Pr)_ π	H(15D)_π H(2)_π H(14)_π H(68B)_π H(79)_π H(69)_π H(11D)_π H(112)_π H(100)_π H(16D_π H(149)_π H(161)_π	Eu$_1$ Eu$_1$ Eu$_1$ Eu$_2$ Eu$_2$ Eu$_2$ Eu$_3$ Eu$_3$ Eu$_3$ Eu$_4$ Eu$_4$ Eu$_4$	3.044 2.567 2.832 2.656 2.979 2.917 3.042 3.060 2.505 2.796 2.523 2.896
	CH_F	H(1C)_F(1) H(4)_F(3)	Eu$_1$ Eu$_1$	2.813 2.725

		H(3C)_F(15)	Eu_1	3.035
		H(81)_F(6)	Eu_2	2.826
		H(82A)_F(6)	Eu_2	2.890
		H(80B)_F(34)	Eu_2	3.147
		H(80B)_F(31)	Eu_2	3.029
		H(99C)_F(45)	Eu_3	3.123
		H(102)_F(45)	Eu_3	3.185
		H(15G)_F(40)	Eu_4	2.696
		H(15H)_F(50)	Eu_4	2.602
		H(14A)_F(49)	Eu_4	2.930
	CF_F	F(22)_F(3)	Eu_1	2.918
		F(39)_F(50)	Eu_4	2.992
4-Eu^{Ph}*RRRR*	*π*(*β*-diketonate)_ *π*(Ph_1)		Eu_1	3.883
			Eu_2	3.940
	CH(Pybox)_HC(Pybox)	H(8A)_H(8A)	In between two Eu_1	2.383
		H(75A)_H(75A)	In between two Eu_2	2.150
	CF_F	F(2)_F(16A)	Eu_1	2.878
4-Eu^{Ph}*SSSS*	*π*(*β*-diketonate)_ *π*(Ph_1)		Eu_1	3.869
			Eu_2	3.879
	CH(Pybox)_HC(Pybox)	H(16B)_H(86A)	In between Eu_1/ Eu_2	2.265
	CF_F	F(20)_F(31)	Eu_2	2.870
5-Eu^{iPr}*RRRRRRRR*	CH_O	H13B)_O(2)	Eu_1	3.003
		H(70A)_O(15)	Eu_2	2.847
	CF_ *π*(*β*-diketonate)	F(3)_ *π*	Eu_1	2.959
	CF_ *π* (Pybox)	F(2)_ *π*(*Py*)	Eu_2	3.071
	CH_F	H(3B)_F(28)	Eu_1	2.914
		H(1B)_F(6)	Eu_1	2.726
		H(1C)_F(1)	Eu_1	2.845
		H(2)_F(1)	Eu_1	2.694
		H(2)_F(3)	Eu_1	2.999
		H(80C)_F(8)	Eu_2	2.678
		H(81)_F(30)	Eu_2	2.898
		H(82B)_F(32)	Eu_2	3.021
		H(82B)_F(33)	Eu_2	2.965
	CF_FC	F(32)_F(16)	In between Eu_1/ Eu_2	3.094
		F(15)_F(37)	In between Eu_1/ Eu_2	2.820
		F(19)_F(41)	In between Eu_1/ Eu_2	3.053
		F(38)_F(6)	In between Eu_1/ Eu_2	3.241
		F(7)_F(29)	In between Eu_1/ Eu_2	2.724
5-Eu^{iPr}*SSSSSSSS*	CH_O	H(5B)_O(1)	Eu_1	2.899
		H(70A)_O(15)	Eu_2	2.979
	CF_ *π*(*β*-diketonate)	F(12)_ *π*	Eu_2	2.989
	CF_ *π* (Pybox)	F(4)_ *π*(*Py*)	Eu_1	3.076
	CH_F	H(15B)_F(6)	Eu_1	2.618
		H(16)_F(27)	Eu_1	2.897
		H(17A)_F(23)	Eu_1	2.947
		H(17A)_F(25)	Eu_1	2.954
		H(80B)_F(29)	Eu_2	3.087
		H(82A)_F(8)	Eu_2	2.745
		H(82C)_F(14)	Eu_2	2.859
		H(81)_F(14)	Eu_2	2.632
		H(81)_F(12)	Eu_2	2.990
	CF_FC	F(16)_F(25)	In between Eu_1/ Eu_2	3.154
		F(36)_F(15)	In between Eu_1/ Eu_2	2.807
		F(40)_F(21)	In between Eu_1/ Eu_2	3.049
		F(8)_F(39)	In between Eu_1/ Eu_2	3.202
		F(28)_F(9)	In between Eu_1/ Eu_2	2.716

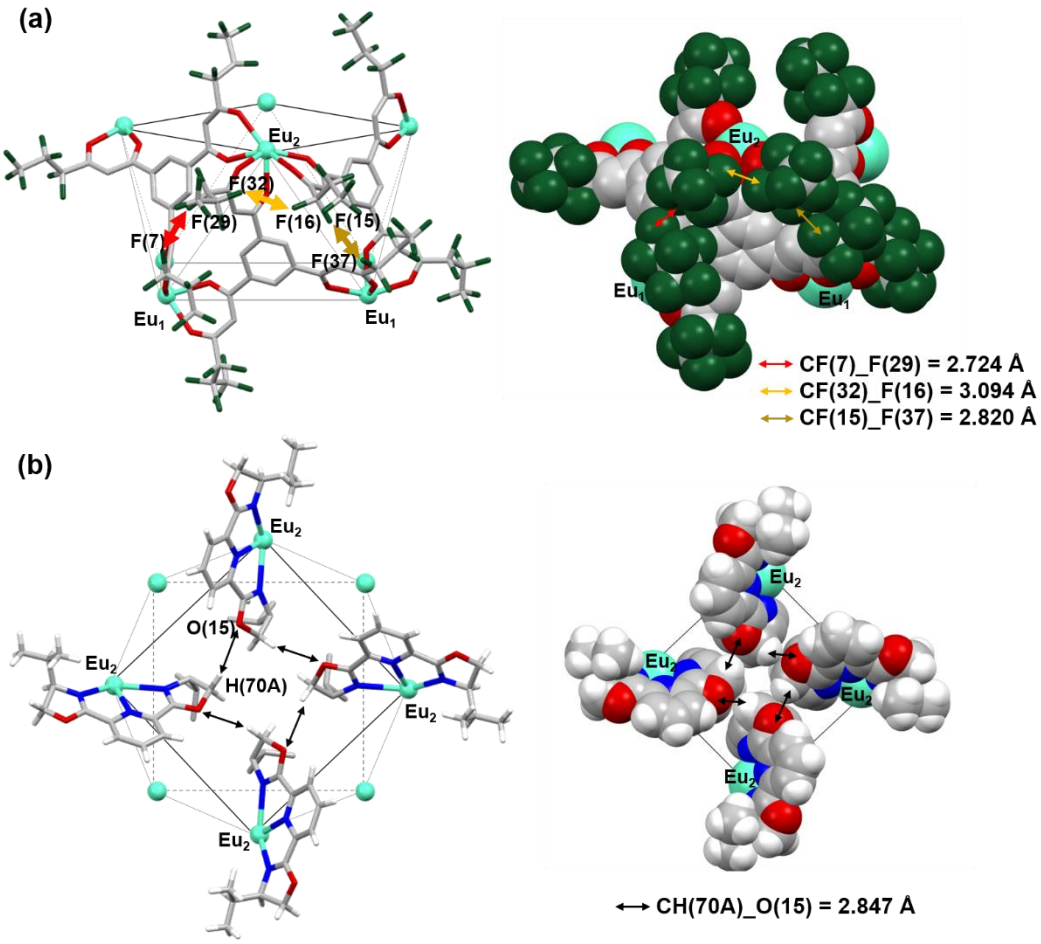

Figure A13. (a) CF_F interactions between THP ligands, and (b) CH_O interactions between ^{i}Pr-pybox ligands found in the crystal structure of **5-Eu^{iPr}*RRRRRRRR***.

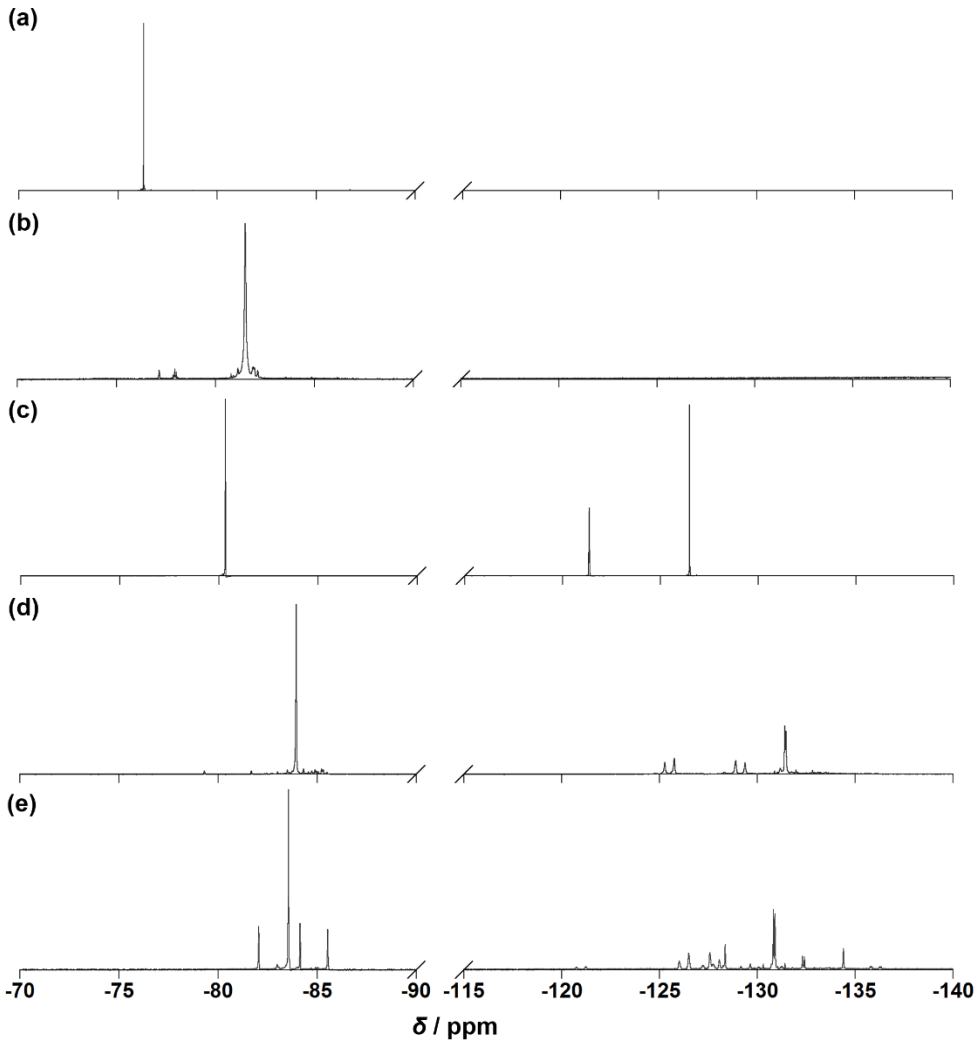

Figure A14. ^{19}F-NMR spectra of (a) H_3TTP ligand, (b) [Eu^{III}_4(TTP)$_4$] and (c) H_3THP ligand in chloroform-d. ^{19}F-NMR spectra of [Eu^{III}_4(THP)$_4$] in (a) methanol-d_4 and (e) acetone-d_6.

^{1}H NMR signal assignment of [(*R*)–Ph-Pybox]$_4$(Y^{III})$_4$(BTP)$_6$.

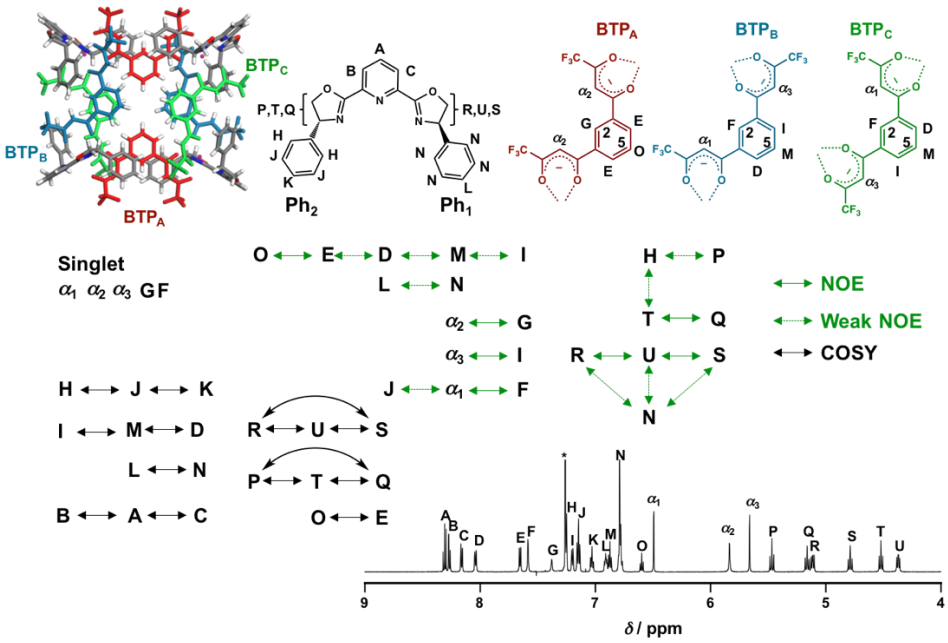

^{1}H NMR signal assignment of [(*R*)–Ph-Pybox]$_4$(Y^{III})$_4$(BTP)$_6$ was performed as follows. For the clarity of assignment, we initially classified the six BTP ligands of [(*R*)-Ph-Pybox]$_4$(Y^{III})$_4$(BTP)$_6$ into three groups, BTP$_A$, BTP$_B$, and BTP$_C$. On one hand BTP$_A$ preserves the ligand C_2-symmetry, on the other hand BTP$_B$ and BTP$_C$ (they are identical) loss of the C_2-symmetry in the self-assembly. The self-assembly [(*R*)-Ph-Pybox]$_4$(Y^{III})$_4$(BTP)$_6$ exhibits a total of 24 resonances at 4.0–8.5 ppm, wherein there are five singlet signals (α_{1-3}, F, and G). The singlet signals due to the aromatic CH proton at position 2 for the bis β-diketonate ligands (BTP) should be found in the aromatic region (> 7 ppm). The corresponding singlets can be found at 7.38 ppm (G) and 7.59 ppm (F) with an integration ratio of 1:2 (4H:8H). The six BTP ligands in [(*R*)-Ph-Pybox]$_4$(Y^{III})$_4$(BTP)$_6$ should be differentiated into two sets of differentiated coordination modes, the BTP$_A$ singly bridges the two metal ions, conversely BTP$_B$ and BTP$_C$ (they are identical) bridge together to the two Y^{III} ions (see the structure). Thus, the singlet peaks at 7.38 ppm (G) can be assigned to the aromatic CH proton at position 2 for BTP$_A$ and 7.59 ppm (F) is assignable to that for BTP$_B$ and BTP$_C$. In the same manner, two triplet signals are found at 6.60 ppm (O) and 6.87 ppm (M) with an integration ratio of 1:2 (4H:8H), corresponding to the aromatic CH proton at position 5 for BTP$_A$ and the other identical BTP ligands (BTP$_B$ and BTP$_C$). Those aromatic protons of BTP show upfield shift (typically "O") due to the shielding effects in the self-assembly. Based on the analysis of the ^{1}H,^{1}H COSY correlations (Figure S4), we assigned the aromatic CH proton at 4, 5 positions for BTP$_A$ (E) as well as for BTP$_B$ and BTP$_C$ (I and D). In the region for the α-proton (5-7 ppm), three singlets are found with an integration ratio of 1:1:1 (α_{1-3}). There are NOE cross peaks between G and α_2, between F and α_1, as well as between I and α_3 (Figure S5). Thus, α_2 corresponds to the α-proton of BTP$_A$ with C_2 symmetry, and the other two singlets (α_1 and α_3) are assignable to

the α-protons of BTP_B and BTP_C without C_2-symmetry. Furthermore, a weak NOE signal was observed between α_1 and J (7.15 ppm), which could be identified between the α-protons of $BTP_{B/C}$ and the side arm of (*R*)-Ph-Pybox (Ph_2). The aromatic protons due to the side arm of (*R*)-Ph-Pybox (Ph_2) were identified based on the analysis of the $^1H,^1H$ COSY correlations (H, J, and K). The aromatic proton due to Ph_2 (H) has NOE-cross peaks with three multiplet signals (P, T, and Q) in the aliphatic region for (*R*)-Ph-Pybox (4–5.6 ppm). The chiral ligand [(*R*)-Ph-Pybox] loses the original ligand C_2-symmetry in the self-assembly because of the differentiation in its side arms (Ph_1 and Ph_2) in terms of the ligand-to-ligand interactions (see the text). The other three multiplet signals (R, U, and S) in the aliphatic region show NOE-cross signals with the aromatic protons (N at 6.79 ppm) due to the side arm of (*R*)-Ph-Pybox (Ph_1). The other aromatic protons (Ph_1 and the central pyridine unit) were successfully determined on the basis of the $^1H,^1H$ COSY analysis (A, B, C, and L). 2D-DOSY NMR spectra are given in Figure S14 for the reference.

^{1}H NMR signal assignment of [(*R*)–Ph-Pybox]$_4$(Eu^{III})$_4$(BTP)$_6$.

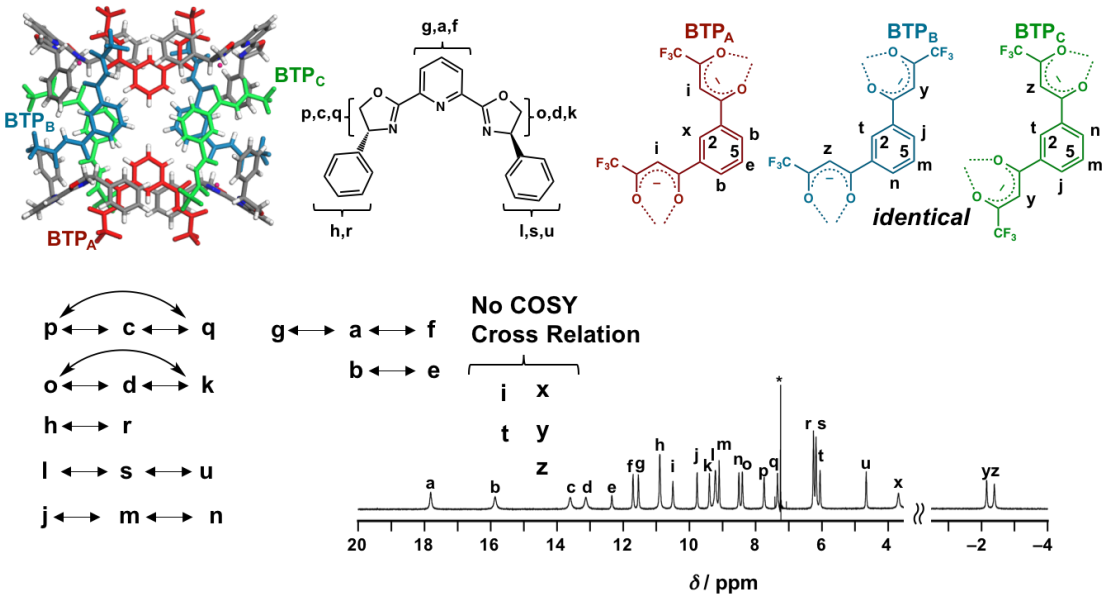

^{1}H NMR signal assignment of the paramagnetic complex [(*R*)-Ph-Pybox]$_4$(Eu^{III})$_4$(BTP)$_6$ was performed in comparison with the NMR signals of [(*R*)-Ph-Pybox]$_4$(Y^{III})$_4$(BTP)$_6$. ^{1}H NMR spectrum (600 MHz, CD_3Cl) of the [(*R*)-Ph-Pybox]$_4$(Eu^{III})$_4$(BTP)$_6$ assembly shows a total of 24 resonances spread over wide chemical shift range (–3–18 ppm) according to the paramagnetic properties of lanthanide(III), in which there is some analogy with the NMR signal pattern of diamagnetic [(*R*)-Ph-Pybox]$_4$(Y^{III})$_4$(BTP)$_6$. As in the case of [(*R*)-Ph-Pybox]$_4$(Y^{III})$_4$(BTP)$_6$, [(*R*)-Ph-Pybox]$_4$(Eu^{III})$_4$(BTP)$_6$ shows total five broad signals (i t, x, y, and z) that have no $^1H,^1H$ COSY correlation (Figure S6). These signals should be assignable to the α-protons and the aromatic CH proton at position 2 for BTP (vide supra). The integrated intensity of signal “x” is half of that of the other signals. Thus, the signal “x” is assignable to

the 7 aromatic CH proton at position 2 for BTP_A. The other four signals (i t, y, and z) correspond to the α-protons and the aromatic CH proton at position 2 for BTP_B and BTP_C (those are identical). In the same manner, a weak integrated signal “e” was assigned as the aromatic CH proton at position 5 for BTP_A, and signal “b” as its vicinal protons (positions 4 and 1) on the basis of the $^1H,^1H$ COSY analysis (Figure S6). The aliphatic protons of (*R*)-Ph-Pybox (p, c, q, o, d, and k) and the central pyridine unit (g, a, f) can be assigned by the $^1H,^1H$ COSY cross-coupling patterns. The aromatic protons due to the side arms of (*R*)-Ph-Pybox were assigned judging from their integrated intensity and the $^1H,^1H$ COSY cross relation (h, r, and l, s, u).

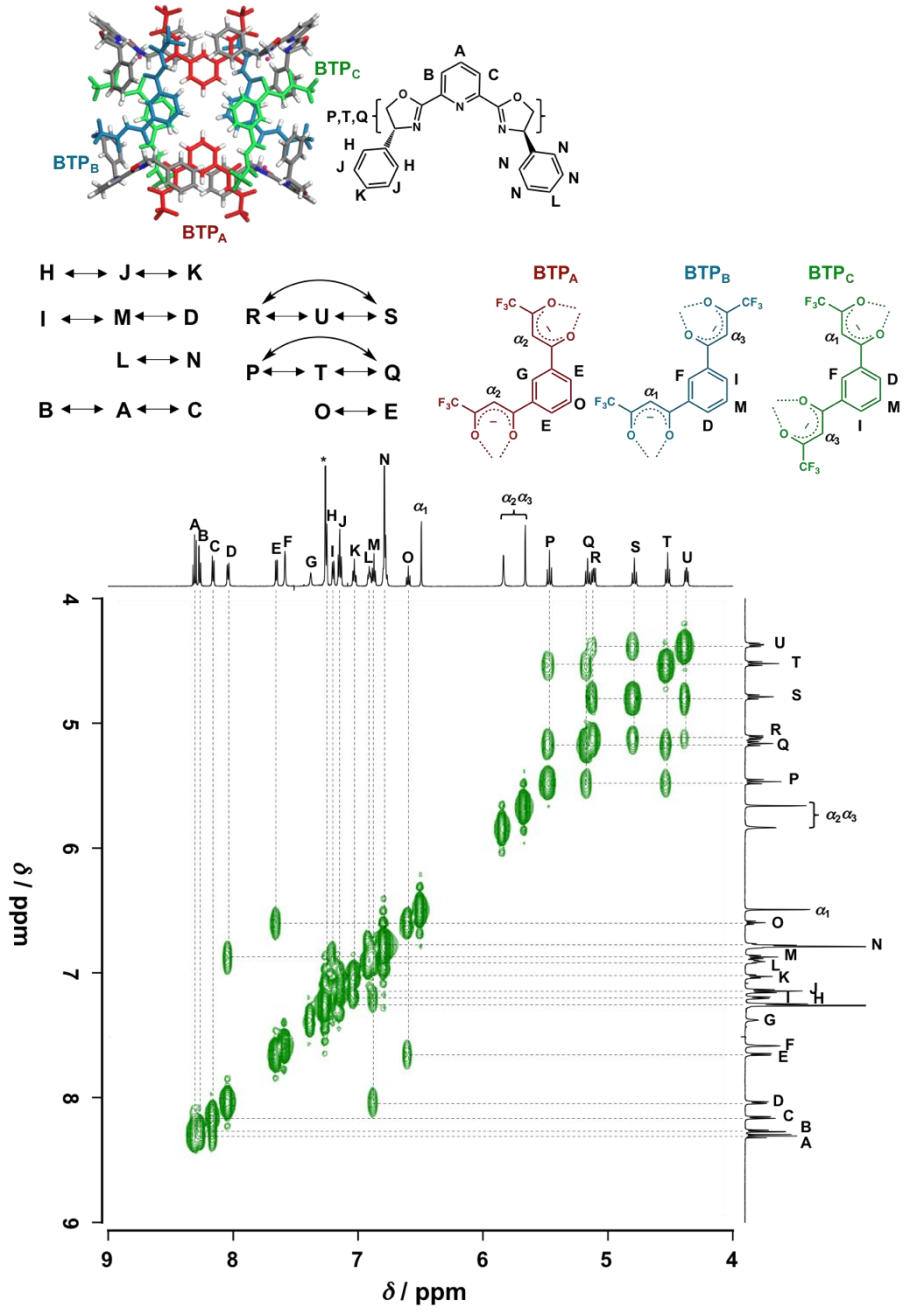

Figure A15. $^1H,^1H$ COSY NMR (600 MHz) spectrum of **1-Y^{Ph}*RRRR*** in chloroform-d at 298 K.

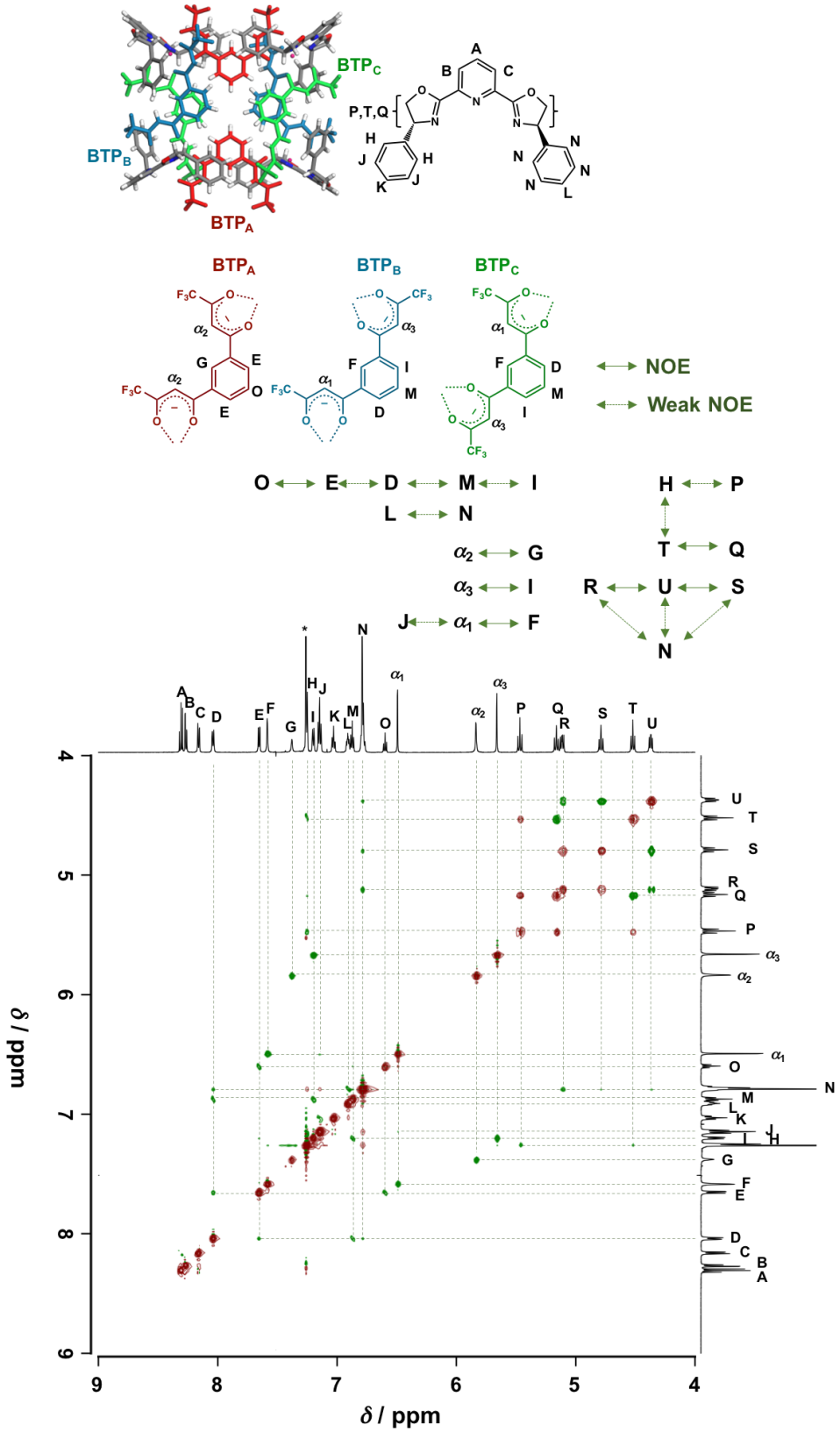

Figure A16. 2D-ROESY NMR (600 MHz) spectrum of **1-Y^{Ph}*RRRR*** in chloroform-d at 298 K.

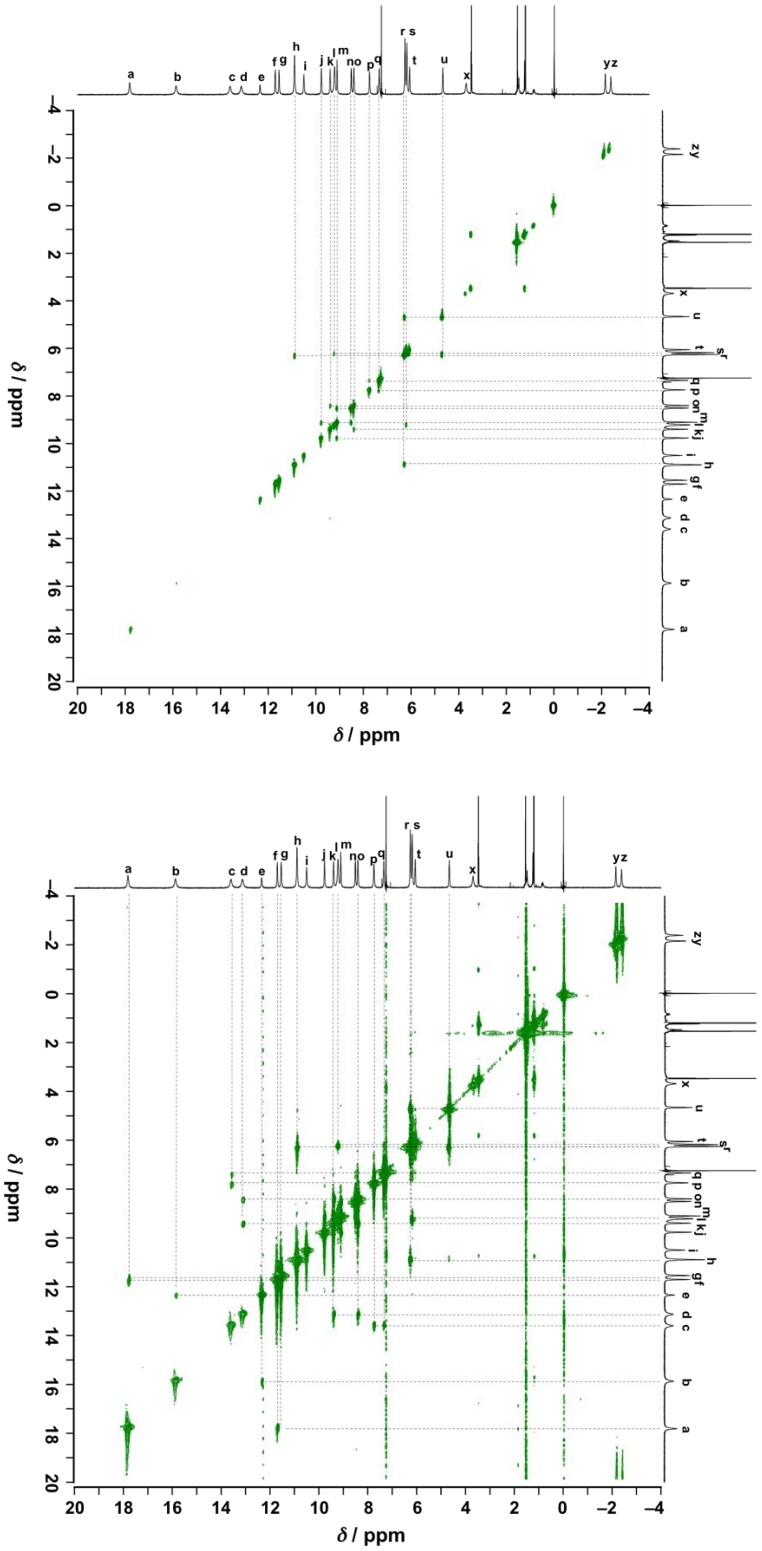

Figure A17. ^{1}H,^{1}H cosy NMR (600 MHz) of **1-Eu^{Ph}*RRRR*** in chloroform-d at 298 K with higher (top) and lower (bottom) threshold level.

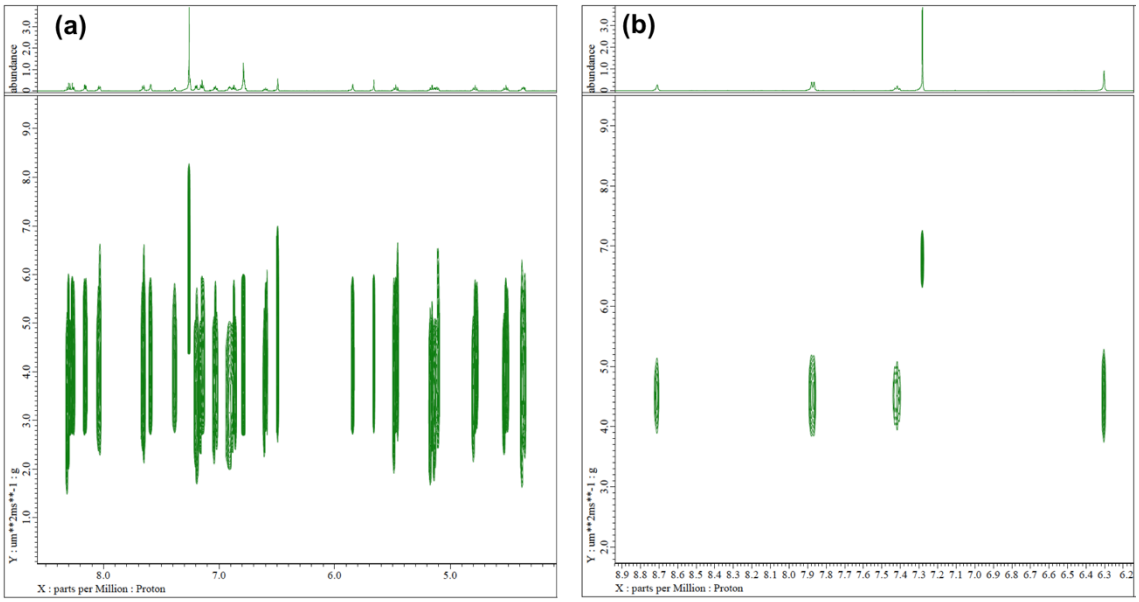

Figure A18. 2D-DOSY NMR spectra of (a) **1-Y^{Ph}*RRRR*** and (b) [(Y^{III})$_2$(BTP)$_3$] in chloroform-d at 298 K.

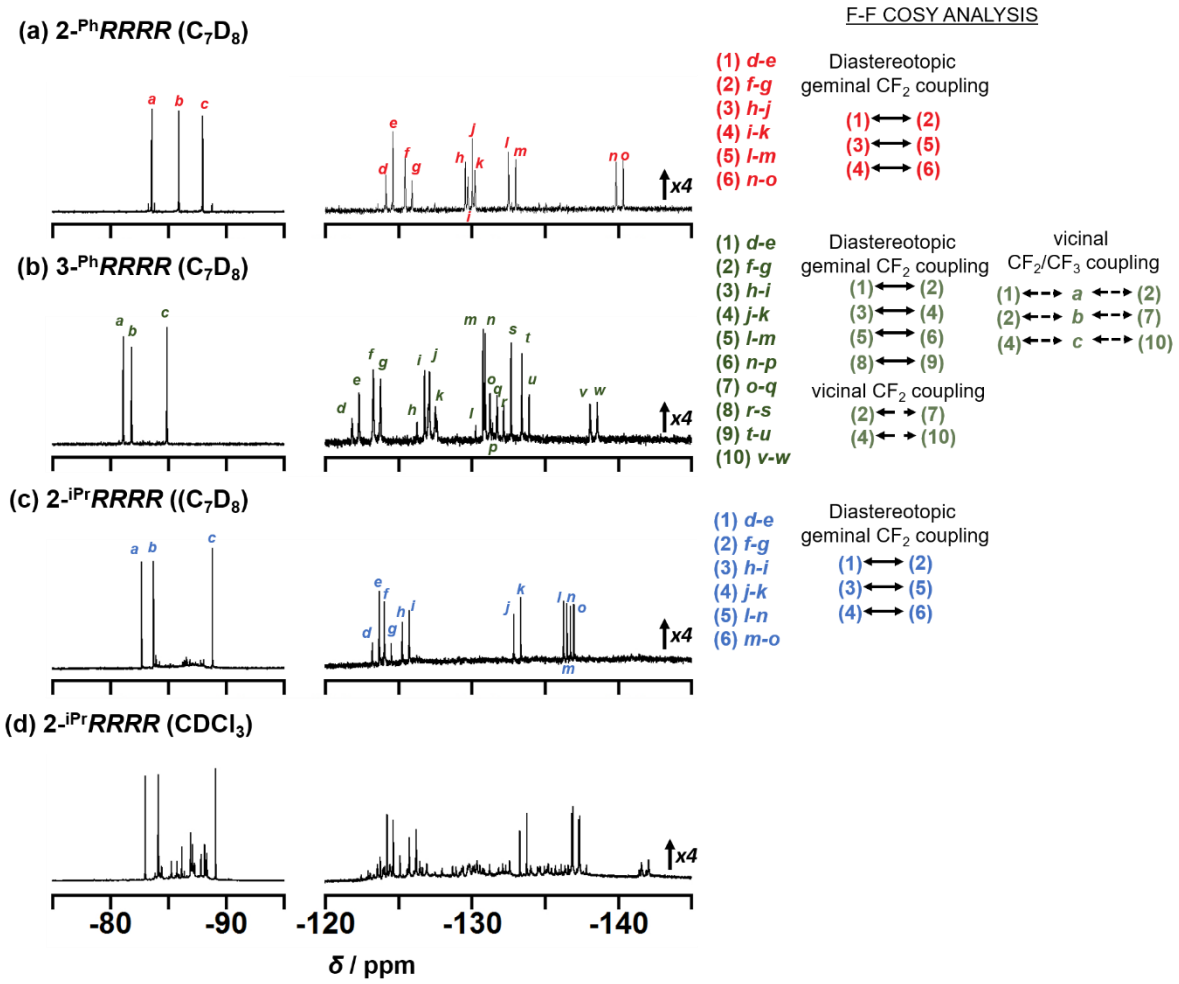

Figure A19. ^{19}F-NMR spectrum (600MHz) of (a) **2-^{Ph}*RRRR***, (b) **3-^{Ph}*RRRR*** (c) **2-^{iPr}*RRRR*** in toluene-d_8 at 298 K. (d) ^{19}F-NMR spectrum (600MHz) of **2-^{iPr}*RRRR*** in *d*-chloroform at 298 K. Intensity of -120ppm to -145ppm region was scaled down for clarity.

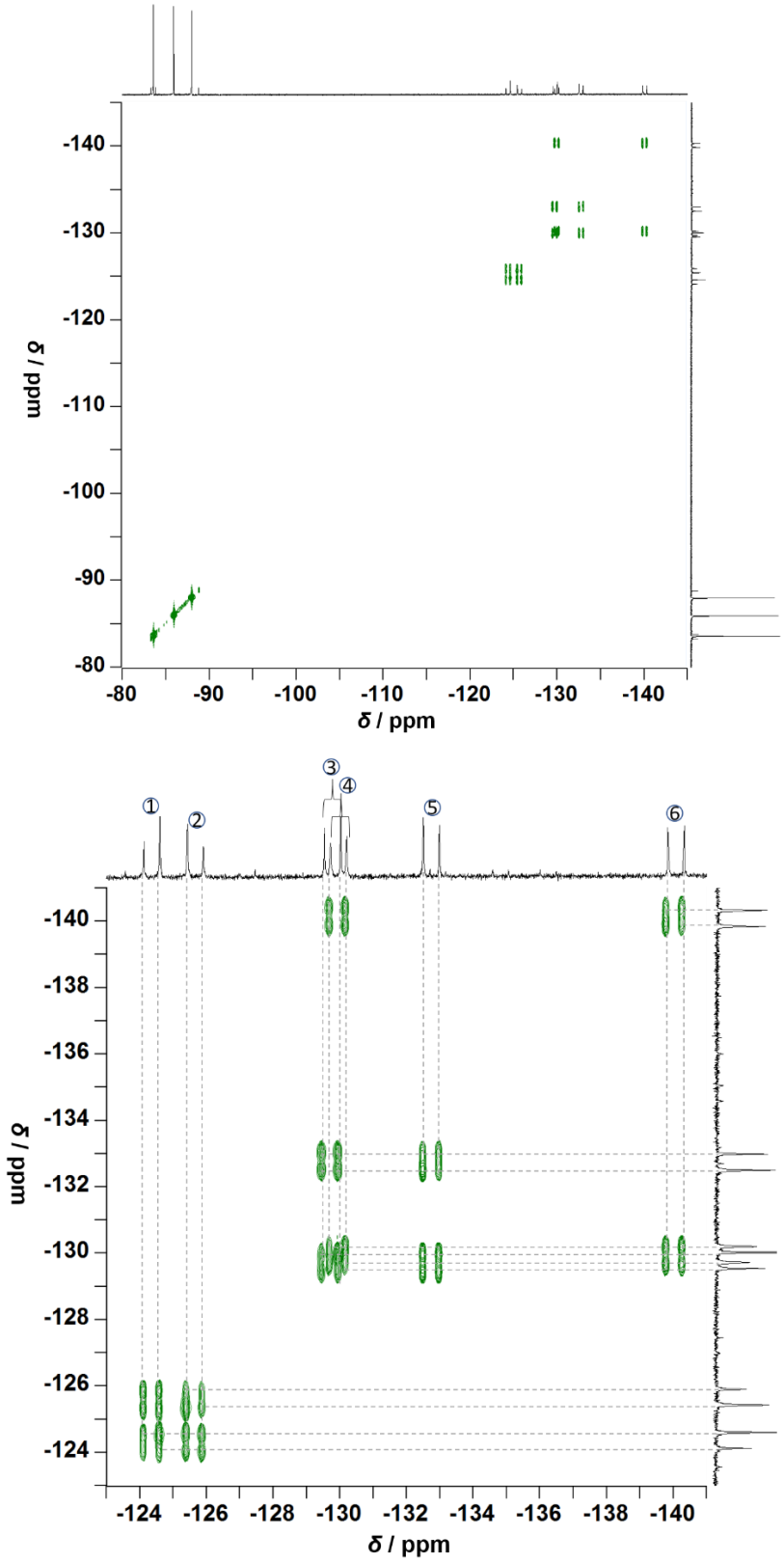

Figure A20. (Top) Full spectrum and (bottom) -123ppm to -141 ppm region of $^{19}F,^{19}F$ COSY NMR (600 MHz) of **2-^{Ph}*RRRR*** in toluene-d_8 at 298 K.

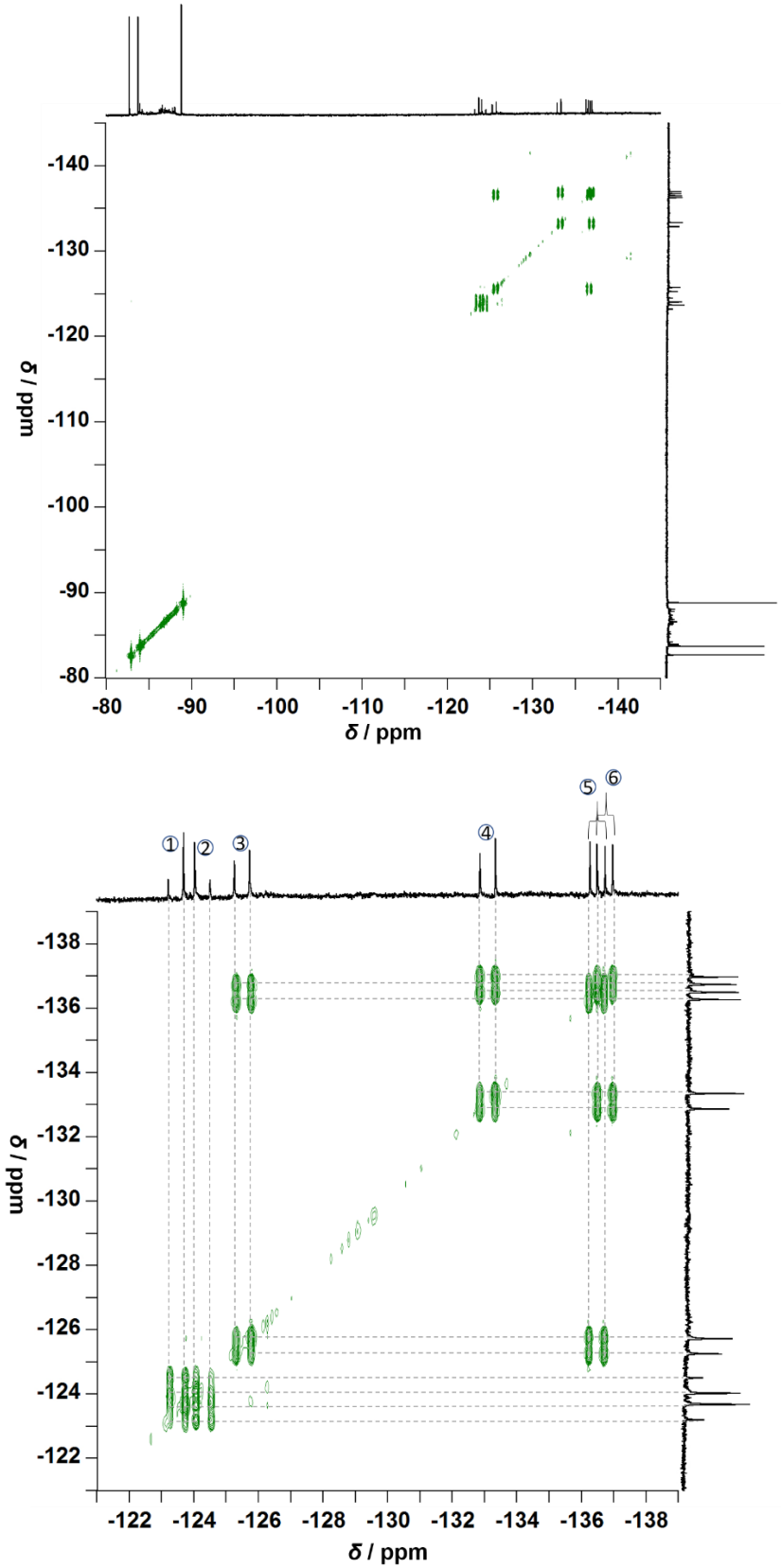

Figure A21. (Top) Full spectrum and (bottom) -123ppm to -141 ppm region of $^{19}F,^{19}F$ COSY NMR (600 MHz) of **2-^{iPr}*RRRR*** in toluene-d_8 at 298 K.

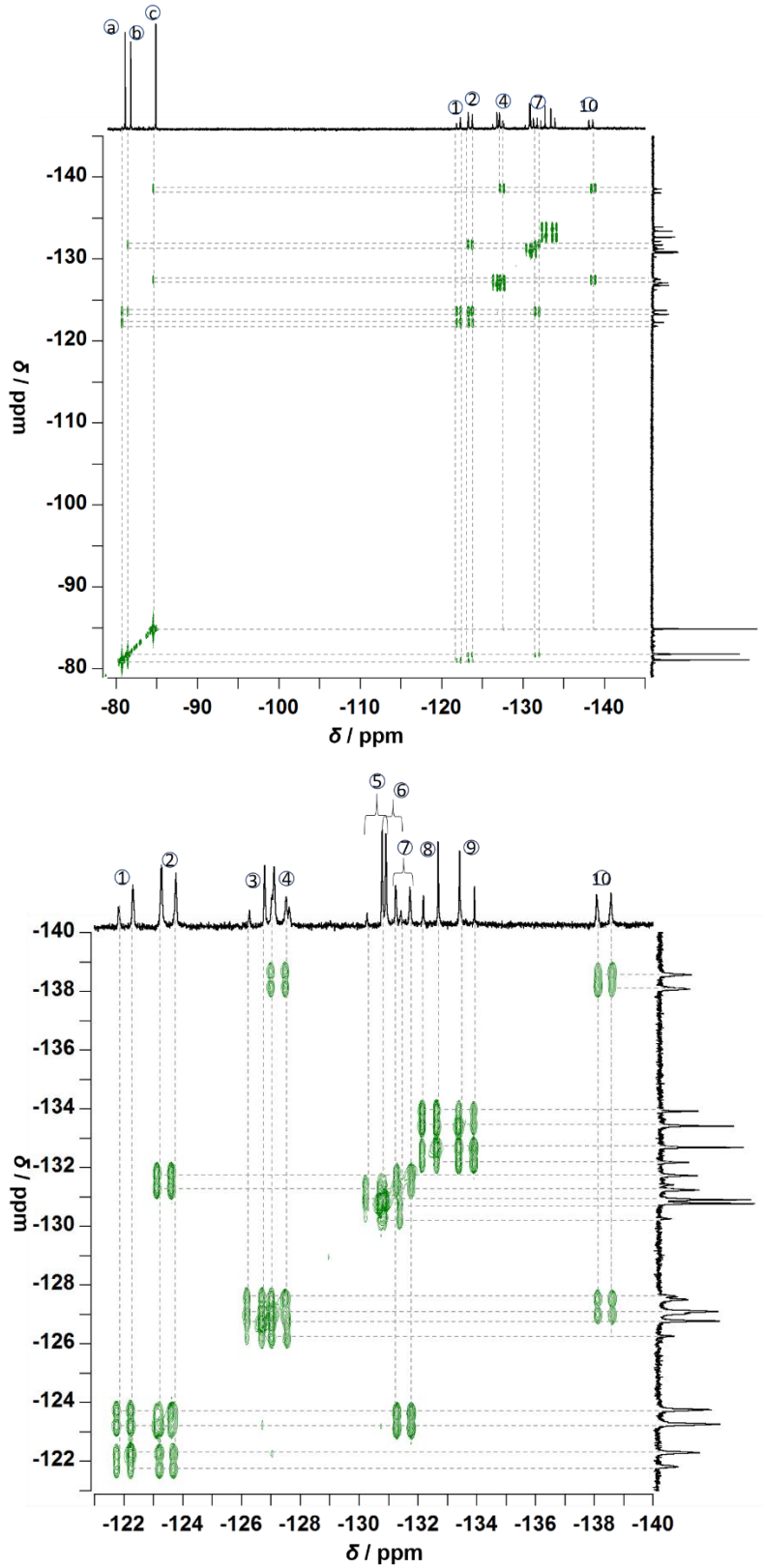

Figure A22. (Top) Full spectrum and (bottom) -123ppm to -141 ppm region of $^{19}F,^{19}F$ COSY NMR (600 MHz) of **2-^{Ph}*RRRR*** in toluene-d_8 at 298 K.

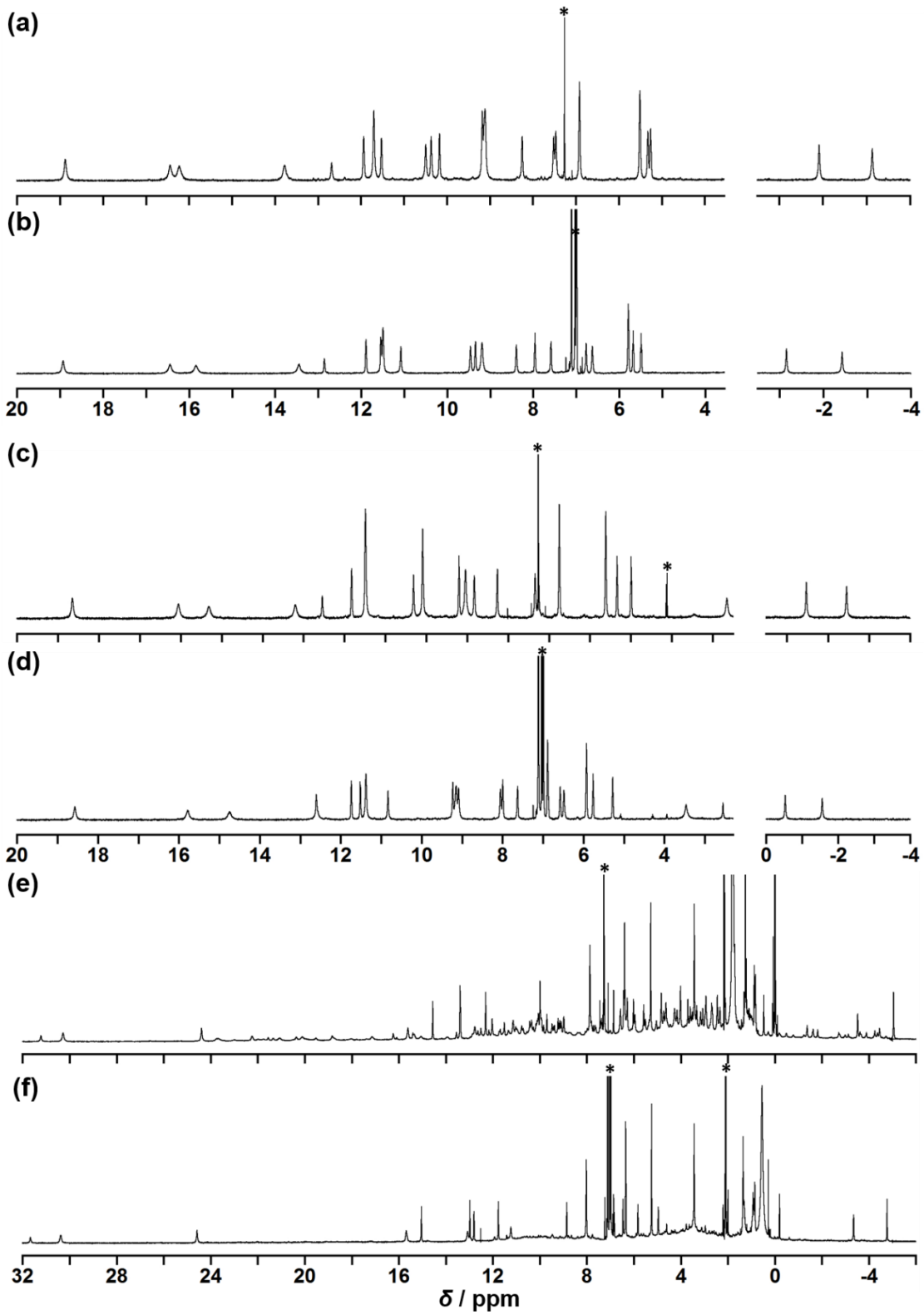

Figure A23. ^{1}H-NMR (600MHz) spectra of **2-Eu^{Ph}*RRRR*** in (a) chloroform-d, and (b) toluene-d_8 at 298K. ^{1}H-NMR (600MHz) spectra of **3-Eu^{Ph}*RRRR*** in (c) chloroform-d, and (d) toluene-d_8 at 298K. ^{1}H-NMR (600MHz) spectra of **2-Eu^{iPr}*RRRR*** in (a) chloroform-d, and (b) toluene-d_8 at 298K.

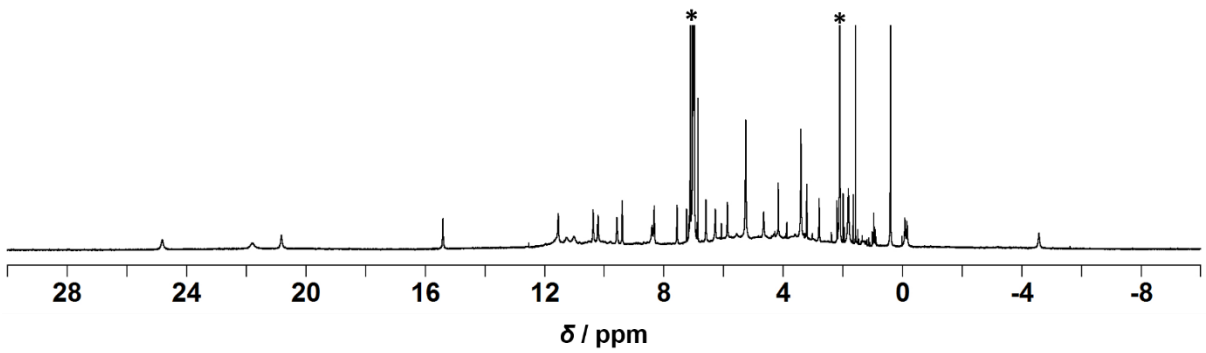

Figure A24. ^{1}H-NMR (600MHz) spectra of **4-Eu^{iPr}*RRRR*** in toluene-d_8 at 298K.

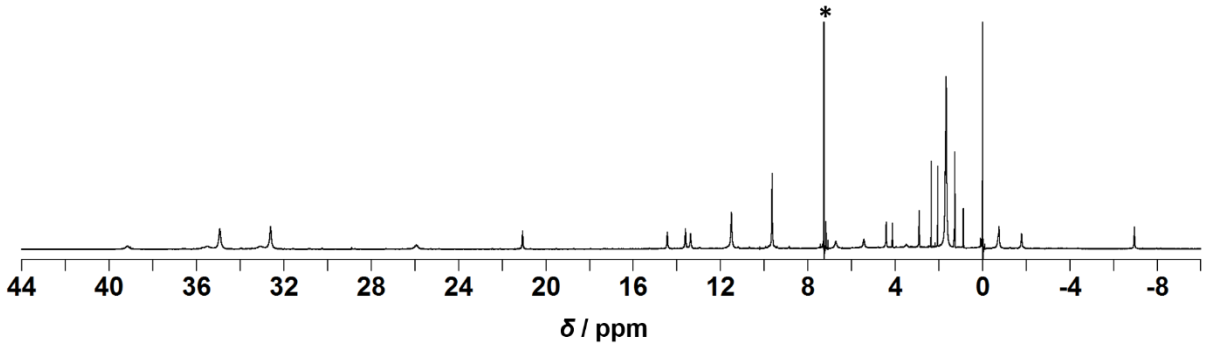

Figure A25. ^{1}H-NMR (600MHz) spectra of **5-Eu^{iPr}*RRRRRRRR*** in chloroform-*d* at 298K.

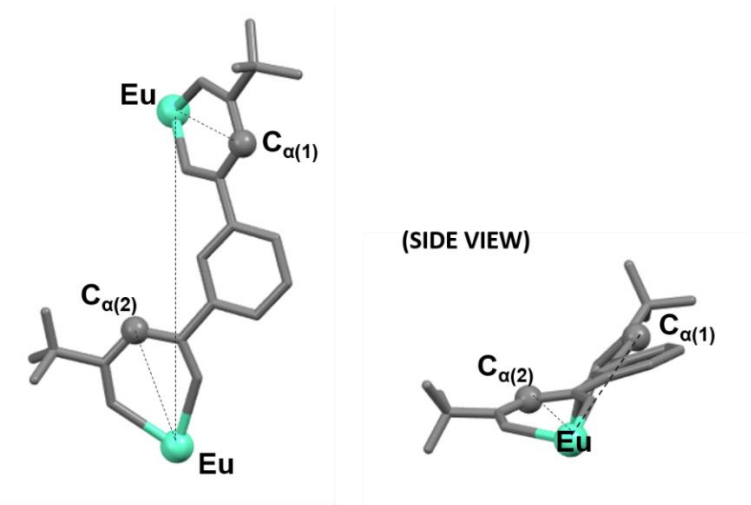

Figure A26. Dihedral angle of anionic L ligand, determined from the angle between the plane bisecting Eu- $C_{\alpha(1)}$ and that bisecting Eu-$C_{\alpha(2)}$.

APPENDIX- UV-VIS ABSORPTION AND CIRCULAR DICHROISM (CD) PROFILE

All the tetranuclear $(Pybox)_4Ln^{III}_4L_6$ and octanuclear $[^{i}Pr\text{-}Pybox]_8Ln^{III}_8L_8$ self-assemblies exhibit similar absorption and CD profiles (Figure 4.4, and 4.5). The assemblies show CD bands in the spectral range of the π-π^* transition of the □-diketonate moieties at around □ = 300–370 nm, suggesting that homochiral assembly formation induces Cotton effects in the absorption band of the β-diketonate ligands. The induced CD spectra show splitting Cotton effects due to excitonic coupling between the BTP ligands,[58–60] suggesting the induced chiral configuration of the bis- or tris-β-diketonate ligands around the Ln^{III} metal center, as revealed in the X-ray crystal structures. The sign of bipolar bis-β-diketonate CD signal of tetranuclear $[(R)\text{-}Pybox]_4Ln^{III}_4L_6$ follows the sequence of (+) and (–) whereas octanuclear $[(R)\text{-}^{i}Pr\text{-}Pybox]_4Ln^{III}_4L_6$ follows the sequence of (-) and (+).

The circular helicates of **1-Eu^{Ph}*RRRR*** and **1-Eu^{Ph}*SSSS*** are sufficiently rigid for the investigation of heterochiral interactions between them, where **1-Eu^{Ph}*RRRR*** and **1-Eu^{Ph}*SSSS*** show no appreciable ligand exchange in racemic condition. Upon spontaneous mixing of **1-Eu^{Ph}*RRRR*** and **1-Eu^{Ph}*SSSS*** in chloroform, a suspension was formed. Figure A23 presents the photographs of the circular Eu^{III} helicates with different ratios between the of **1-Eu^{Ph}*RRRR*** and **1-Eu^{Ph}*SSSS*** in chloroform solutions. Although pure **1-Eu^{Ph}*RRRR*** and **1-Eu^{Ph}*SSSS*** samples are transparent, each racemic mixture forms a suspension. The resulting suspension was diluted (150-fold) to obtain a clear solution for CD spectral measurements of the racemic samples, with no appreciable suspension in the resulting dilute solutions. The CD profile is identical in each case (Figure A23a), but the amplitude (θ) increases almost proportionally with an increase in the initial enantiomeric excess (*ee*) of the circular Eu^{III} helicates (Figure A24b). The linear relationship suggests that each racemic sample contains mostly the homochiral diastereomers (**1-Eu^{Ph}*RRRR*** and **1-Eu^{Ph}*SSSS***), where heterochiral diastereomers (e.g., **1-Eu-^{Ph}*RRSS***, **1-Eu-^{Ph}*RSSS***, **1-Eu-^{Ph}*RRRS***) formed by ligand exchange apparently do not extensively coexist. Such ill-defined structures should possess different CD profiles with smaller amplitude than that of the homochiral diastereomers, which should result in a threshold-type non-linear relationship between the CD intensity and the initial enantiomeric excess. The observed linear relationship indicates the resulting precipitate as an insoluble heterochiral aggregate between the **1-Eu^{Ph}*RRRR*** and **1-Eu^{Ph}*SSSS*** isomers. This observation is in coincidence with the homochiral racemic crystals of **1-Eu^{Ph}*RRRR*** and **1-Eu^{Ph}*SSSS*** obtained from reaction of racemic Ph-pybox with $[Eu^{III}_2(BTB)_3]$ in the synthesis of circular Eu^{III} helicates.

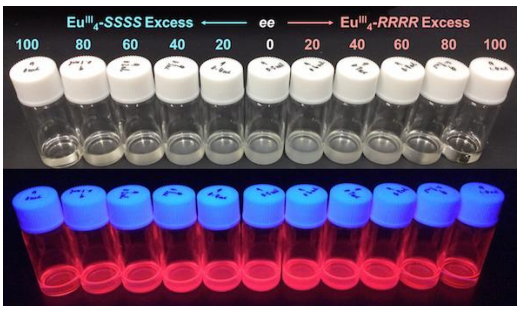

Figure A27. Photographs of the circular Eu^{III} helicates (initial total concentration: 4.7×10^{-4} M) with different *ee* in chloroform under bright conditions (top) and UV/light irradiation (bottom).

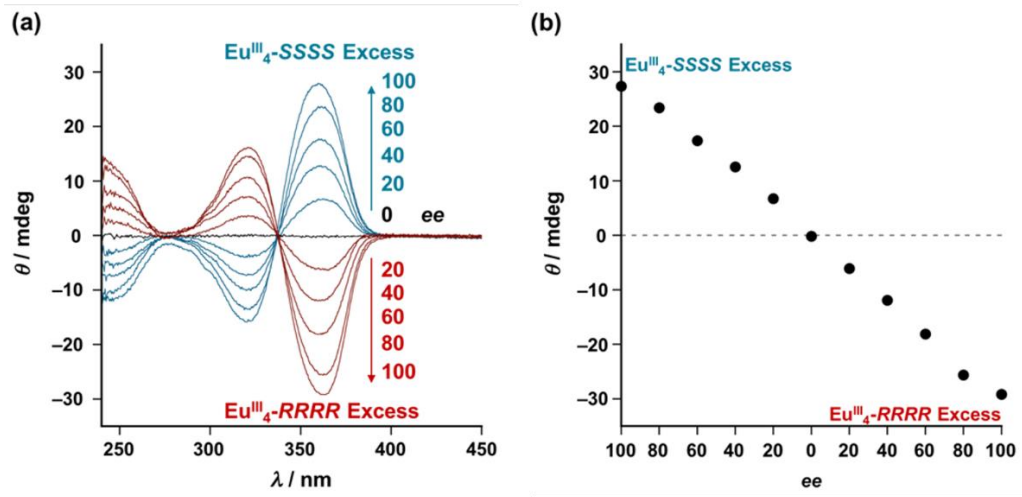

Figure A28. (a) CD spectra of the resulting dilute solutions of **1-Eu^{Ph}*RRRR*** and **1-Eu^{Ph}*SSSS*** mixture with different ratio in chloroform. (b) Plot of θ at λ = 363 nm vs the initial *ee* of the circular Eu^{III} helicate.

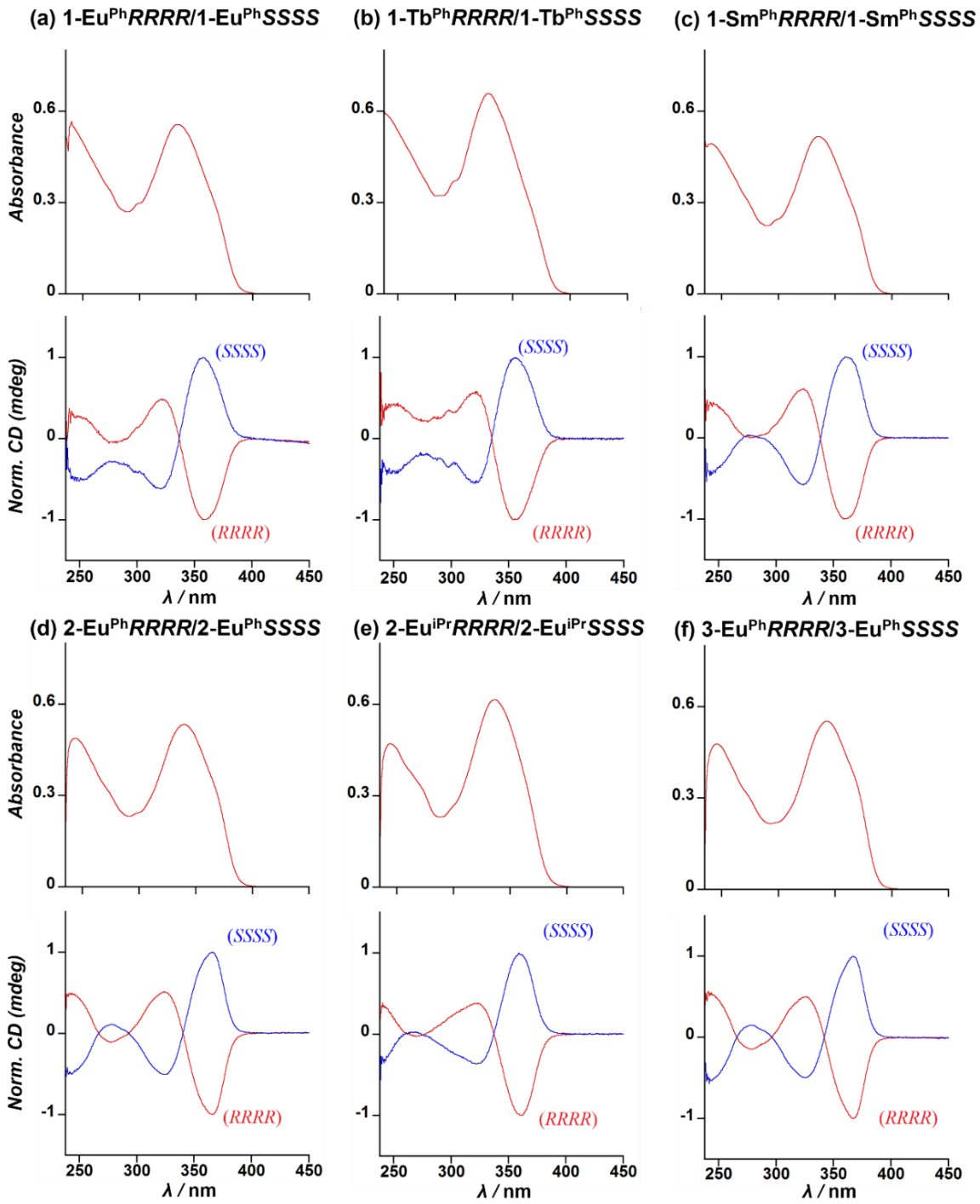

Figure A29. UV spectra (top) of (a) **1-Eu^{Ph}*RRRR***, (b) **1-Tb^{Ph}*RRRR***, (c) **1-Sm^{Ph}*RRRR***, (d) **2-Eu^{Ph}*RRRR***, (e) **2-Eu^{iPr}*RRRR***, and (f) **3-Eu^{Ph}*RRRR*** in chloroform at 298K (conc. = 3.4 × 10^{-6} M). Normalized CD spectra of (a) **1-Eu^{Ph}*RRRR*/1-Eu^{Ph}*SSSS***, (b) **1-Tb^{Ph}*RRRR*/1-Tb^{Ph}*SSSS***, (c) **1-Sm^{Ph}*RRRR*/1-Sm^{Ph}*SSSS***, (d) **2-Eu^{Ph}*RRRR*/2-Eu^{Ph}*SSSS***, (e) **2-Eu^{iPr}*RRRR*/2-Eu^{iPr}*SSSS***, and (f) **3-Eu^{Ph}*RRRR*/3-Eu^{Ph}*SSSS*** in chloroform at 298K (conc. = 3.4 × 10^{-6} M). [Red and blue solid line for the (*R*)- and (*S*)- enantiomers, respectively.]

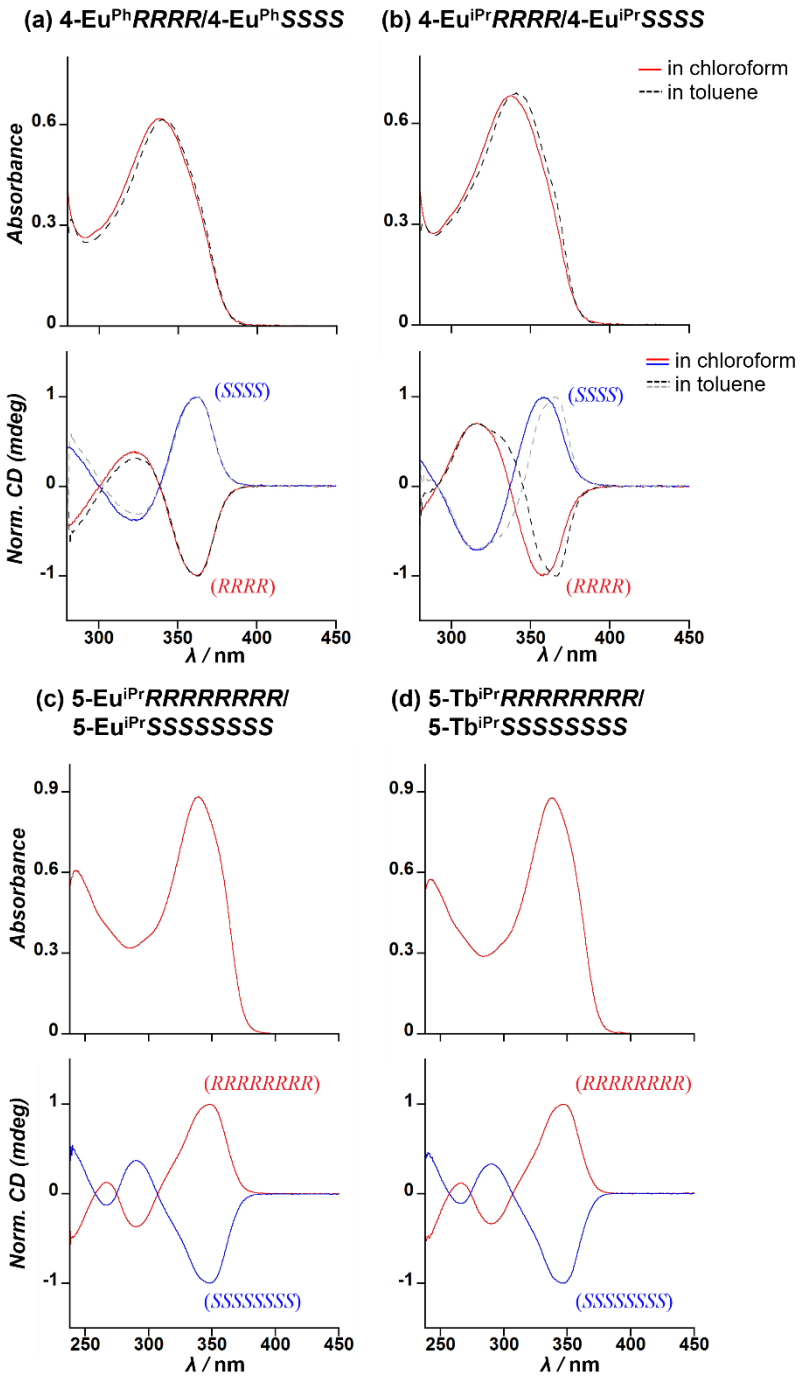

Figure A30. UV spectra (top) of (a) **4-Eu^{Ph}*RRRR***, and (b) **4-Eu^{iPr}*RRRR*** in chloroform and toluene at 298K (conc. = 3.4 × 10^{-6} M). Normalized CD spectra of (a) **4-Eu^{Ph}*RRRR*/4-Eu^{Ph}*SSSS***, and (b) **4-Eu^{iPr}*RRRR*/4-Eu^{iPr}*SSSS*** in chloroform and toluene at 298K (conc. = 3.4 × 10^{-6} M). [Red and blue solid line for the (*R*)- and (*S*)- enantiomers in chloroform, respectively; black and grey dashed line for the (*R*)- and (*S*)- enantiomers in toluene]. UV spectra (top) of (c) **5-Eu^{iPr}*RRRRRRRR***, and (b) **5-Tb^{iPr}*RRRRRRRR*** in chloroform at 298K (conc. = 2.6 × 10^{-5} M). Normalized CD spectra of (a) **5-Eu^{iPr}*RRRRRRRR*/5-Eu^{iPr}*SSSSSSSS***, and (d) **5-Tb^{iPr}*RRRRRRRR*/5-Tb^{iPr}*SSSSSSSS*** in chloroform at 298K (conc. = 2.6 × 10^{-5} M). [Red and blue solid line for the (*R*)- and (*S*)- enantiomers in chloroform, respectively]

APPENDIX-EMISSION DECAY PROFILE

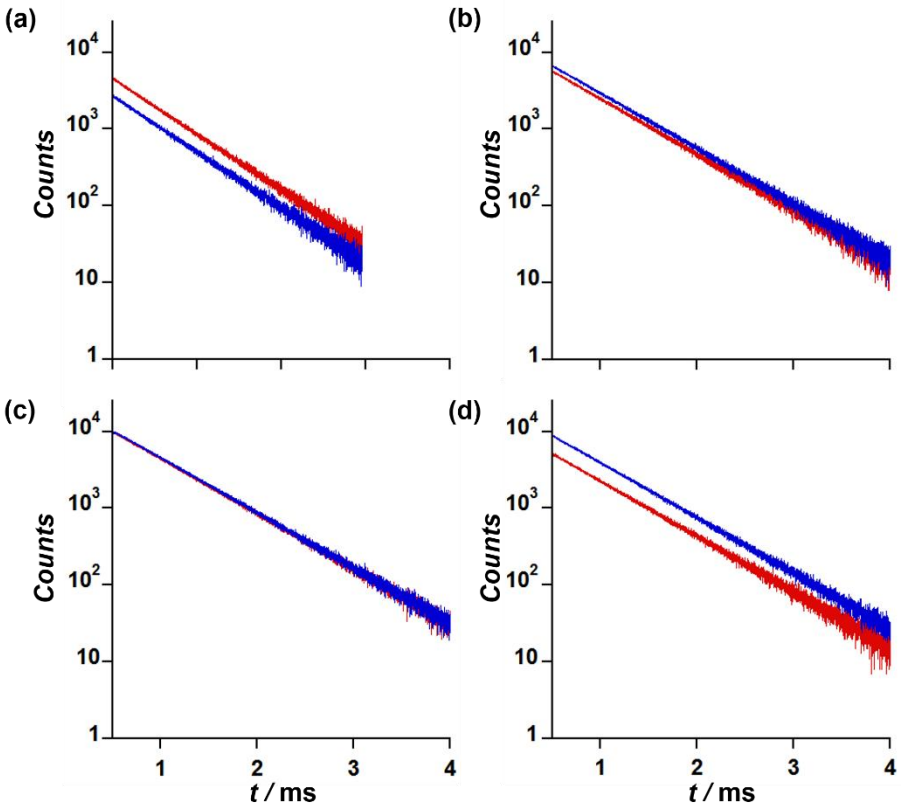

Figure A31. Emission decay profile of (a) **1-Eu^{Ph}*RRRR*/1-Eu^{Ph}*SSSS***, (b)**2-Eu^{Ph}*RRRR*/2-Eu^{Ph}*SSSS***, (c) **2-Eu^{iPr}*RRRR*/2-Eu^{iPr}*SSSS***, and (d) **3-Eu^{Ph}*RRRR*/3-Eu^{Ph}*SSSS*** at λ = 618 nm in chloroform at 298K (conc. = 3.4 × 10^{-6} M). [Red and blue solid line = *R* and *S* isomers respectively].

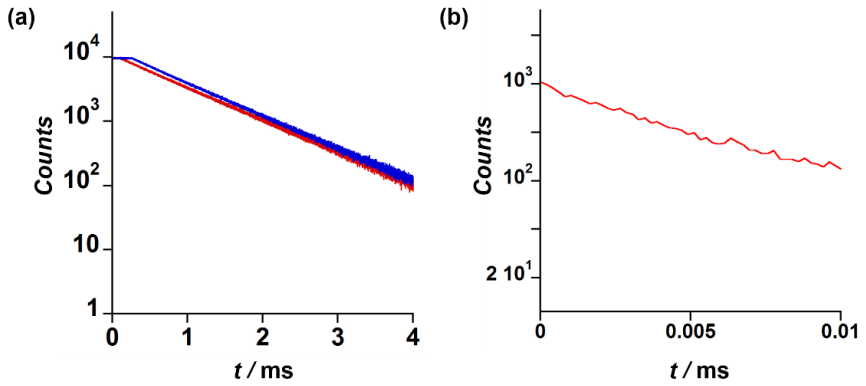

Figure A32. Emission decay profile of (a) **5-Eu^{iPr}*RRRRRRRR*/5-Eu^{iPr}*SSSSSSS*** at λ = 614 nm in chloroform (conc.= 2.6 × 10^{-5} M). (b) **5-Tb^{iPr}*RRRRRRRR*** at λ = 545 nm in chloroform (conc. = 2.6 × 10^{-5} M). [Red and blue solid line = *R* and *S* isomers respectively].

ACHIEVEMENTS

1. Tan, Y. B.; Kawai, T.; Yuasa, J. Ligand-to-Ligand Interactions That Direct Formation of D_2-Symmetrical Alternating Circular Helicates. *J. Am. Chem. Soc.*, **2018**, *140*, 10, 3683-3689.
2. Tan, Y. B.; Yamada, M.; Katao, S.; Nishikawa, Y.; Asanoma, F.; Yuasa, J.; Kawai, T. Self-assembled Tetranuclear Eu^{III} Complexes with D_2- and C_{2h}-Symmetrical Square Scaffold. *Inorg. Chem.*, **2020**, *59*, 17, 12867-12875.